

**Experimental and numerical research on a novel hysteretic  
dissipative and easily repairable device for composite  
steel-concrete frame structures**

**Diogo Jorge Santos Cabrita**

Dissertation for the degree of Master of Science in

**Civil Engineering**

Supervisors:

Prof. Luís Manuel Calado de Oliveira Martins

Prof. Jorge Miguel Silveira Filipe Mascarenhas Proença

**Jury**

Chairperson: Prof. António Manuel Figueiredo Pinto da Costa

Supervisor: Prof. Luís Manuel Calado de Oliveira Martins

Member of the Committee: Prof. Alper Kanyilmaz

**December 2020**



## Declaração

Declaro que o presente documento é um trabalho original da minha autoria e que cumpre todos os requisitos do Código de Conduta e Boas Práticas da Universidade de Lisboa.



## **Acknowledgments**

I would like to show my gratitude to Professor Luís Calado and Professor Jorge Miguel Proença for their guidance, availability and exemplary attention and support, in a stress-free and committed way.

Also, I want to express my thankfulness for being invited to be part of the DISSIPABLE project (RFCS 2017 Project No 800699) and for the grant that supported this work.

A special word of appreciation to Professor Luís Calado and Professor Alper Kanyilmaz for the opportunity given to participate in the international meetings of the DISSIPABLE project. This was definitely a unique experience to expand my academic knowledge and gain a broader view on the scientific research world.

Thank you to my fellow colleague Sérgio Nascimento for providing me with all the research material on the topic and for his valuable support.

Thank you to Tiago Farinha for the discussions shared under this research.

Thank you to the laboratory technicians Fernando Alves and Jorge Pontes for their prompt availability and all the great work they have done in the experimental setup process.

To my parents, Ana and Jorge, thank you for giving me the chance to achieve this goal and to my, recently doctorate, sister, Inês, for being a true inspiration of success in all terms.

Last but not least, I want to dedicate this work to all my friends that make the best of me thrive. I sincerely could not have done it without you.



## Abstract

In the structural design research and professional activities, there is an increasing requirement of safety and structure resilience when it comes to seismic events. Taking the experience collected in previous researches, a novel dissipative and repairable bracing device connection was developed. The device is applied in composite steel-concrete frame structures and comprises a transversal steel pin that dissipates energy through yielding.

In order to access the local performance of the device, experimental and numerical studies on eight different configurations are investigated. The study encompasses two pin geometries, chamfered or circular with different weld configurations and an innovative feature, the guiding plates. The device showed a good hysteretic behaviour and good dissipation energy capacity. The damage was concentrated on the dissipative element, the pin. The eye-bar plates suffered yielding and ovalization. Results showed a ductile failure due to bending for chamfered pin sections and a generally shear induced failure for welded circular pin sections. The bending of the eye-bar plates observed in previous research was successfully eliminated due to the implementation of spacers. Lateral displacements were significantly reduced due to the implementation of the guiding plates.

Numerical models were developed for a more in-depth evaluation of the bracing connection performance. Combined hardening was introduced to simulate the cyclic behaviour of the steel material and ductile damage criteria was introduced to simulate the failure of the pin. The simulations corroborated the promising results of the experimental tests. Python scripts were developed to automate some steps of the numerical modeling and postprocessing.

**Keywords:** Bracing connection, repairable dissipative devices, cyclic experimental tests, hysteretic behaviour, numerical modelling, ductile damage.





## Resumo

Com suporte no conhecimento desenvolvido em investigações anteriores, um novo dispositivo dissipativo e reparável de ligação coluna-contraventamento foi desenvolvido. Dando resposta à crescente exigência de segurança e resiliência de estruturas que minorizem os efeitos das acções sísmicas. Este dispositivo é aplicado em estruturas porticadas mistas de aço e betão, e contém um pino metálico transversal que dissipa energia através da sua plastificação.

De maneira a avaliar o comportamento local do dispositivo, estudos experimentais e numéricos de oito configurações diferentes foram desenvolvidos. Este estudo englobou duas geometrias do pino, chanfrada e circular, com diferentes configurações de soldas e um elemento inovador, as chapas de guia. Este dispositivo revelou bom comportamento histerético e boa capacidade de dissipação de energia. O dano foi localizado no elemento dissipativo, o pino. Os resultados mostraram uma rotura dúctil devido à flexão nas secções chanfradas e uma rotura por corte nas secções circulares. A deformação por flexão das chapas perfuradas observada em investigações anteriores foi eliminada com sucesso através da aplicação de espaçadores. Os deslocamentos laterais foram reduzidos com a aplicação de chapas de guia.

Os modelos numéricos foram desenvolvidos para uma avaliação mais aprofundada do desempenho do dispositivo. O endurecimento combinado foi introduzido para simular o comportamento cíclico do material metálico e o critério de dano “ductile damage” foi introduzido para simular a rotura do pino. As simulações apresentaram resultados correspondentes com os obtidos experimentalmente. Foram desenvolvidos scripts em Python para automatizar algumas etapas da modelação e do pós-processamento dos modelos numéricos.

**Palavras-chave:** Ligação coluna-contraventamento, dispositivos dissipativos reparáveis, testes experimentais cíclicos, comportamento histerético, modelação numérica, ductile damage.



# Contents

- Contents ..... ix**
- List of Figures ..... xiii**
- List of Tables ..... xix**
- List of Symbols ..... xxi**
- List of Acronyms ..... xxiii**
- 1. Introduction ..... 1**
  - 1.1. Scope ..... 1
  - 1.2. Personal motivations ..... 2
  - 1.3. Aims and objectives ..... 2
  - 1.4. Structure of the dissertation ..... 2
- 2. Literature Review ..... 3**
  - 2.1. Seismic Risk ..... 3
  - 2.2. Resilience in construction ..... 3
  - 2.3. Seismic protection strategies and devices ..... 3
  - 2.4. Previous research on dissipative hysteretic devices ..... 5
    - 2.4.1. EBF dissipative systems ..... 5
    - 2.4.2. MRF dissipative systems ..... 7
    - 2.4.3. CBF dissipative systems ..... 9
- 3. Experimental Studies ..... 17**
  - 3.1. Introduction ..... 17
  - 3.2. DBrC Specimen ..... 18
    - 3.2.1. Description ..... 18
    - 3.2.2. Predesign ..... 19
    - 3.2.3. Pin Section Geometry ..... 22
    - 3.2.4. Pin Material ..... 22
    - 3.2.5. Guiding Plates ..... 22
    - 3.2.6. Weld configurations ..... 23
    - 3.2.7. Load history ..... 23
  - 3.3. Material characterization ..... 24
    - 3.3.1. Tensile Tests ..... 24
    - 3.3.2. SOFMAN Components ..... 25
    - 3.3.3. IST Components ..... 26

3.4.	Experimental Setup .....	27
3.5.	Experimental Results.....	31
3.5.1.	Experimental Test 01R .....	32
3.5.2.	Experimental Test 15C .....	34
3.5.3.	Experimental Test 02R .....	36
3.5.4.	Experimental Test 03R .....	38
3.5.5.	Experimental Test 04R .....	40
3.5.6.	Experimental Test 16C .....	42
3.5.7.	Experimental Test 17C .....	44
3.5.8.	Experimental Test 18C .....	46
3.6.	Conclusions .....	48
<b>4.</b>	<b>Analysis of Experimental Results .....</b>	<b>51</b>
4.1.	Experimental test limitations.....	51
4.2.	Parameters of interpretation .....	51
4.3.	Behaviour assessment of the experimental test configurations .....	53
4.3.1.	Ductility .....	53
4.3.2.	Stiffness .....	55
4.3.3.	Resistance .....	56
4.3.4.	Energy Dissipation.....	57
<b>5.</b>	<b>Numerical Models .....</b>	<b>61</b>
5.1.	Introduction.....	61
5.2.	Finite Element Model.....	61
5.2.1.	Geometric properties .....	61
5.2.2.	Material properties .....	61
5.2.3.	Mesh, contact, interactions, boundary conditions and loads.....	64
5.2.4.	Type of analysis.....	65
5.2.5.	Output variables.....	65
5.3.	Numerical Results .....	66
5.3.1.	Chamfered section tests .....	66
5.3.2.	Circular section tests .....	67
<b>6.</b>	<b>Numerical-Experimental Comparison .....</b>	<b>69</b>
6.1.	Chamfered pin tests .....	69
6.2.	Circular pin test with welded sections .....	71
6.2.1.	Damage criteria .....	72
<b>7.</b>	<b>Conclusion and Further Developments .....</b>	<b>79</b>
7.1.	General conclusions .....	79

7.2. Further Developments .....	80
<b>References .....</b>	<b>81</b>
<b>Annex A .....</b>	<b>85</b>
<b>Annex B .....</b>	<b>89</b>
<b>Annex C .....</b>	<b>95</b>



# List of Figures

- Figure 2-1: Seismic protection strategies (adapted from Guerreiro, 2011). ..... 4
- Figure 2-2: (a) ADAS and (b) TADAS (Alehashem et al., 2008). ..... 6
- Figure 2-3: BSD connection scheme (Amiri et al., 2020). ..... 6
- Figure 2-4: The behaviour of structures equipped with BSD devices (Amiri et al., 2020)..... 6
- Figure 2-5: Replaceable bolted link (Taucer et al., 2014)..... 7
- Figure 2-6: SSD connection scheme (Oh et al., 2009). ..... 7
- Figure 2-7: Dual moment resisting frames with replaceable shear panels (Vayas et al., 2017). ..... 8
- Figure 2-8: FUSEIS1 system: (a) general layout, (b) assembly in frame structure, (c) beam link (FUSEIS1-1), (d) pin link (FUSEIS1-2) (Vayas et al., 2013). ..... 8
- Figure 2-9: FUSEIS2 system: (a) bolted beam splice (b) welded beam splice. .... 9
- Figure 2-10: BRB configuration (Kiggins and Uang, 2006). ..... 10
- Figure 2-11: CBF-MB system scheme (Vayas et al., 2017). ..... 10
- Figure 2-12: INERD U-connection: (a) experimental test, (b) pin connections within a frame (Calado et al., 2004)..... 11
- Figure 2-13: INERD pin connection: (a) experimental test, (b) pin connections within a frame (Calado et al., 2004)..... 12
- Figure 2-14: INERD pin connection: (a) one-interior plate and (b) two interior plates configurations (Vayas et al., 2017)..... 12
- Figure 2-15: Stages of loading of pin connection (Vayas et al., 2017)..... 13
- Figure 2-16: INERD issues: (a) bending of the exterior plates, (b) pinching (RFCS Project - Dissipable, 2017)..... 13
- Figure 2-17: (a) Schematic of a brace with WHPs installed on a frame (Vasdravellis et al., 2014) and (b) CSF-brace assembly (Gray et al., 2010)..... 14
- Figure 2-18: Dissipative double pin-connections: (a) pins in-parallel, (b) pins in-line. (Tirca et al., 2014). ..... 15
- Figure 3-1: Full list of experimental test specimens ..... 17
- Figure 3-2: Overall view of DRBrC installed in a frame (DISSIPABLE, 2018). ..... 18
- Figure 3-3: DRBrC overall view. .... 18
- Figure 3-4: DRBrC after the inclusion of the second interior spacer, the current configuration. .... 19
- Figure 3-5: Connection scheme: (a) top view and (b) side view. (DISSIPABLE, 2020a). ..... 19
- Figure 3-6: Moment diagram of the pin at the point of ultimate resistance. .... 20

Figure 3-7: DRBrC current configuration: (a) top view and (b) side view. Dimensions in mm. ....	21
Figure 3-8: Chamfered (R) and circular (C) pin sections. ....	22
Figure 3-9: Guiding plates .....	23
Figure 3-10: Tested weld configurations.....	23
Figure 3-11: Tensile test setup at LERM.....	24
Figure 3-12: Codename designation of the tensile test specimens. ....	25
Figure 3-13: Determination of yield strength using 0.2% offset line method.....	25
Figure 3-14: Tensile test specimen 13: (a) removed pin and (b) pin processing. ....	26
Figure 3-15: Tensile test specimen 15PIN235.....	27
Figure 3-16: Experimental test setup at LERM. ....	27
Figure 3-17: Fixed equipment scheme.....	28
Figure 3-18: Instrumentation: (a) Load cell, (b) LVDT1 and wire sensor, (c) LVDT2. ....	29
Figure 3-19: Instruments position and direction criterion. ....	29
Figure 3-20: Examples of equipment used: (a) computer setup, (b) control console and (c) data logger. .....	30
Figure 3-21: Codename for the experimental test configurations. ....	31
Figure 3-22: Experimental test 01R: (a) specimen model, (b) load history applied. ....	32
Figure 3-23: Experimental test 01R: (a) & (b) asymmetric loading, (c) pin elongation and (d) pin sliding. .....	33
Figure 3-24: Force-displacement curve for experimental test 01R. ....	33
Figure 3-25: Experimental test 15C: (a) specimen model, (b) load history applied. ....	34
Figure 3-26: Experimental test 15C: (a) GP1 position, (b) weld failure, (c) asymmetric loading and (d) exterior plate ovalization.....	35
Figure 3-27: Force-displacement curve for experimental test 15C. ....	35
Figure 3-28: Experimental test 02R: (a) specimen model, (b) load history applied. ....	36
Figure 3-29: Experimental test 02R: (a) pin deformation, (b) pin elongation, (c) & (d) pin failure. ....	37
Figure 3-30: Force-displacement curve for experimental test 02R. ....	37
Figure 3-31: Experimental test 03R: (a) specimen model, (b) load history applied. ....	38
Figure 3-32: Experimental test 03R: (a) asymmetric loading, (b) pin elongation, (c) & (d) pin failure. .	39
Figure 3-33: Force-displacement curve for experimental test 03R. ....	39
Figure 3-34: Experimental test 04R: (a) specimen model, (b) load history applied. ....	40



Figure 3-35: Experimental test 04R: (a) pin elongation, (b) pin deformation, (c) & (d) pin failure. ....	41
Figure 3-36: Force-displacement curve for experimental test 04R. ....	41
Figure 3-37: Experimental test 16C: (a) specimen model, (b) load history applied. ....	42
Figure 3-38: Experimental test 16C: (a) onset of failure of the pin, (b) failure mode (c) & (d) pin failure. ....	43
Figure 3-39: Force-displacement curve for experimental test 16C. ....	43
Figure 3-40: Experimental test 17C: (a) specimen model, (b) load history applied. ....	44
Figure 3-41: Experimental test 17C: (a) weld failure, (b) mid-span undeformed section, (c) & (d) pin failure. ....	45
Figure 3-42: Force-displacement curve for experimental test 17C. ....	45
Figure 3-43: Experimental test 18C: (a) specimen model, (b) load history applied. ....	46
Figure 3-44: Experimental test 18C: (a) pin elongation, (b) weld failure, (c) & (d) pin failure. ....	47
Figure 3-45: Force-displacement curve for experimental test 18C. ....	47
Figure 3-46: Guiding plates influence on lateral displacement. ....	49
Figure 3-47: Guiding plates influence on lateral displacement. ....	50
Figure 4-1: Equipment limitation: trimmed force-displacement curve. ....	51
Figure 4-2: Determination of the elastic parameters. ....	52
Figure 4-3: Parameters of interpretation for one cycle (ECCS, 1986). ....	53
Figure 4-4: Full ductility of chamfered pin tests. ....	54
Figure 4-5: Full ductility of circular pin tests. ....	54
Figure 4-6: Rigidity ratio for chamfered pin tests. ....	55
Figure 4-7: Rigidity ratio for circular pin tests. ....	56
Figure 4-8: Resistance ratio for chamfered pin tests. ....	56
Figure 4-9: Resistance ratio for circular pin tests. ....	57
Figure 4-10: Cumulative dissipated energy WT at the end of each cycle. ....	58
Figure 4-11: Absorbed energy ratio for chamfered tests. ....	59
Figure 4-12: Absorbed energy ratio for circular tests. ....	59
Figure 5-1: Evolution of isotropic and kinematic hardening for combined hardening model under uniaxial stress stress state (adapted from ABAQUS, 2012). ....	63
Figure 5-2: Boundary conditions and rupture: (a) plate element, (b) pin element. ....	63

Figure 5-3: Combined hardening calibration: (a) plate material, (b) SOFMAN pin material and (c) IST pin material. ....	64
Figure 5-4: Numerical model representation: (a) symmetry model for chamfered section configurations, (b) full model for circular section configurations. ....	65
Figure 5-5: Von Mises stresses for the numerical model of test 02R: (a) bracing under tension, (b) bracing under compression. ....	66
Figure 5-6: Normal stresses $\sigma_{33}$ for the numerical model of test 02R: (a) bracing under tension, (b) bracing under compression. ....	66
Figure 5-7: Equivalent plastic strains PEEQ for the numerical model of test 02R: (a) bracing under tension, (b) bracing under compression. ....	67
Figure 5-8: Von Mises stresses for the numerical model of test 16C: (a) bracing under tension, (b) bracing under compression. ....	67
Figure 5-9: Normal stresses $\sigma_{33}$ for the numerical model of test 16C: (a) bracing under tension, (b) bracing under compression. ....	68
Figure 5-10: Equivalent plastic strains PEEQ for the numerical model of test 16C: (a) bracing under tension, (b) bracing under compression. ....	68
Figure 6-1: Force-displacement curves comparison for test 02R. ....	69
Figure 6-2: Envelope curves comparison for test 02R. ....	70
Figure 6-3: Peak force for each half cycle comparison for test 02R. ....	70
Figure 6-4: Excursion for each half cycle comparison for test 02R. ....	71
Figure 6-5: Deformation of the pin in test 02R: (a) experimental test, (b) numerical model. ....	71
Figure 6-6: Force-displacement curves comparison for test 16C. ....	72
Figure 6-7: Stress-strain curve with progressive damage degradation (adapted from ABAQUS, 2012). ....	72
Figure 6-8: Tensile test rupture: (a) & (c) plate element, (b) & (d) pin element. ....	73
Figure 6-9: Damage criteria calibration: (a) plate elements, (b) pin element. ....	74
Figure 6-10: Force-displacement curves comparison for test 16C with implemented damage criteria. ....	75
Figure 6-11: Envelope curves comparison for test 16C with implemented damage criteria. ....	75
Figure 6-12: Excursion for each half cycle comparison for test 16C. ....	76
Figure 6-13: Peak force for each half cycle comparison for test 16C. ....	76
Figure 6-14: Failure mode of test 16C: (a) experimental test, (b) numerical model. ....	77
Figure 7-1: The evolution of the DRBrC device: guiding plates. ....	79

Figure A.-1:Engineering and true stress-strain curves for exterior plates material. ....	85
Figure A-2: Engineering and true stress-strain curves for end plates material. ....	85
Figure A-3: Engineering and true stress-strain curves for interior plates material. ....	86
Figure A-4: Engineering and true stress-strain curves for exterior spacers material. ....	86
Figure A-5: Engineering and true stress-strain curves for interior spacers material. ....	87
Figure A-6: Engineering and true stress-strain curves for SOFMAN pin material.....	87
Figure A-7: Engineering and true stress-strain curves for test specimen removed from an untested device corresponding to SOFMAN pin material. ....	88
Figure A-8: Engineering and true stress-strain curves for IST pin material.....	88
Figure B-1: Force-displacement curves comparison for test 01R. ....	89
Figure B-2: Force-displacement curves comparison for test 02R. ....	89
Figure B-3: Force-displacement curves comparison for test 03R. ....	90
Figure B-4: Force-displacement curves comparison for test 04R. ....	90
Figure B-5: Force-displacement curves comparison for test 15C. ....	91
Figure B-6: Force-displacement curves comparison for test 16C. ....	91
Figure B-7: Force-displacement curves comparison for test 16C with implemented damage criteria. .	92
Figure B-8: Force-displacement curves comparison for test 17C. ....	92
Figure B-9: Force-displacement curves comparison for test 18C. ....	93



# List of Tables

- Table 3-1: Forces and deflections of pin connection (Plumier et al., 2004). ..... 20
- Table 3-2: Predesign of the pin device. .... 20
- Table 3-3: Plates and spacers dimensions and material. .... 21
- Table 3-4: Pin dimensions and material. .... 21
- Table 3-5: ECCS load history (ECCS, 1986). .... 24
- Table 3-6: Dimensions of the SOFMAN tensile test specimens (dimensions in mm). .... 25
- Table 3-7: SOFMAN specimen tensile test data. .... 26
- Table 3-8: IST specimen tensile test data. .... 27
- Table 3-9: Measuring instruments configurations. .... 30
- Table 3-10: Tested specimens (adapted from DISSIPABLE, 2020c). .... 31
- Table 3-11: Results for experimental test 01R. .... 32
- Table 3-12: Results for experimental test 15C. .... 34
- Table 3-13: Results for experimental test 02R. .... 36
- Table 3-14: Results for experimental test 03R. .... 38
- Table 3-15: Results for experimental test 04R. .... 40
- Table 3-16: Results for experimental test 16C. .... 42
- Table 3-17: Results for experimental test 17C. .... 44
- Table 3-18: Results for experimental test 18C. .... 46
- Table 3-19: Dissipated energy and nr. of cycles obtained in each experimental test. .... 49
- Table 4-1: Elastic parameters of the tested devices. .... 52
- Table 5-1: Combined hardening parameters. .... 63
- Table 6-1: Damage parameters for the tensile tests. .... 74
- Table 6-2: Damage parameters for the numerical test 16C. .... 74
- Table 6-3: Numerical-experimental peak forces and dissipated energy comparison. .... 78



## List of Symbols

### Latin upper case letters

$A_i$	Area of a half cycle of the force-displacement curve, positive or negative
$C$	Kinematic hardening parameter
$D$	Damage parameter
$E$	Modulus of elasticity
$F_y$	Yield load, positive or negative
$G_f$	Fracture energy
$I$	Second moment of area of the pin cross section
$K_e$	Elastic stiffness, positive or negative
$L$	Equivalent length
$M_{pl}$	Plastic resistance moment of the pin
$PEEQ$	Equivalent plastic strain index
$P_{max}$	Maximum design load of the connection
$P_y$	Design yield load of the connection
$Q_{\infty}$	Isotropic hardening parameter
$W_i$	Absorbed energy for each half cycle, positive or negative
$W_{pl}$	Plastic section modulus
$W_t$	Total dissipated energy

### Latin lower case letters

$a$	Distance between the exterior the interior eye-bar plate
$b$	Pin width, Isotropic hardening parameter
$b_{ext}$	Width of the exterior eye-bar plates
$b_{int}$	Width of the interior eye-bar plates
$d_{ext}$	Axial distance between the exterior eye-bar plates
$d_{int}$	Axial distance between the interior eye-bar plates
$e_y$	Yield displacement, positive or negative (same as $\delta_y$ )
$f_u$	Tensile strength of the material
$f_y$	Yield strength of the material
$h$	Pin height
$h_{ext}$	Height of the exterior eye-bar plates
$h_{int}$	Height of the interior eye-bar plates
$l$	Axial distance between medial axis of exterior eye-bar plates
$s_{ext}$	Distance from the free edge of the exterior eye-bar plate and the edge of the hole
$s_{int}$	Distance from the free edge of the interior eye-bar plate and the edge of the hole
$t_{ext}$	Thickness of the exterior eye-bar plates
$t_{int}$	Thickness of the interior eye-bar plates
$tg\alpha_i$	slope at the change of sign in the force for each half cycle, positive or negative

$tg\alpha_y$	Tangent of the envelope curve at the origin, positive or negative
$\bar{u}^{pl}$	Equivalent true plastic displacement
$\bar{u}_f^{pl}$	Equivalent true plastic displacement at failure

#### Greek upper case letters

$\Delta e_i$	Excursion for each half cycle, positive or negative
$\Phi$	Pin diameter

#### Greek lower case letters

$\alpha$	Imperfection factor
$\bar{\alpha}$	Equivalent back stress
$\gamma$	Kinematic hardening parameter
$\delta_{II}$	Ultimate displacement
$\delta_{lim}$	Deformation capacity displacement
$\delta_y$	Yield displacement (same as $e_y$ )
$\bar{\varepsilon}^{pl}$	Equivalent plastic strain
$\bar{\varepsilon}_0^{pl}$	Equivalent plastic strain at the onset of damage
$\varepsilon_{eng}$	Engineering strain
$\varepsilon_i$	Resistance ratio, positive or negative
$\varepsilon_{ij}^p$	Plastic strain tensor
$\varepsilon_{true}$	True strain
$\varepsilon_u$	Strain at the ultimate stress
$\eta_i$	Absorbed energy ratio, positive or negative
$\mu_i$	Full ductility, positive or negative
$\xi_i$	Rigidity ratio, positive or negative
$\sigma$	(Damaged) Stress tensor
$\bar{\sigma}$	Equivalent stress or Von Mises stress
$\sigma^0$	Yield stress at zero plastic strain
$\sigma _0$	Initial yield surface size
$\sigma_{eng}$	Engineering stress
$\sigma_{ij}$	Stress tensor at each point
$\sigma_{true}$	True stress
$\sigma_u$	Ultimate stress
$\sigma_{VonMises}$	Von mises equivalent stress
$\sigma_{y0}$	Stress at the onset of damage



## List of Acronyms

ADAS	Added Damping and Stiffness
ADRS	Acceleration Displacement Response Spectrum
ASTM	American Society for Testing and Materials
BRB	Buckling-Restrained Brace
BSD	Block Slit Damper
CBF	Concentrically Braced Frames
CBF-MB	Concentrically Braced Frame with Modified Braces
CEN	Comité Européen de Normalisation
CSB	Crescent Shaped Braces
CSF	Cast Steel Yielding Fuse
DISSIPABLE	Fully Dissipative and Easily Repairable Devices for Resilient Buildings with Composite Steel-Concrete Structure (project acronym)
DRBrC	Dissipative Replaceable Bracing Connection
DUAREM	Full-scale Experimental Validation of Dual Eccentrically Braced Frame with Removable Links (project acronym)
EBF	Eccentrically Braced Frame
ECCS	European Convention for Constructional Steelwork
EPP	Elastic Perfectly Plastic
FEM	Finite Element Model
FUSEIS	Dissipative Devices for Seismic-Resistant Steel Frames (project acronym)
GP	Guiding Plate
INERD	Two Innovations for Earthquake Resistant Design (project acronym)
INNOSEIS	Innovative Anti-Seismic Devices and Systems (project acronym)
IST	Instituto Superior Técnico
LERM	Laboratório de Estruturas e Resistência de Materiais
LVDT	Linear Variable Differential Transformer
MATCH	Material Choice for Seismic Resistant Structures (project acronym)
MRF	Moment Resisting Frame
PNG	Portable Network Graphics (image file format)
PRECASTEEL	Prefabricated steel structures for low-rise buildings in seismic areas (project acronym)
RFCS	Research Fund for Coal and Steel
SSCD	Steel Self-Centering Device
SSD	Shear Slit Damper
STEELRETRO	Steel Solutions for Seismic Retrofit and Upgrade of Existing Constructions (project acronym)
TADAS	Triangular Added Damping and Stiffness
WHP	Web Hourglass Pin



# 1. Introduction

The dissipative devices offer advantageous seismic protection to structures. Hysteretic devices are amongst the most efficient and economical dissipative devices. The hysteretic devices aim to make use of the formation of plastic hinges in the dissipative element in order to concentrate the damage, otherwise suffered by the structure, in strategically selected zones. In addition, hysteretic devices are often small, when compared to the whole structure, which allows for easy repair. Therefore, the service life and resilience of the structure is improved.

Under seismic action, structures are submitted to imposed displacements. Consequently, high forces are originated that produce permanent deformations, local buckling and collapse of essential structural elements. These damages may lead to stability problems, structural collapse, loss of lives and economic drops. The structure may stand still if the damage is limited but the structural elements can be compromised. Therefore, the stability of the structure is affected threatening the safety it provides.

To mitigate the consequences suffered from the disastrous event dissipative devices offer an advantageous protection to the structure life period. The Dissipative Repairable Bracing Connection (DRBrC) device aims to make use of the formation of plastic hinges in the dissipative pin element. And thus, concentrate the damage suffered by the structure in strategically local places and prevent the buckling of the brace element. In addition, this device offers the possibility of a repair so that with the simple replacement of the device the service life and resilience of the structure is guaranteed.

## 1.1. Scope

This work is inserted in the DISSIPABLE project financed by the European Commission, within the Research Fund for Coal and Steel. It arises from the need to further investigate hysteretic dissipative devices intended to be applied to combined steel-concrete structures, focusing on the component level. The low-cost DRBrC device under investigation in this dissertation increases the life expectancy of the structures and their resilience. This device is applied in the brace-column connections of composite steel-concrete frames and acts like a fuse, focusing the damage caused by an earthquake in a way that the overall structure of a building is not strongly affected. The elements of the device are all constituted by steel and the main dissipative element is the pin. In the present dissertation all the elements of the device are made of carbon steel. Although in the DISSIPABLE project it is also being investigated the use of other materials like high strength steel or stainless steel. The pin is subjected to bending and thus the yielding is explored to achieve energy dissipation.

Previous research programs that are the foundation of this investigation led to the current design of the DRBrC. The first related study, the FUSEIS project, developed investigations on several devices with an identical mechanism of operation. In the following study, the INERD project, the original design of the DRBrC was introduced. Instituto Superior Técnico (IST) participated in the INERD project investigations with the task of experimentally access the local behaviour of the device. Finally, in the present project, DISSIPABLE, the objective is to access the issues on the pin device verified in the INERD project in order to improve the design, taking into account the energy dissipation and repair abilities.

## **1.2. Personal motivations**

This project encompasses several topics whose interest I have been deepening throughout my academic career, namely, in the areas of steel structures, structural analysis and seismic engineering. As an additional motivating factor, it has an experimental component together with computational modelling, that make this academic experience much more comprehensive and enriching. Finally, it is part of an international research project program, DISSIPABLE, part of the “Research Fund for Coal and Steel” program organized by the European Commission. In short, I consider it to be of great value to have the opportunity to work together with other students and researchers from universities and companies on the international spectrum such as Greece, Italy and Germany.

## **1.3. Aims and objectives**

The objective of this dissertation is to compare and evaluate the local performance of eight previously defined configurations of the DRBrC device. In an effort to assess the influence of different variables that define the configurations tested. The variables in question are both geometric and material properties. The pin section geometry, chamfered pin section or circular pin section, will be focused. Moreover, this work aims to offer a numerical model, developed based on the experimental studies, that is able to predict the behaviour of the device in order to create a reliable tool for the following studies on the dissipative device. In this regard damage criteria is investigated in order to predict failure of the pin device.

## **1.4. Structure of the dissertation**

This document is divided into seven chapters. It begins with a brief introduction to the study and its aims in the chapter one. Then, a review of the seismic protection approaches with a focus on different dissipation devices, grouped by structural system to which they apply, is presented in the second chapter. The experimental test studies on the DRBrC device, from the setup up to the obtained results, are described in chapter three. The fourth chapter explains the analysis of the experimental results regarding the pin device behaviour under cyclic loads. Then, the development of the numerical models in the finite element software analysis program ABAQUS is described in chapter five. In this chapter, the results obtained from the simulations are presented and discussed. Next, in chapter six, the results obtained in the numeric models are compared with those obtained in the experimental tests regarding one example for each pin section geometry of the DRBrC device, one chamfered pin configuration and one circular pin configuration. Finally, in chapter seven general conclusions are drawn, and further developments are suggested.

## **2. Literature Review**

### **2.1. Seismic Risk**

Earthquakes are highly unpredictable and one of the major causes of damage in structures, affecting economic, environmental, and social aspects of society. Seismic risk is, in many areas of the world, a reality that cannot be ignored, but rather requires appropriate protection measures. This concept is defined by the combination of three aspects:

- Hazard – probability of occurrence of earthquakes of certain characteristics during certain periods of time.
- Exposure – people and built environment exposed to earthquakes.
- Vulnerability – seismic resistance of the built environment.

Notably, in May 2012, Italy, a country with elevated seismic activity, suffered what is classified as one of the costliest earthquake sequences in history, although having registered relatively low magnitudes. This fact indicates that exposure and vulnerability dimensions are as relevant factors as the hazard dimension involved.

### **2.2. Resilience in construction**

Although there is a growing increase in technologies and regulations in order to minimize the seismic risk in structures, post-disaster recovery is still very impactful and expensive (RFCS Project - Dissipable, 2017).

The concept of resilience, discussed by Bruneau et al. who states "The term [resilience] implies both the ability to adjust to "normal" or anticipated levels of stress and to adapt to sudden shocks and extraordinary demands" (Bruneau *et al.*, 2004, p.3) addresses this issue. This way, increasing seismic resilience is a more in-depth concept than reducing seismic risk because it takes into account the post-disaster recovery in addition to earthquake-resistant capacity. In the case of life support infrastructures, for example, it is mandatory that after a seismic event, they recover their normal functions as soon as possible. Thus, seismic resilience becomes particularly important.

### **2.3. Seismic protection strategies and devices**

There are three different approaches to enhance the seismic behaviour of structures: increasing its resistance and/or ductility (A), introducing seismic isolation systems (B) or through energy dissipation devices (C) (Guerreiro, 2011). The effect of each different approach in the acceleration displacement response spectrum (ADRS) format of a building is depicted in Figure 2-1.

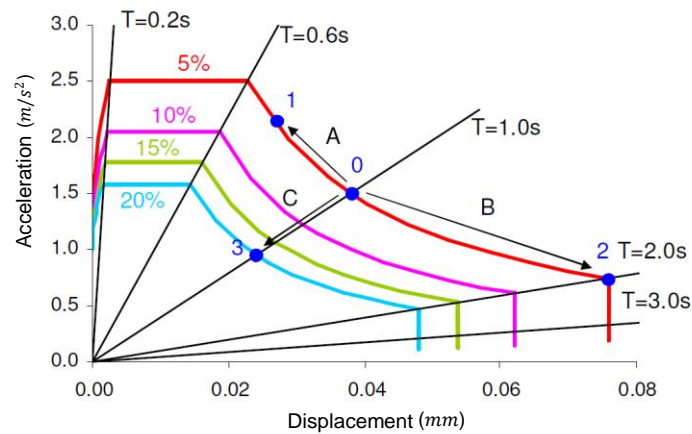


Figure 2-1: Seismic protection strategies (adapted from Guerreiro, 2011).

The application of conventional lateral-resistant structural systems follows the first approach (A). However, these systems alone have several limitations. It is the case of moment resisting frames (MRFs), concentrically (CBF) or eccentrically braced frames (EBFs) and shear walls. Although efficient, these structural systems use the inelastic deformation of the structural elements to dissipate energy, through the formation of plastic hinges, which can cause permanent damage to the structures. In these systems, reparability is often not feasible since the dissipative zones on conventional frames are heavy elements that carry gravity loads and thus difficult to handle and repair.

Seismic isolation systems (B) allow for an independence between the horizontal soil movement and the structure while energy dissipation devices (C) consist of systems introduced in the structure with the primary function of absorbing energy. These new seismic protection strategies, (B) and (C), act as complementary solutions together with the conventional systems and have been developed over the last four decades. In that way, recent regulations, such as Eurocode 8 (EN1998-1, 2004), outline its applications. These recent regulations place greater demands on non-collapse and damage limitation. Thus, the application of seismic protection systems is an efficient and economically viable alternative in strengthening these structures to seismic action (Franco, 2010). Although the seismic isolation design (B) prevents the propagation of deformations in structures in a more efficient way, it needs an absolute separation between the base and the upper building. Thus, seismic isolation may induce difficulties in structural design leading to additional construction measures and it is mostly only applicable on new constructions. Hence, the seismic energy dissipation technologies for mitigating seismic damages receive more applications in building engineering, exhibiting small interferences or modifications to the main structures. Energy dissipation devices (C) are frequently classified by their structural control technique such as passive, active or semi-active. Passive systems do not require exterior energy supply, active systems require exterior energy supply and operate based on sensors which are attached within the structures and semi active systems are a combination of both passive and active systems. Passive control systems have the advantage of presenting high reliability, reduced direct cost and reduced maintenance (Carvalho, 2017).

Passive energy dissipation devices can be considered velocity-dependent, the case of viscous dampers or displacement independent, the case of hysteretic dissipative devices. Hysteretic dissipative devices,

also referred as metallic dissipative or yielding devices, in virtue of their simplicity, are considered to be the most economical, applicable, and effective means of passive energy dissipation devices. They take advantage of the inelastic properties of metal materials to dissipate kinetic energy imposed by earthquakes, leaving main structural elements undamaged. These devices have the benefits of presenting a stable hysteretic behaviour, long-term reliability, low cost, insensitivity to ambient temperatures and finally, due to its simple concept, the materials and behaviour are familiar to practicing engineers. On the other hand, there are some drawbacks, the devices can be damaged after an earthquake event and may require replacement since the yielding is explored. Also, because it has a nonlinear behaviour, it may require nonlinear analysis (Symans et al., 2008). If necessary, most of yielding devices are meant to be replaced, and, as long as other structural members remain elastic, the building can be self-centered, with no residual storey displacement. Therefore, the repair time and cost would be minimized, and the building would be back to service rapidly (Shoeibi et al., 2017).

## **2.4. Previous research on dissipative hysteretic devices**

The first hysteretic dissipative devices for seismic protection of buildings were developed and implemented by Kelly and Skinner in 1972. One particular study carried out is the type C device (Kelly et al., 1972), which takes advantage of the flexural behaviour of short rectangular beams. These devices are intended to be installed in the diagonal bracings of steel frames, to deliver the energy absorption that would otherwise develop in the beam-column connections. The dissipated energy was estimated under controlled displacement cycling with the hysteresis loops recorded during each test.

### **2.4.1. EBF dissipative systems**

Based on the work of Kelly and Skinner, a wide variety of devices have been developed. The Added Damping and Stiffness device (ADAS) is the most well-known and used device for seismic prevention in buildings. It consists of a series of steel plates subjected to shear forces due to the lateral movement of the frame. The shear forces induce bending moments over the height of the plates. The geometrical configuration of the plates is such that bending moments produce a uniform flexural stress distribution over the height of the plates so that inelastic action occurs uniformly over the full height of the plates. For this to happen, if the plates are fixed-fixed, the geometry must have an hourglass shape. However, in case that the plates are fixed-pinned, the geometry must be triangular, and the device is called Triangular Added Damping and Stiffness (TADAS). ADAS and TADAS (Figure 2-2) are widely used today in Japan, USA, and Europe. The TADAS has been successfully applied in the energy-absorbing retainers for piping systems in nuclear power plants (Tehranizadeh, 2001) and in the Structural Engineering Association of California 2000's "Award for Excellence" recognized Core Pacific City shopping mall (Chang et al., 1999).

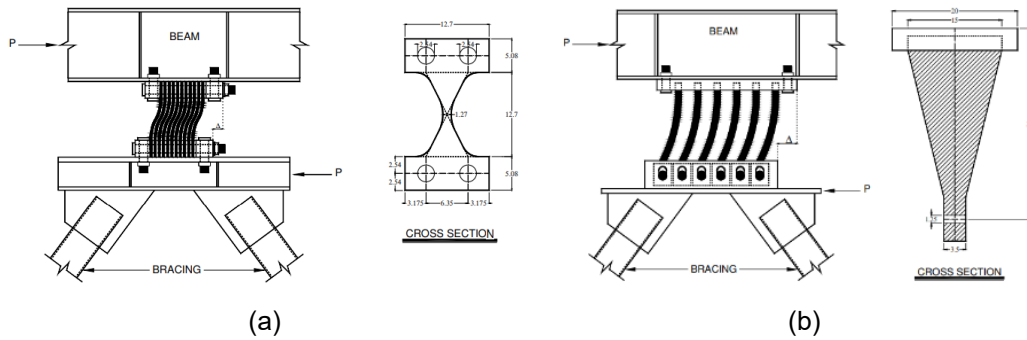


Figure 2-2: (a) ADAS and (b) TADAS (Alehashem et al., 2008).

Recently, Block Slit Damper (BSD) system was developed and evaluated experimentally and analytically (Amiri et al., 2020). This device consists of a steel block with several slits and two steel plates at the top and bottom of the block that connect the dissipative device to the beam and bottom of the block that connect the dissipative device to the structure (Figure 2-3).

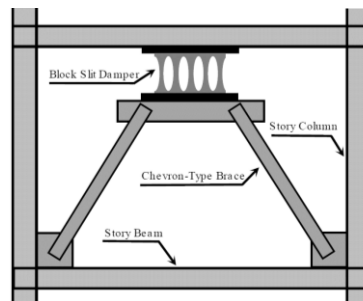


Figure 2-3: BSD connection scheme (Amiri et al., 2020).

In this work, Amiri showed that by applying hysteretic devices the simplified structural behaviour is described by a multi-linear curve, instead a bi-linear curve (Figure 2-4), due to the fact that hysteretic devices work in parallel with the bare structure. The multi-linear behaviour promotes the performance of the structure against quasi-resonance phenomenon in earthquakes. This means that the structure stiffness changes more often and consequently the period also changes more often, resulting in a reduced time range for the quasi-resonance phenomenon to occur.

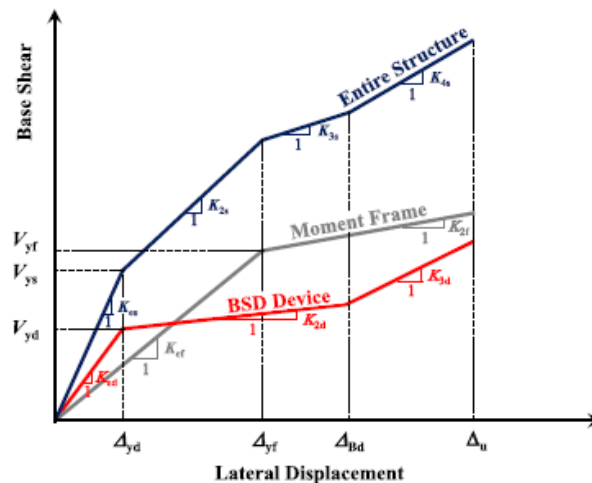


Figure 2-4: The behaviour of structures equipped with BSD devices (Amiri et al., 2020).



Another interesting dissipative device investigated is the replaceable bolted link (Taucer et al., 2014), a dual structure system, obtained by combining steel eccentrically braced frames (EBFs) equipped with removable bolted links (Figure 2-5), and moment resisting frames (MRFs). The bolted links are intended to provide the energy dissipation capacity and to be easily replaceable. The flexible MRFs provide the necessary re-centering capability to the structure, defined as the capacity of minimizing the residual displacement at the end of the seismic action. Dual re-centering EBFs with replaceable bolted links may be applied to multi-storey steel buildings.

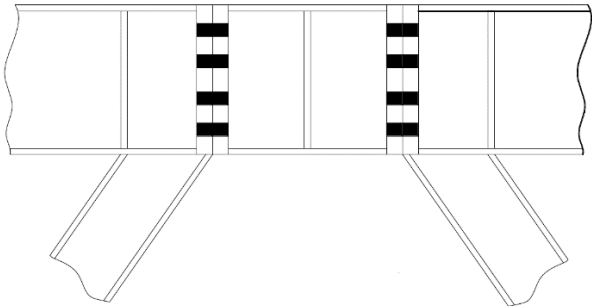


Figure 2-5: Replaceable bolted link (Taucer et al., 2014).

**2.4.2. MRF dissipative systems**

A relevant new beam-column connection system is the Shear Slit Damper (SSD). These replaceable devices consist of hollow steel plates that allow gravitational loads transferring from the beam to the column (Figure 2-6). The SSD keeps the structural elements in the elastic range and are best suited for tall buildings, since the load transfer mechanism of the structural system is not governed by shear forces, but by the bending moments. The seismic performance of this system was validated through full-scale cyclic tests and obtained an excellent hysteretic behaviour (Oh et al., 2009).

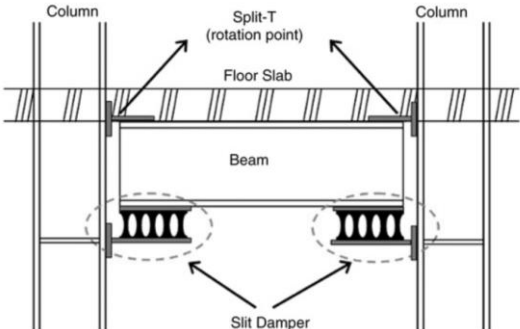


Figure 2-6: SSD connection scheme (Oh et al., 2009).

The replaceable shear panels system is a dual frame application where two replaceable shear panels are inserted inside moment resisting frames (Figure 2-7), providing additional lateral stiffness. The shear panels are bordered by additional vertical elements with simple connections at their ends to the beams. This innovative dual frame with shear panel may be applied to existing and new multi-storey steel moment resisting frames.

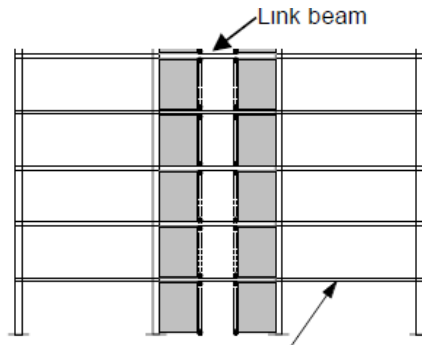


Figure 2-7: Dual moment resisting frames with replaceable shear panels (Vayas et al., 2017).

The FUSEIS1 system resembles a shear resistance wall but with the added advantages of energy dissipation. It is formed by two closely spaced strong columns rigidly interconnected by multiple links, that can be materialized through beam links with reduced beam sections (FUSEIS 1-1) or short pins links (FUSEIS 1-2) (Figure 2-8). This system resists lateral loads as a vertical Vierendeel beam. Dissipative elements are not generally subjected to vertical loads, as they are placed between floor levels. For appropriately selected sections of the FUSEIS1 system, sequential plastification may be achieved. Decisive design parameters of this system are the section types, material, length of the links and loading conditions. The innovative FUSEIS1 system may be applied to multi-storey steel buildings.

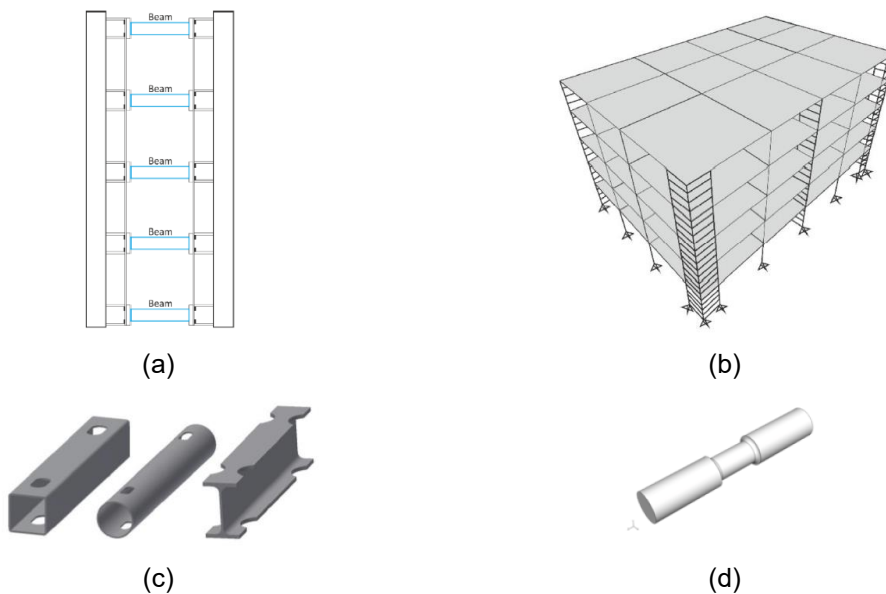


Figure 2-8: FUSEIS1 system: (a) general layout, (b) assembly in frame structure, (c) beam link (FUSEIS1-1), (d) pin link (FUSEIS1-2) (Vayas et al., 2013).

Under the same investigation project, another device, the FUSEIS2, was studied (Espinha, 2011). In the book edited by Vayas it stated that “This system is similar to the SSD, resembling “replaceable plastic hinges” for moment resisting frames” (Vayas et al., 2017).

The devices are made by introducing a discontinuity on the composite beams of a moment resisting frame and assembling the two parts of the beam through steel plates connected to the web and flange of the beam. Depending on the type of connection, FUSEIS2 is divided in two systems: FUSEIS bolted or welded beam splices (Figure 2-9).

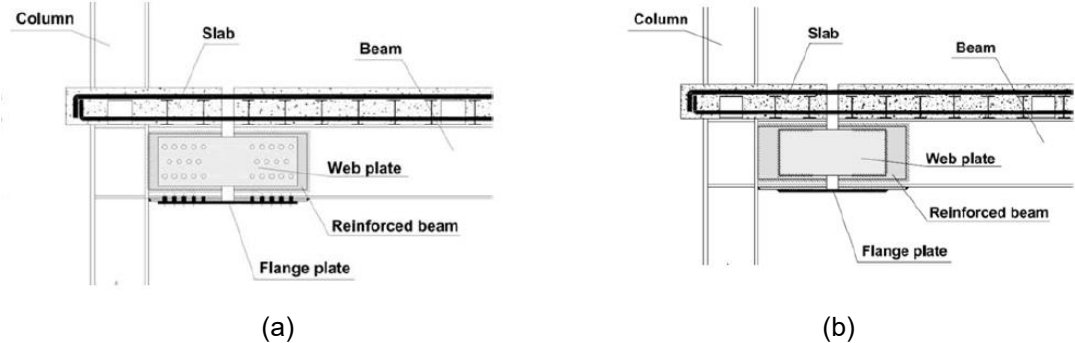


Figure 2-9: FUSEIS2 system: (a) bolted beam splice (b) welded beam splice.

To avoid cracking of the concrete in the dissipative area due to flexural deformation, a gap is placed in the concrete slab. The steel reinforcement is not interrupted in the gap section. The innovative dissipative system FUSEIS2 may be applied to multi-storey composite steel-concrete buildings with moment resisting frames.

Experimental tests on both FUSES1 and FUSEIS2 systems have been conducted during two European projects, FUSEIS (Vayas et al., 2013) and MATCH (Feldmann et al., 2017).

**2.4.3. CBF dissipative systems**

One of the most investigated concentrically braced frames dissipative systems is the buckling-restrained brace (BRB). This system consists of a steel surrounded by a stiff steel tube (Figure 2-10). The region between the tube and brace is filled with a concrete-like material and a special coating is applied to the brace to prevent it from bonding to the concrete. Thus, the brace can slide with respect to the concrete-filled tube. The confinement provided by the concrete-filled tube allows the brace to be subjected to compressive loads without buckling. Under compressive loads, the BRB behaviour is essentially identical to its behaviour in tension. Since buckling is prevented, significant energy dissipation can occur over a cycle of motion (Symans et al., 2008). The compression capacity of the BRB bracing system is actually found to be, to some extent, superior to the tension capacity, since the elements that are preventing the bending of the core absorb part of the stresses. However, there is an inherent complexity to the construction phase, which can induce poor performance due to possible geometric imperfections (Carvalho, 2017).

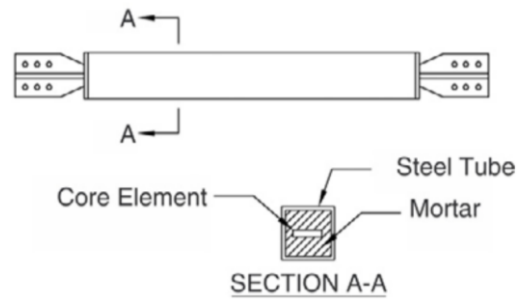


Figure 2-10: BRB configuration (Kiggins and Uang, 2006).

Based on traditional concentrically braced frames, the innovative concentrically braced frame with modified braces (CBF-MB), presented in Figure 2-11, can be described with two main features. The first innovation consists of the introduction of a horizontal intermediate member called splitting beam. The second innovation consists of the introduction of modified braces with variable “H”-shaped welded built-up cross-sections. The modified brace are the main dissipative elements while the splitting beam may partially participate. The CBF-MB systems are representative of the braced frames family. Their topology does not differ much from the topology of classical cross diagonal braced frame. In that sense, they may be successfully implemented in office and commercial buildings and in industrial constructions for pipe rack frames or engineering facilities (Vayas et al., 2017).

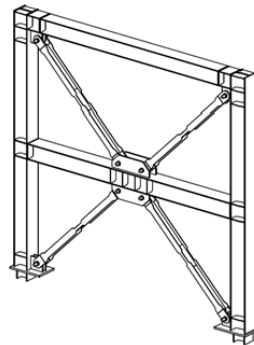


Figure 2-11: CBF-MB system scheme (Vayas et al., 2017).

Under the scope of the European Research Program of the Research Fund for Coal and Steel (RFCS), the INERD project (Plumier et al., 2004) introduced two innovative dissipative devices, the U and pin connections, that act as semi-rigid ductile brace-to-column connections for composite concentrically braced frames. The main purpose of these easy-repairable connections is to concentrate the damage in the correspondent predefined dissipative element, in the case of a strong seismic event, protecting the remaining structural elements from yielding and buckling. This project covered extensive experimental, numerical, and analytical studies, including multi-storey pushover analysis and non-linear dynamic analysis, resulting in the drafting of a preliminary Design Guide, technical reports and journal publications. Contrary to connections in conventional braced frames which must be stronger than the connected members and remain elastic, INERD connections are weaker than the connected members, exhibiting inelastic deformations and dissipating energy during seismic loading (Castiglioni et al., 2004).

All the structural elements besides the dissipative element of the connections are designed for capacity design forces according to the connection strength. Meaning that any repair works concentrate within the connections and thus are easier and inexpensive. In any case, the introduction of semi-rigid connections enhances further the structural flexibility. For this reason, the dissipative connections are better suitable for braced frames, such frames are sufficiently stiff to accommodate additional flexibility and may be protected from buckling. Additional advantages of INERD connections in comparison with conventional braced frames are the activation of all braces, either in compression or in tension, even at large storey drifts, reduction of overall structural costs and increased resilience for the same performance level (Vayas et al., 2017).

The INERD U-connection (Figure 2-12) consists of the dissipative element U-shaped thick plates with varying radius, length, thickness, and position and its design is essentially controlled by its deformation capacity. The investigations led to the general conclusion that the best performance of the U-device is obtained by increasing the thickness and decreasing the radius (Calado et al., 2004). This dissipative connection, due to its high deformability is intended to be applied in structures that are not too sensitive to large displacements, as is the case of multi-storey buildings with a limited number of floors.

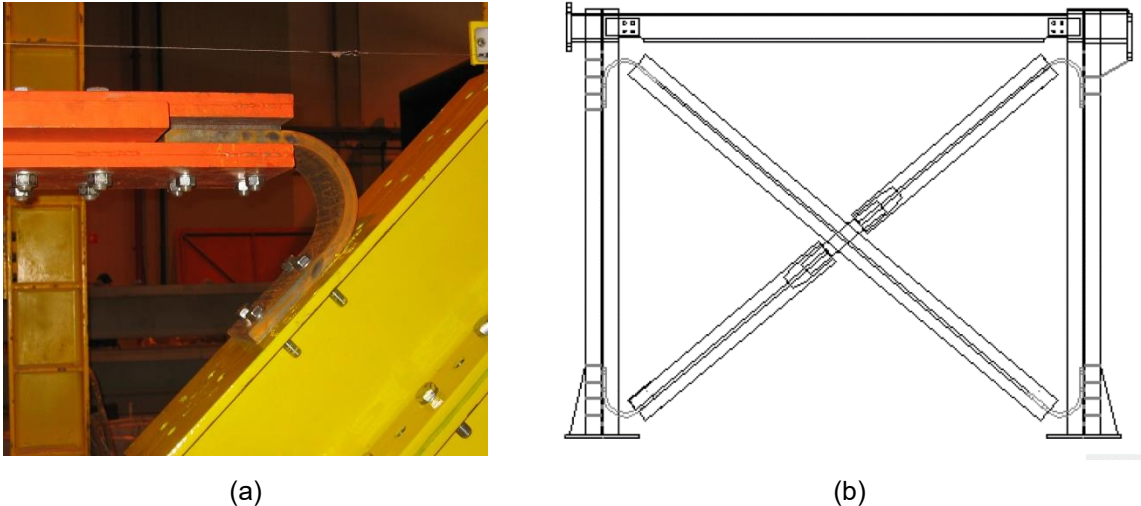
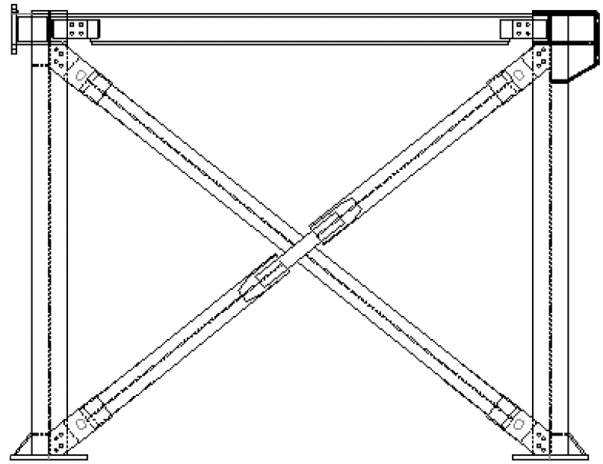


Figure 2-12: INERD U-connection: (a) experimental test, (b) pin connections within a frame (Calado et al., 2004).

Furthermore, the INERD pin connection (Figure 2-13) is materialized by a pair of exterior plates, connected to the column flanges, and one or two interior plates (Figure 2-14), connected to the brace. Last but foremost a pin, the dissipative element, is run through all the plates. The axial force of the bracing is transferred to the pin by the contact of the plates, which is this way subjected to bending and its yielding properties are explored. Under a strong seismic event, the damage is restricted to the pin allowing the INERD pin connections to be easily repaired with less material, time, and equipment.



(a)



(b)

Figure 2-13: INERD pin connection: (a) experimental test, (b) pin connections within a frame (Calado et al., 2004).

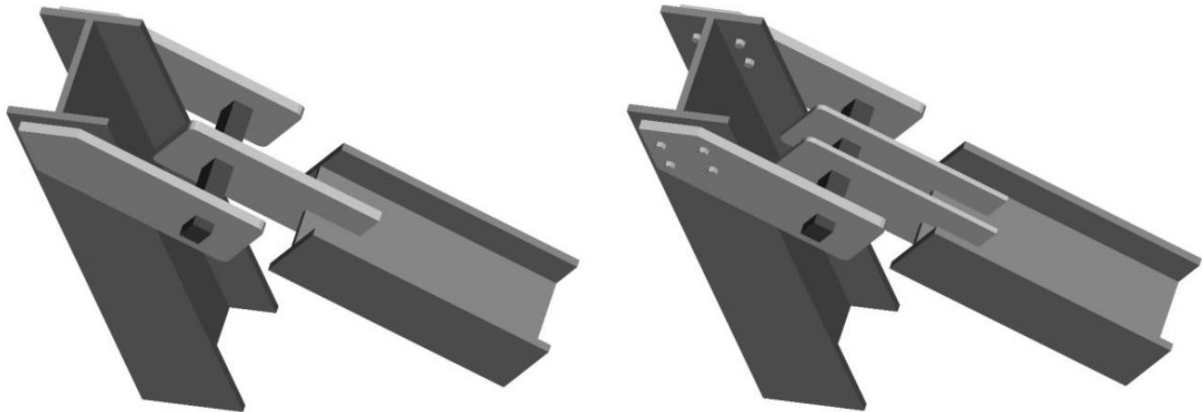


Figure 2-14: INERD pin connection: (a) one-interior plate and (b) two interior plates configurations (Vayas et al., 2017).

In order to demonstrate the response of the dissipative element, the pin, can be modelled with a beam (Figure 2-15). At the first stage of loading, the supports act as pinned, so the beam is simply supported, and the moment is concentrated at mid-span, when the acting moment reaches the plastic resistance moment of the pin, hinges are formed at the location of the interior plates and significant pin deformation takes place. At the second stage of loading, the end supports start to act as fixed, further increasing the connection resistance, until plastic hinges are also formed at the location of the exterior plates (supports). At the final stage of loading, the pin resistance has been fully exploited and the remaining stiffness of the connection is given due to the strain hardening and the expansion of the plastic zones.

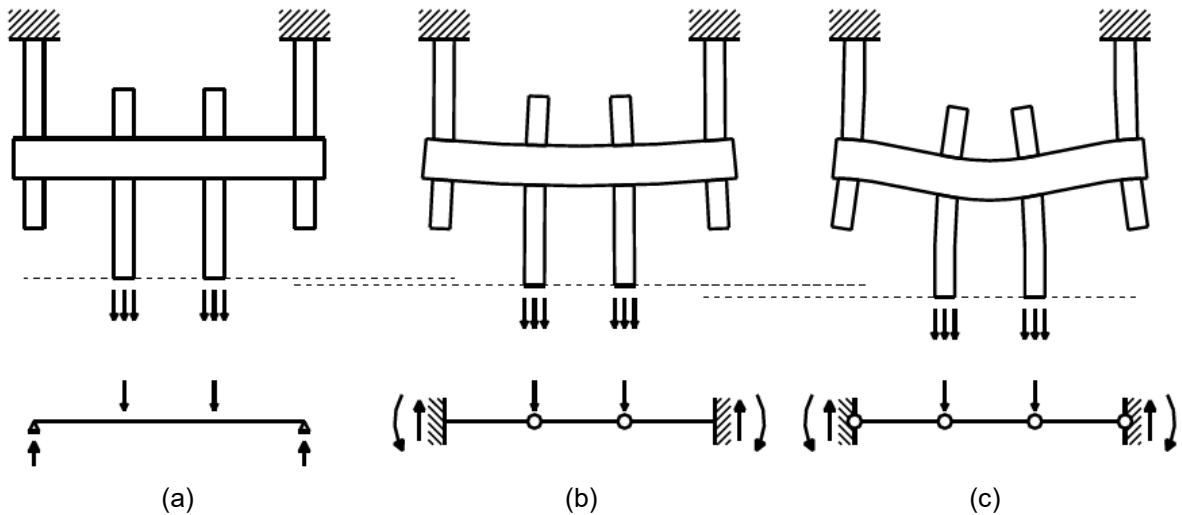


Figure 2-15: Stages of loading of pin connection (Vayas et al., 2017).

Consequently, since the resistance of the connection against axial force occurs through bending of the pin, it is independent of its direction. Two pin cross section geometries, chamfered and circular, with different dimensions, as well as different distance between the interior plates were investigated. The INERD pin connections proved to protect the braces against buckling and yielding, with the inelastic range limited at the region of the connections, mainly the pin. The position of the connections allows for easy inspection and, if necessary, replacement with low cost and short time, providing that the connection system is relatively light weight. Excellent hysteretic response was obtained, even for large deformations. The main issues discovered in the previous investigations of this system is the transverse bending of the steel plates through which the pin runs, and the bearing at the pin-plates interface because of slippage due to holes ovalization causing pinching of the hysteresis loops and therefore decreasing the energy dissipation capacity (Figure 2-16).

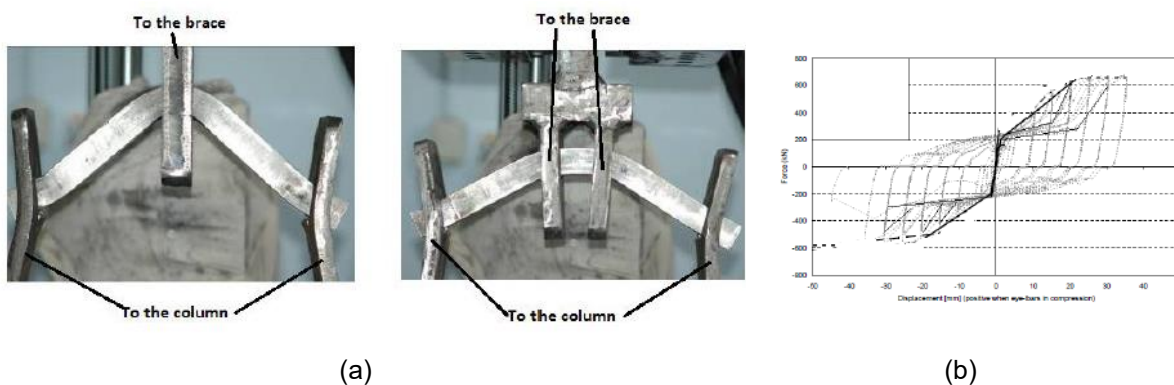


Figure 2-16: INERD issues: (a) bending of the exterior plates, (b) pinching (RFCS Project - Dissipable, 2017).

Moreover, the experimental investigations on the INERD pin connection under cyclic loading indicated that the pins with chamfered sections are preferable over the rectangular sections due to lower stress concentrations. Also, specimens with lower eye-bar plate holes tolerance exhibited better cyclic

behaviour. Finally, the innovative pin connection proved to be applicable to short, medium or high-rise steel buildings, as they demonstrate adequate stiffness and ductility (Vayas et al., 2017). Proposed modifications to the INERD pin devices based on the issues referred consist of using appropriate spacers between the exterior and interior eye-bar plates, that would not interfere with the assembling, in order to prevent the bending of the plates. Together with the introduction of end plates welded to the exterior and interior eye-bar plates and connected by means of bolts to the column and brace members, enabling an easier replacement of the device.

Similar energy dissipation devices to the INERD pin connections are the Web Hourglass Pin (WHP) and the Cast Steel Yielding Fuse (CSF) (Gray et al., 2010) (Figure 2-17). The first consists of cylindrical steel pins with hourglass-shape bending parts. Possible applications are to equip bracing members with this system or use it as the dissipative element of a steel self-centering device. Experimental tests on WHPs made of high-strength steel and stainless steel showed their very good energy dissipation and fracture capacities (Vasdravellis et al., 2014). The latter is a new seismic device for concentrically braced frames, which is designed to achieve a stable symmetric inelastic response through the flexural yielding of specially designed pin elements, intended to eliminate the cyclic tensile yielding and inelastic compressive buckling of traditional braces.

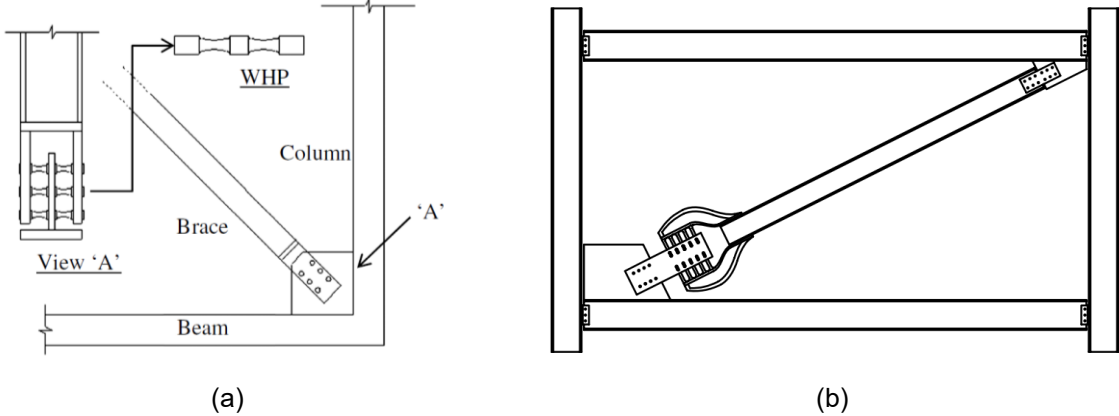


Figure 2-17: (a) Schematic of a brace with WHPs installed on a frame (Vasdravellis et al., 2014) and (b) CSF-brace assembly (Gray et al., 2010)

Based on the INERD pin connection, a double-pin connection device with pins placed in-parallel and inline (Figure 2-18) was proposed. This new approach aims to sustain larger axial forces that may need to be transferred from braces to CBF columns through the connections (Tirca et al., 2014). With the recourse to numerical models validated through the experimental results on the INERD device, it was found that doubling the pin member and employing the parallel configuration, the load-carrying capacity of connection increases two times. Additionally, the deflection is similar to that experienced by an equivalent single-pin device. Alternatively pins placed in-line show lower stresses and strains than an equivalent single-pin device.



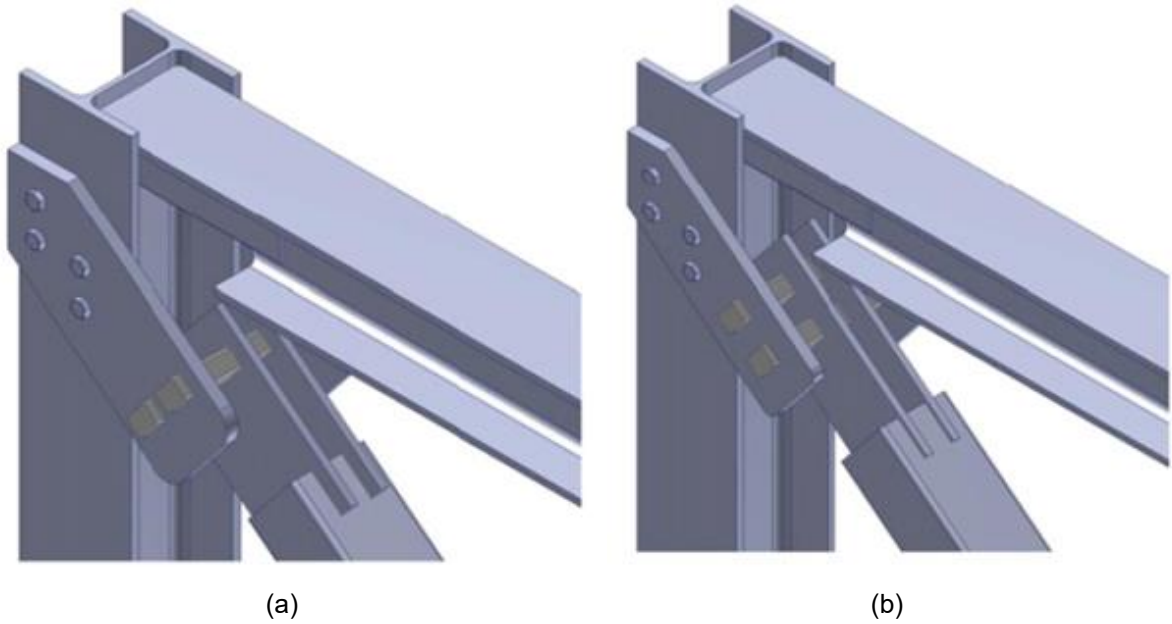


Figure 2-18: Dissipative double pin-connections: (a) pins in-parallel, (b) pins in-line. (Tirca et al., 2014).

As evidenced in this brief summary, there are today numerous forms of dissipation devices developed and investigated. However, although they are already outlined in the Eurocode (EN1998-1, 2004), their application is still very limited. This may be due to being a relatively recent technology, or due to the quiet and unalarming nature of the seismic risk that does not catalyze the need for this type of safety technologies. It is therefore important that the largest number of experimental and numerical studies continue to be carried out so that more evidence on the remarkable benefits that these devices offer in the mitigation of the devastating seismic action.



### 3. Experimental Studies

#### 3.1. Introduction

The experimental studies presented in this work started in November 2019 at Laboratório de Estruturas e Resistência de Materiais (LERM) of Instituto Superior Técnico (IST), as part of the DISSIPABLE project calendar (RFCS Project - Dissipable, 2017). These studies establish the first phase of experimental tests with the objective of evaluating the local behaviour of the DRBrC (Dissipative Replaceable Bracing Connection) device and are constituted by eight different pin device configurations presented in Figure 3-1.

The process can be divided into two stages:

- o Characterization of the material through tensile tests.
- o Experimental tests on the pin device.

No of test configuration	Configuration code (*)	Pin shape	Pin $\Phi$	Pin steel	External plate thickness	External plate dimensions	Number of internal plates	Internal plate thickness	External plate dimensions	Plates steel	Load protocol
1	R_S235_S355_E	R	50	S235	30	220x300	2	20	140x300	S355	E
2	R_S235_S355_C1	R	50	S235	30	220x300	2	20	140x300	S355	C1
3	R_S235_S355_C2	R	50	S235	30	220x300	2	20	140x300	S355	C2
4	R_S235_S355_C3	R	50	S235	30	220x300	2	20	140x300	S355	C3
5	R_S235_HSS_E	R	50	S235	30	220x300	2	20	140x300	HSS	E
6	R_S235_HSS_C1	R	50	S235	30	220x300	2	20	140x300	HSS	C1
7	R_S235_HSS_C2	R	50	S235	30	220x300	2	20	140x300	HSS	C2
8	R_S235_HSS_C3	R	50	S235	30	220x300	2	20	140x300	HSS	C3
9	R_SiS_S355_E	R	50	SiS	30	220x300	2	20	140x300	S355	E
10	R_SiS_S355_C1	R	50	SiS	30	220x300	2	20	140x300	S355	C1
11	R_SiS_S355_C2	R	50	SiS	30	220x300	2	20	140x300	S355	C2
12	R_SiS_HSS_E	R	50	SiS	30	220x300	2	20	140x300	HSS	E
13	R_SiS_HSS_C1	R	50	SiS	30	220x300	2	20	140x300	HSS	C1
14	R_SiS_HSS_C2	R	50	SiS	30	220x300	2	20	140x300	HSS	C2
15	C_S235_S355_E	C	50	S235	30	220x300	2	20	140x300	S355	E
16	C_S235_S355_C1	C	50	S235	30	220x300	2	20	140x300	S355	C1
17	C_S235_S355_C2	C	50	S235	30	220x300	2	20	140x300	S355	C2
18	C_S235_S355_C3	C	50	S235	30	220x300	2	20	140x300	S355	C3
19	C_S235_HSS_E	C	50	S235	30	220x300	2	20	140x300	HSS	E
20	C_S235_HSS_C1	C	50	S235	30	220x300	2	20	140x300	HSS	C1
21	C_S235_HSS_C2	C	50	S235	30	220x300	2	20	140x300	HSS	C2
22	C_S235_HSS_C3	C	50	S235	30	220x300	2	20	140x300	HSS	C3
23	C_SiS_S355_E	C	50	SiS	30	220x300	2	20	140x300	S355	E
24	C_SiS_S355_C1	C	50	SiS	30	220x300	2	20	140x300	S355	C1
25	C_SiS_S355_C2	C	50	SiS	30	220x300	2	20	140x300	S355	C2
26	C_SiS_HSS_E	C	50	SiS	30	220x300	2	20	140x300	HSS	E
27	C_SiS_HSS_C1	C	50	SiS	30	220x300	2	20	140x300	HSS	C1
28	C_SiS_HSS_C2	C	50	SiS	30	220x300	2	20	140x300	HSS	C2

Dimensions in mm and steel grades in MPa

(\*) Configuration code according to: #PinShape\_#PinSteelGrade\_#PlatesSteelGrade\_#LoadProtocol

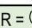
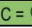
Color codes		
Protocol	Pin section	Steel grade
E = ECCS	R =  Chamfered	S235
C1 = Constant 1	C =  Circular	SiS
C2 = Constant 2		S355
C3 = Constant 3		HSS

Figure 3-1: Full list of experimental test specimens

### 3.2. DBrC Specimen

#### 3.2.1. Description

The DRBrC connection is an evolution of the previous RFCS project design, INERD (Plumier et al., 2004), used between a brace of a frame structure and its column (Figure 3-2).

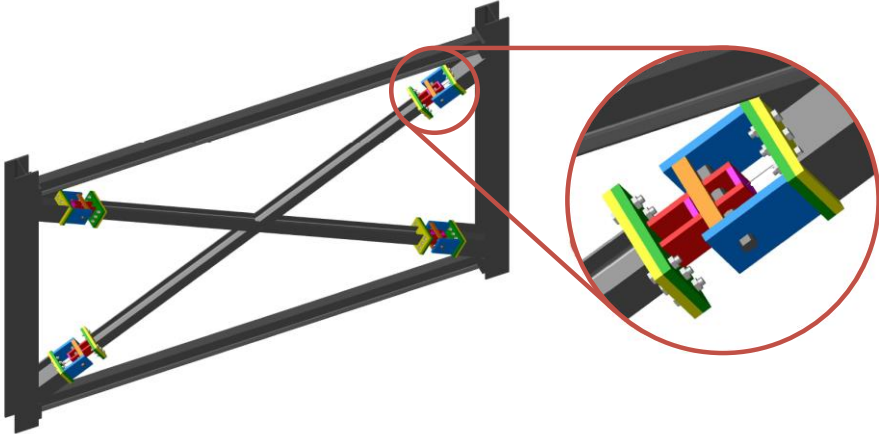


Figure 3-2: Overall view of DRBrC installed in a frame (DISSIPABLE, 2018).

In the DRBrC connection a pin, the dissipative element, is subjected to four-point bending which behaves in a relatively simple and predictable way, resembling a beam. The energy dissipation is thus obtained by accumulation of permanent plastic deformations in the pin, as referred in chapter two. The DRBrC dissipative device is meant to be applied in steel or combined steel-concrete concentrically braced frames. In order to take advantage of the accommodation of displacements that these systems offer.

The Figure 3-3 represents the DRBrC pin device configuration. This device consists of two end plates, in yellow, which are bolted to the structure elements, the brace and the column. One end plate is welded to the exterior eye-bar plates, in blue, and the other end plate is welded to the interior eye-bar plates, in red. Both exterior and interior eye-bar plates have welded spacers, to prevent bending, in orange and pink respectively. Finally, the dissipative pin, in grey, is placed through the eye-bar plates, completing the dissipative device. Thus, the outer housing of the device is formed by the pair of exterior plates and exterior spacer, and the inner housing is formed by the pair of interior plates and interior spacer.

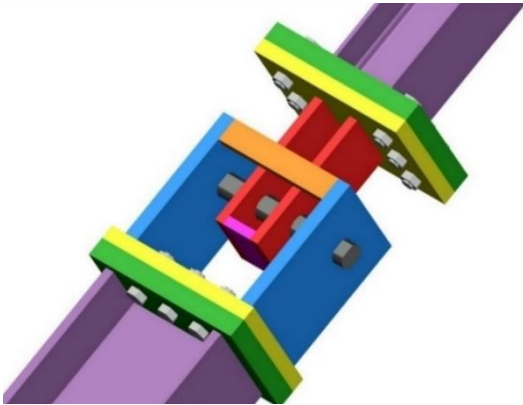


Figure 3-3: DRBrC overall view.

The main upgrade of this design evolution in the dissipative device is that it can be fully replaced (DISSIPABLE, 2018) due to the bolted connection with both the brace and the column. Whereas the INERD pin device used weld connections to the brace element. Studies with the use of numerical models (DISSIPABLE, 2020a) allowed for an upgrade on the configuration of the pin device, showing evident advantages, which is the inclusion of a second interior spacer, as presented in Figure 3-4. This showed improvements on the buckling of the interior eye-bar plates, and so this new element is implemented in all the configurations tested in the present studies.

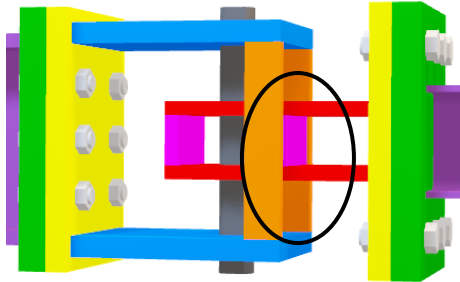


Figure 3-4: DRBrC after the inclusion of the second interior spacer, the current configuration.

**3.2.2. Predesign**

The dimensions that define the dissipative device are presented in the Figure 3-5.

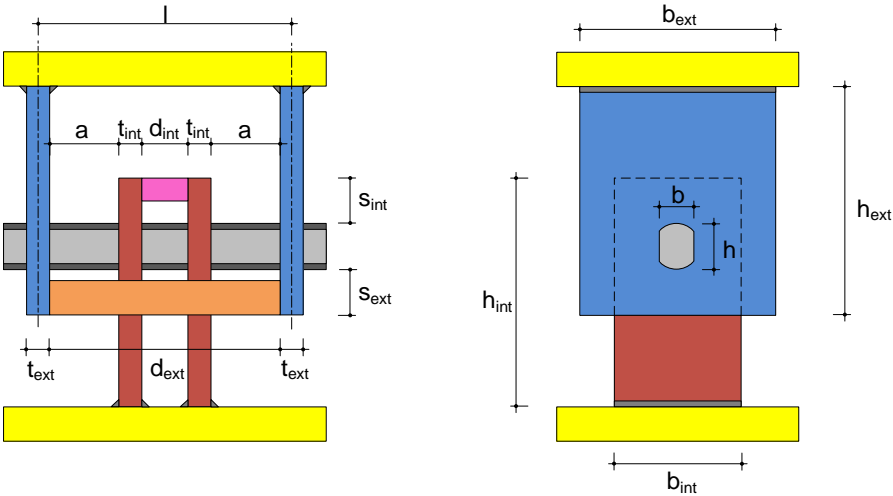
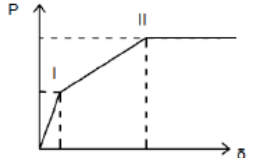


Figure 3-5: Connection scheme: (a) top view and (b) side view. (DISSIPABLE, 2020a).

The storey height, layout length, masses and other variables that affect the seismic behaviour ought to be assessed in order to design the dissipative device.

In this present work, the pin design is governed by its ultimate force, that must not exceed the maximum capacity of the load cell available at the laboratory, 500 kN for either compression or tensile directions. This requirement was verified taking into consideration the pin connection ultimate resistant force definition presented in Table 3-1 and the moment diagram of the simplified beam model depicted on Figure 3-6, where  $a$  is the distance between the exterior and the interior eye-bar plates.

Table 3-1: Forces and deflections of pin connection (Plumier et al., 2004).

	Force P	Deformations $\delta$
Point I "yielding y"	$P_y = \frac{2 \cdot M_p}{a}$	$\delta_y = 1,5 \cdot \frac{M_p \cdot l^2 \cdot \alpha}{EI} \cdot (3 - 4\alpha)$
Point II "ultimate u"	$P_u = \frac{4 \cdot M_u}{a}$	$\delta_{II} = 0,2 \cdot a$
Deformation capacity		$\delta_{lim} = 0,4 \cdot a$

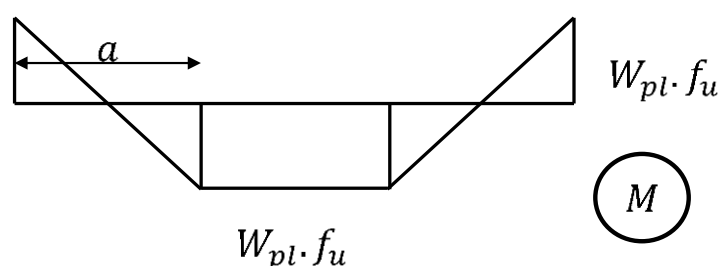


Figure 3-6: Moment diagram of the pin at the point of ultimate resistance.

Taking the requirement above exposed into consideration, two pin sections, further discussed in section 3.1.3, were designed. The pin material considered was S235 steel grade and the remaining elements material was S355 steel grade, following the capacity design philosophy, to make sure that the formation of the dissipative zone occurs in the pin element. This way, the relevant dimensions and the verification that imposes the design of the pin device for this study are presented in Table 3-2. These dimensions are also considered for comparison purposes, being identical to the pin dimensions in the experimental tests performed along INERD studies (Calado et al., 2004).

Table 3-2: Predesign of the pin device.

	$f_u$ (MPa)	$b$ (mm)	$h$ (mm)	$\Phi$ (mm)	$a$ (mm)	$W_{pl}$ (mm <sup>3</sup> )	$M_u = W_{pl} \cdot f_u$ (kNm)	$P_u = \frac{4 \cdot M_u}{a}$ (kN)	$P_{max}$ (kN)
Chamfered section (R)	360	40	50	-	80	2.0E+04	7.1	354	< 500
Circular section (C)	360	-	-	50	80	2.1E+04	7.5	375	< 500

Also, following the guidelines presented in the INERD Design Guide (Plumier et al., 2004) and further developed in ECCS INNOSEIS book (Vayas et al., 2017) the pin dimensions are selected so that:

Minimum distance between plates:

$$a = 80 \text{ mm} \geq h = 50 \text{ mm} \quad (3.1)$$

Thickness of exterior plates:

$$t_{ext} = 30 \text{ mm} \geq 0.75 h = 0.75 * 50 = 25 \text{ mm} \quad (3.2)$$

Thickness of interior plates:

$$t_{int} = 20 \text{ mm} \geq 0.5 t_{ext} = 0.5 * 30 = 15 \text{ mm} \quad (3.3)$$

Hence, the current DRBrC configuration design, with chamfered section, is achieved (Figure 3-7). The circular section configuration is identical with the only variation in the pin section and the exterior plates holes that are circular with a 50 mm diameter. The dimensions and material of the plate elements and the pin elements are summarized in Table 3-3 and Table 3-4, respectively.

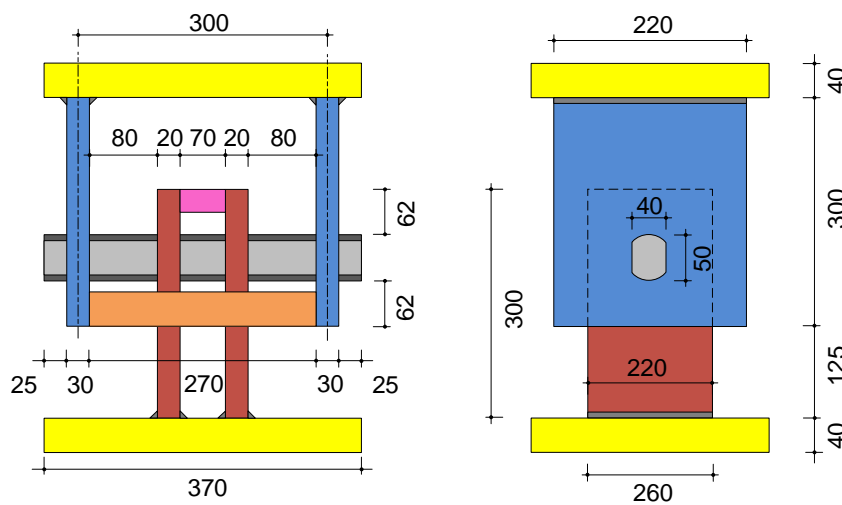


Figure 3-7: DRBrC current configuration: (a) top view and (b) side view. Dimensions in *mm*.

Table 3-3: Plates and spacers dimensions and material.

Element	Acronym	Height ( <i>mm</i> )	Width ( <i>mm</i> )	Thickness ( <i>mm</i> )	Material
End Plates	EndP	370	260	40	S355
Exterior Plates	EP	300	220	30	S355
Interior Plates	IP	300	140	20	S355
Exterior Spacer	ES	270	50	20	S355
Interior Spacers	IS	140	70	20	S355

Table 3-4: Pin dimensions and material.

Element	<i>h</i> ( <i>mm</i> )	<i>b</i> ( <i>mm</i> )	$\Phi$ ( <i>mm</i> )	Length ( <i>mm</i> )	Material
Chamfered Pin	50	40	-	380	S235
Circular Pin	-	-	50	380	S235

Next sections provide a brief description of the different configuration parameters tested, setting out the reasons and implications these parameters may offer to the pin device performance.

### 3.2.3. Pin Section Geometry

The experimental studies encompass two types of pin section geometry:

The chamfered pin section (R) and the circular pin section (C) configurations (Figure 3-8).

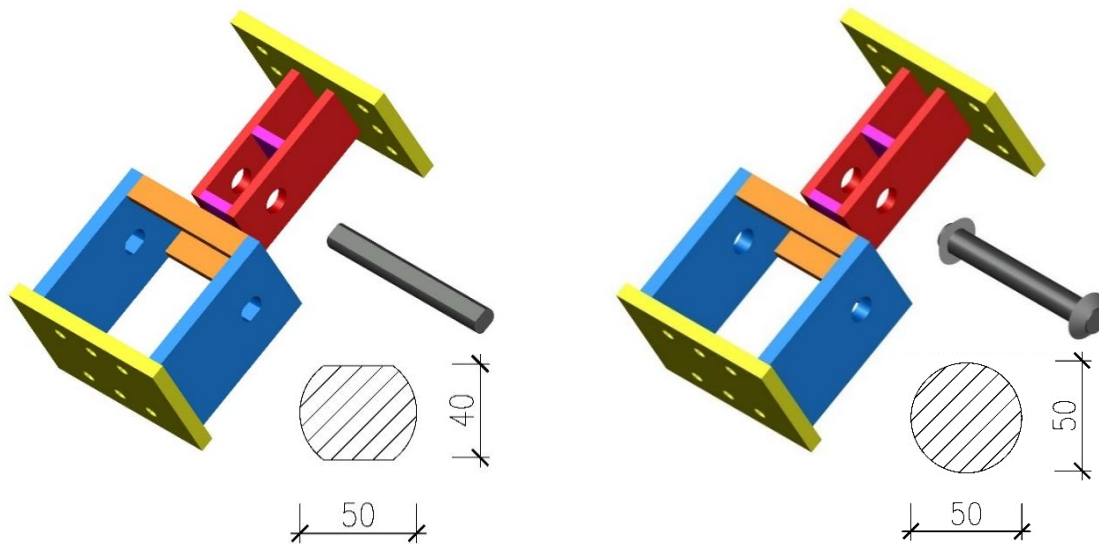


Figure 3-8: Chamfered (R) and circular (C) pin sections.

The chamfered section is in essence the circular sections with two flattened faces. Because the hole in these plates has the pin cross-section shape, with a slight gap, the chamfered pin behaves as fixed end in the exterior eye-bar plates, which restrain possible uncontrolled rotations of the pin along its axis. For the interior eye-bar plates, the brace can rotate as the hole in these plates is circular, preventing the transmission of torsion stresses to the pin. On the other hand, the circular section is fixed through different weld configurations introduced in section 3.1.5.

### 3.2.4. Pin Material

In the first two experimental tests, SOFMAN pin material was used. For the remaining tests, IST pin material was used for the reasons explained in section 3.4.3.

### 3.2.5. Guiding Plates

During the first experimental tests performed there was a considerable non-symmetric behaviour of the pin device. To solve this problem, new elements, entitled guiding plates, were considered (Figure 3-9). Firstly, two vertical plates, in dark blue, entitled GP1, were considered, which are welded on the exterior spacers and make the inner housing of the device have a more limited lateral clearance. Improvements were obtained, but they were not enough to solve the non-symmetric behaviour. Thus, a second group of guiding plates, in green, entitled GP2, was developed. This group is composed by a plate that is welded in the inner zone of the inner housing, also limiting the lateral clearance of the device, through the contact of the GP2 with the faces of the exterior eye-bar plates.



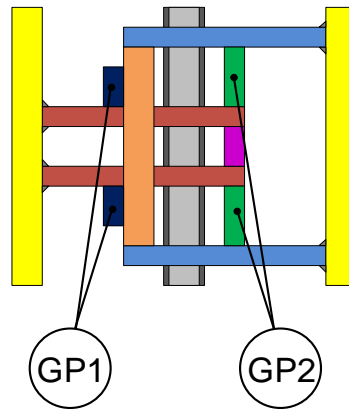


Figure 3-9: Guiding plates

### 3.2.6. Weld configurations

In the case of circular pin sections, in order to test different pin fixing solutions, three weld configurations, presented in Figure 3-10, were considered. In the experimental test 15C and 17C only exterior welds were applied, this weld configuration is referred to as W1. On the experimental test 16C the pin device was welded on the exterior and the interior, referred to as weld configuration W2. Finally, in the experimental test 18C only one exterior weld was applied, allowing the pin to freely rotate and elongate on the other extremity. This weld configuration is referred to as W3.

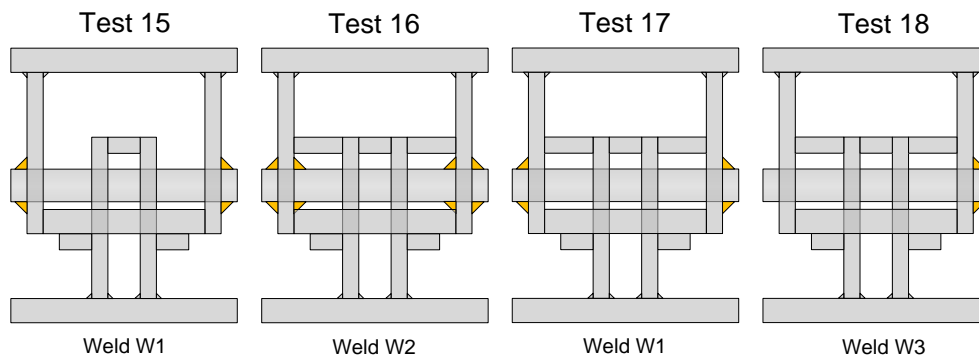


Figure 3-10: Tested weld configurations.

### 3.2.7. Load history

The load histories applied differ in whether it is a constant cyclic test or a hysteretic cyclic test based on the ECCS (European Convention for Constructional Steelwork) protocol (ECCS, 1986). The ECCS hysteretic cyclic load history is applied in order to standardize and better analyze the results. This protocol provides tools for easily comparing between experimental tests. The protocol is composed by a sequence of cycles presented in Table 3-5.

As it is a uniaxial cyclic test, it is not relatively interesting to do monotonic tests to determine the elastic parameters. These elastic parameters, mainly the value of the yielding displacement  $\delta_y$  that will define the cyclic test protocol, can be easily determined analytically with the expression in Table 3-1. For the pin with S235 grade steel was determined that  $\delta_y = 2.5 \text{ mm}$ .

Table 3-5: ECCS load history (ECCS, 1986).

Step	Imposed displacement interval	Number of Cycles
1	$+\frac{1}{4}\delta_y, -\frac{1}{4}\delta_y$	1
2	$+\frac{2}{4}\delta_y, -\frac{2}{4}\delta_y$	1
3	$+\frac{3}{4}\delta_y, -\frac{3}{4}\delta_y$	1
4	$+\delta_y, -\delta_y$	3
5	$+2\delta_y, -2\delta_y$	3
>5	$+(2 + 2n)\delta_y, -(2 + 2n)\delta_y, n = 1, 2, \dots$	3

Due to the limitations of the laboratory equipment, as it is explained in section 4.1, some load histories, mainly for the circular pin section tests, had to be adapted. For this reason, the load history for each experimental test is presented along with the results.

### 3.3. Material characterization

The main purposes of this step are:

- Evaluate the actual stresses of the materials.
- Serve as reference to develop the constitutive relations of the numerical models.

The materials prescribed have been chosen, as explained in section 3.1.1, to satisfy the design guidelines that were previously defined on previous projects, and considering the laboratory equipment capabilities. In this work the tensile tested material elements are referred as tensile test specimens and the tested pin device configurations as test specimens. The tensile test specimens relate to the different elements of the pin device. With the stress-strain curves obtained from the tensile tests it is possible to define characterization parameters of the pin device behaviour. Not only this, but the tensile tests are useful to the calibration process of the numerical models.

#### 3.3.1. Tensile Tests

The tensile tests were performed using the INSTRON testing machine, presented in the Figure 3-11, available at LERM with 250 kN capacity.



Figure 3-11: Tensile test setup at LERM.

Standard tensile tests were performed following the European Standard for tensile testing of metallic materials (EN10002-1, 2001) that indicates the presentation of the following information for each test:

- Identification of the tensile test specimen.
- Specified material.
- Type of tensile test specimen.
- Test results (Annex A).

The codename of the test specimens represents the number of the test specimen, the corresponding element type and the steel grade prescribed (Figure 3-12).

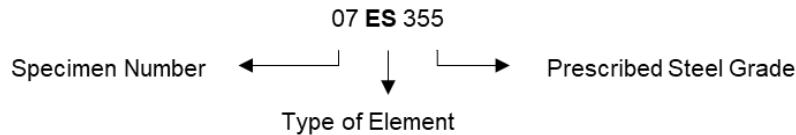


Figure 3-12: Codename designation of the tensile test specimens.

### 3.3.2. SOFMAN Components

Fourteen SOFMAN tensile test specimens, with the dimensions presented in Table 3-6, were tested.

Table 3-6: Dimensions of the SOFMAN tensile test specimens (dimensions in *mm*).

SOFMAN tensile test specimens	1EP355	2EP355	3EndP355	4EndP355	5IP355	6IP355	7ES355	8ES355	9IS355	10IS355	11PIN235	12PIN235	13PIN235*	14PIN235*
Height	180	180	180	180	180	180	180	180	180	180	180	180	180	107
Width	30	30	30	30	20	20	20	20	20	20	15	15	-	-
Thickness	10	10	10	10	10	10	10	10	10	10	15	15	-	-
Diameter	-	-	-	-	-	-	-	-	-	-	-	-	20	20

Note (\*): material of pin removed from untested device.

Since the pin material tensile test specimens did not exhibit a yielding plateau the method of 0.2% offset line was applied according to testing standards (ASTM A370-20, 2016), to define the yield strength. This method establishes the yield strength based on the intersection of the stress-strain curve of the material with an offset of 0.2% parallel line to the elastic range. A demonstration of the method is shown in Figure 3-13.

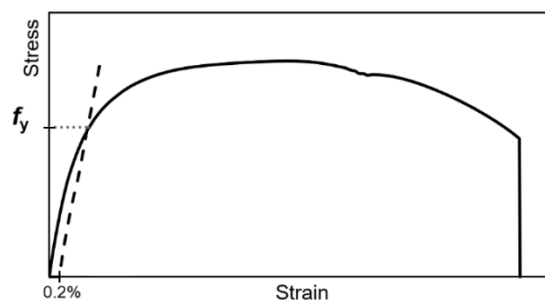


Figure 3-13: Determination of yield strength using 0.2% offset line method.

Average yield stress and tensile strength values obtained for each element is given in Table 3-7.

Table 3-7: SOFMAN specimen tensile test data.

Element	Exterior Plate		End Plate		Internal Plate		Exterior Spacer		Interior Spacer		Pin			
Codename	1EP355	2EP355	3EndP355	4EndP355	5IP355	6IP355	7ES355	8ES355	9IS355	10IS355	11PIN235	12PIN235	13PIN235*	14PIN235*
$f_y$ (MPa)	380	380	380	380	370	370	370	370	370	370	380	380	370	430
$f_u$ (MPa)	580	600	610	620	610	560	600	600	610	580	510	520	520	500

All elements presented an expected resistance except the pin material. Consulting the stress-strain curves for the pin elements presented in Annex A it can be observed that the material did not present a yielding plateau and most importantly, the stresses are higher than expected for a S235 steel grade material. This led to two additional tensile tests on the pin material to verify if the tensile test specimens of the pin material received presented the same characterizing properties as the material of the pin installed in the devices. This time the tensile test specimen was manufactured by removing one pin from an untested device (Figure 3-14). This material showed the same unwanted characteristics. Hence, pins with a new material, referred to as IST pin material, were manufactured.



Figure 3-14: Tensile test specimen 13: (a) removed pin and (b) pin processing.

**3.3.3. IST Components**

Due to the observations referred above, a new pin material, IST material, was manufactured and tested (Figure 3-15). The circular tensile test specimen used to characterize this material had the length of 165 mm and a diameter of 20 mm. The resulting characteristics for this material are presented in Table 3-8. Again, no yielding plateau was observed, but fortunately this material presents a lesser resistance. It still did not show the prescribed characteristics but for the purposes of the experimental tests it was considered adequate. This way, the material was considered to meet the prescribed designed material choices for the experimental tests.

Table 3-8: IST specimen tensile test data.

Element	Name	$f_y$ (MPa)	$f_u$ (MPa)
Pin	15PIN235	370	420



Figure 3-15: Tensile test specimen 15PIN235.

### 3.4. Experimental Setup

The experimental tests took place at LERM, IST (Figure 3-16), where the previous pin device design, INERD (Calado et al., 2004) was tested, in 2004. Fulfilling the demands of this study, in terms of facilities, equipment and experience of the team leading the experiment.



Figure 3-16: Experimental test setup at LERM.

The experimental test process consists of imposing uniaxial displacements, through a mechanical actuator, on a brace equipped with the dissipative device. These displacements are controlled manually through the control console and can be either in forward or backward directions, corresponding to compression or tension, respectively. An installed load cell then measures the force that the pin device is subjected.

The fixed equipment composing the laboratory setup are presented in Figure 3-17.

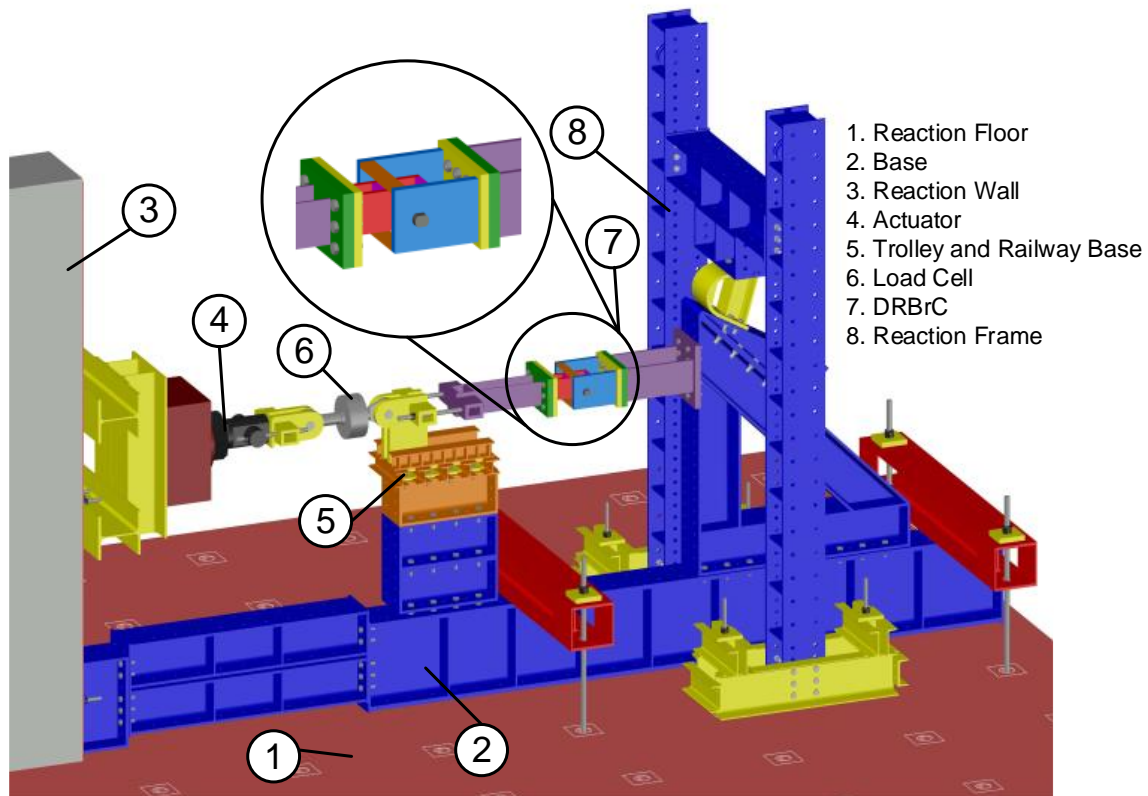


Figure 3-17: Fixed equipment scheme.

The instrumentation of the test (Figure 3-18) is composed of:

- Load Cell: This force transducer converts the force into an electrical signal. The electrical signal is measured and processed into a load measurement. It has a load range of  $1000\text{ kN}$ , ( $-500\text{ kN}$  to  $500\text{ kN}$ ).
- Linear Variable Differential Transformer 1 (LVDT1): Measures the longitudinal linear displacement of the system. Each LVDT is equipped with a mobile cursor which sends an electrical impulse when moved. The impulse is then transmitted to the data acquisition system and converted into a displacement measurement. Positioned horizontally under the pin device. It has a range of  $100\text{ mm}$  ( $-50\text{ mm}$  to  $50\text{ mm}$ ).
- Linear Variable Differential Transformer 2 (LVDT2): Measures the out-of-plane linear displacement. Positioned horizontally on the exterior face of an exterior eye-bar plate of the dissipative device,  $20\text{ mm}$  from the free end. It has a range of  $40\text{ mm}$  ( $-20\text{ mm}$  to  $20\text{ mm}$ ).
- Wire Transducer: As well as the LVDT1, it measures the longitudinal linear displacement of the system. Serves as a backup equipment so that, if LVDT1 fails at any point during the test, the displacement measurements can still be attained. This instrument is less accurate than the LVDTs.

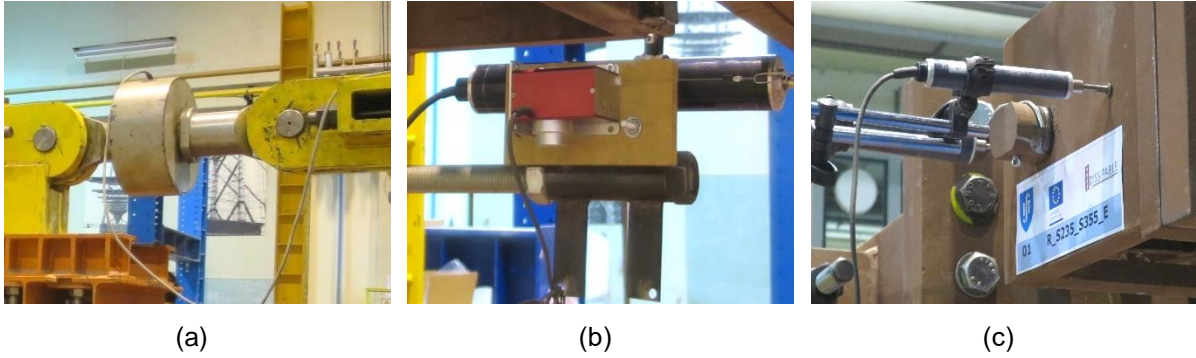


Figure 3-18: Instrumentation: (a) Load cell, (b) LVDT1 and wire sensor, (c) LVDT2.

For all instrumentation, including the load cell a positive and negative direction is defined. Positive force readings happen when the bracing element is under tension. Similarly, positive displacement values are given when the transducers are retracted, equivalent to the tensile direction of the bracing element. The transducers positioning as well as the direction criterion are illustrated in Figure 3-19.

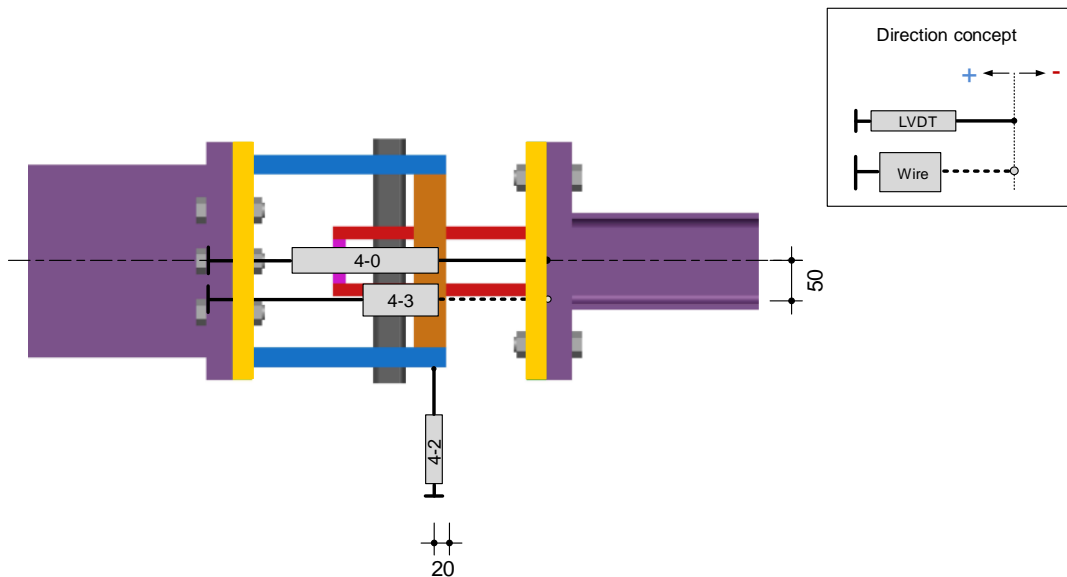


Figure 3-19: Instruments position and direction criterion.

To calibrate the instrumentation, control the movement of the actuator and data acquisition and processing the following equipment (Figure 3-20) is also required:

- Computer: equipped with the laboratory software, it allows for instrument calibration and organization as well as data storage and visualization.
- Control console: unit that controls the movement of the actuator.
- Data logger: unit of data acquisition.

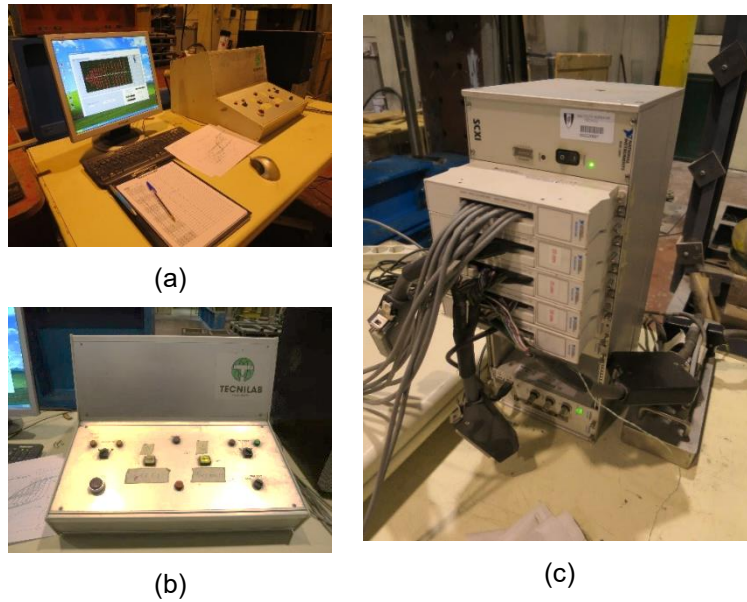


Figure 3-20: Examples of equipment used: (a) computer setup, (b) control console and (c) data logger.

The instrumentation was connected to a module of the data logger and organized in four information input channels in the laboratory software, as presented in Table 3-9.

Table 3-9: Measuring instruments configurations.

Channel	Instrument	Name	Codename	Sensibility	Scale
4-0	LVDT1	CDP-100	561656	5 mV/V	100
4-1	Load Cell	HBM 500	F846	2 mV/V	500
4-2	LVDT2	CDP-50	511662	5 mV/V	50
4-3	Wire Transducer	DP-500 E	BGD130526	5 mV/V	500

The minimum time between two successive readings the computer could register data is about 2 seconds.

A more detailed description of the assembly of the specimens and of the experimental test setup is described in further detail in the deliverable D4.1 Report on experimental tests on DRD systems (DISSIPABLE, 2020b).

Before initiating the tests following tasks are performed:

- Measurement of the geometric dimensions of the test specimen.
- Exact placement of all instrumentation.
- Video cameras positioning, a top view and a lateral view.
- All measuring instruments are confirmed to be functional, calibrated and organized in the Data Logger channels.

During the tests, all displacement and force readings had to be carefully observed, through the computer, since the process of imposing displacement was manual, and also because some instrumentation occasionally revealed reading errors leading to brief suspensions of the test to fix these incidences.



### 3.5. Experimental Results

For each experimental test, the following information is presented:

- Configuration scheme of the test specimen.
- Load history applied.
- Maximum force ( $kN$ ) in both tensile and compressive directions.
- Maximum longitudinal displacement ( $mm$ ) in both tensile and compressive directions.
- Total dissipated energy ( $kNm$ ), determined by the integral of the force-displacement curve.
- Total number of cycles.
- Pictures taken, during and after the tests, as visual representation of the occurrences.
- Hysteresis loop of the device response, in terms of the applied force ( $kN$ ) and imposed displacement ( $mm$ ).

The configuration codename is organized by the number of the test configuration, the pin section geometry, the prescribed pin steel grade, the prescribed plates steel grade and the load protocol applied (Figure 3-21).

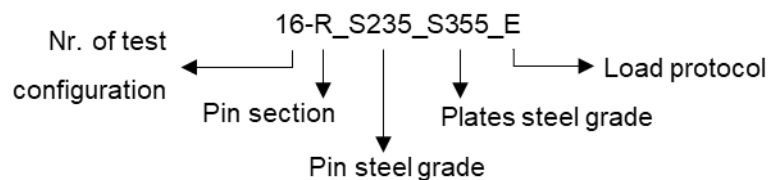


Figure 3-21: Codename for the experimental test configurations.

The experimental tests results will be presented chronologically ordered and not numerically as it is in the specimens list depicted in Table 3-10. This is because following the chronological order the process of discussion on the occurrences and improvements on each test is thought to be more evident.

Table 3-10: Tested specimens (adapted from DISSIPABLE, 2020c).

Test Configurations			Pin			Guiding Plates	
No	Codename	Acronym	Section	$\Phi$ ( $mm$ )	Material	GP1	GP2
01	R_S235_S355_E	<b>01R</b>	R	50	SOFMAN		
02	R_S235_S355_E	<b>02R</b>	R	50	IST	X	
03	R_S235_S355_C1	<b>03R</b>	R	50	IST	X	
04	R_S235_S355_C2	<b>04R</b>	R	50	IST	X	X
15	C_S235_S355_E	<b>15C</b>	C	50 W1	SOFMAN	X	
16	C_S235_S355_E	<b>16C</b>	C	50 W2	IST	X	X
17	C_S235_S355_E	<b>17C</b>	C	50 W1	IST	X	X
18	C_S235_S355_E	<b>18C</b>	C	50 W3	IST	X	X

### 3.5.1. Experimental Test 01R

The first experimental test, with codename 01-R\_S235\_S355\_E, is composed by a chamfered section pin device (Figure 3-22 a), with all materials manufactured by SOFMAN. No guiding plates are applied. The loading history applied is defined by a hysteretic cycle following the ECCS protocol (Figure 3-22 b).

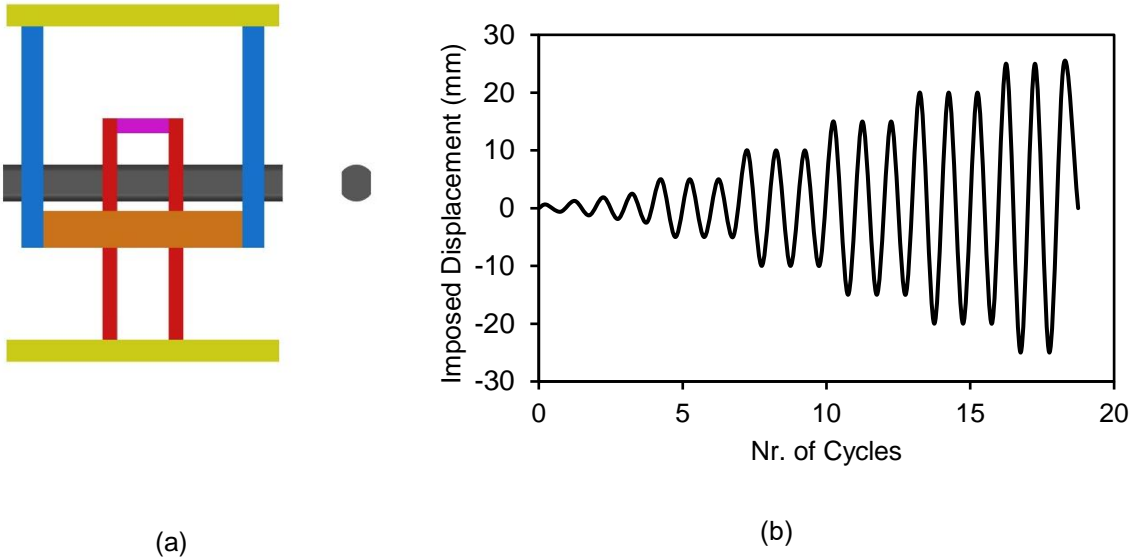


Figure 3-22: Experimental test 01R: (a) specimen model, (b) load history applied.

This test revealed unexpected high forces, and was interrupted at some point, before reaching pin failure because the pin was increasingly coming out of the longitudinal plane, due to the decentralization of the imposed displacement. Pronounced elongation, and ovalization of the holes of the eye-bar plates occurred. The positive and negative peak load and imposed displacement, total dissipated energy and number of cycles obtained in the experimental test 01R is presented in Table 3-11.

Table 3-11: Results for experimental test 01R.

	Positive	Negative
$F_{max}$ (kN)	505	-474
$\delta_{max}$ (mm)	25.94	-27.06
Dissipated Energy (kNm)	110	
Nr. of cycles	19	

Note: Did not reach failure



(a)



(b)



(c)



(d)

Figure 3-23: Experimental test 01R: (a) & (b) asymmetric loading, (c) pin elongation and (d) pin sliding.

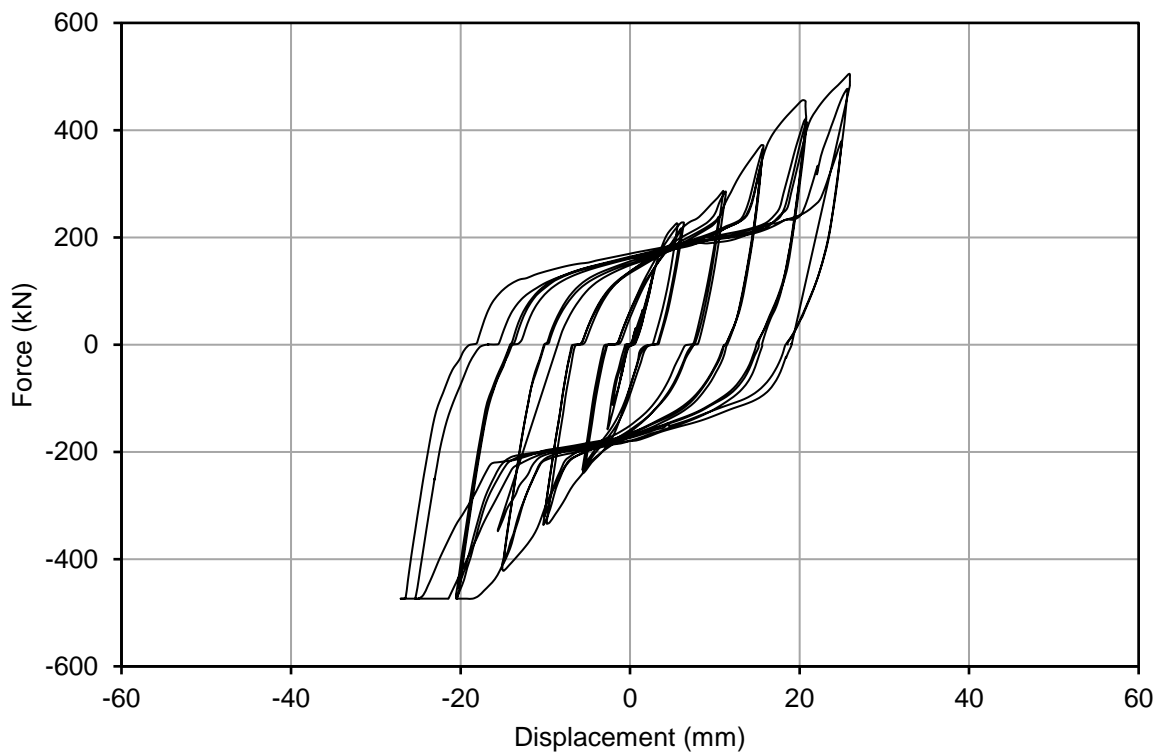


Figure 3-24: Force-displacement curve for experimental test 01R.

### 3.5.2. Experimental Test 15C

The test specimen 15-C\_S235\_S355\_E is composed by a circular section pin (Figure 3-25 a) and plate elements made of SOFMAN material. Following the results of the first experimental test, guiding plates GP1 are implemented to help centralize the imposed displacement. Contains weld configuration (W1). The loading history applied is defined by a hysteretic cycle following an adapted ECCS protocol (Figure 3-25 b).

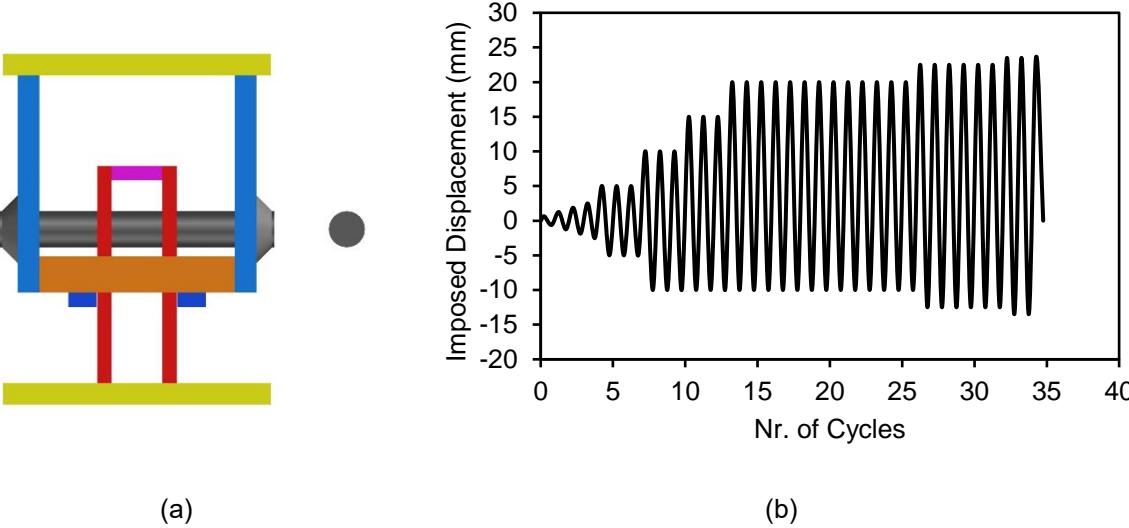


Figure 3-25: Experimental test 15C: (a) specimen model, (b) load history applied.

Just as the first experimental test, unexpected high forces took place. This led to the interruption of the test before reaching pin failure, however the welds did reach failure. The welded sections prevented the pin elongation. Ovalization of the holes of the eye-bar plates occurred. The positive and negative peak load and imposed displacement, total dissipated energy and number of cycles obtained in the experimental test 15C are presented in Table 3-12.

Table 3-12: Results for experimental test 15C.

	Positive	Negative
$F_{max}$ (kN)	527	-474
$\delta_{max}$ (mm)	23.85	-13.85
Dissipated Energy (kNm)	190	
Nr. of cycles	27	

Note: Did not reach pin failure, reached failure of the welds.



(a)



(b)



(c)



(d)

Figure 3-26: Experimental test 15C: (a) GP1 position, (b) weld failure, (c) asymmetric loading and (d) exterior plate ovalization.

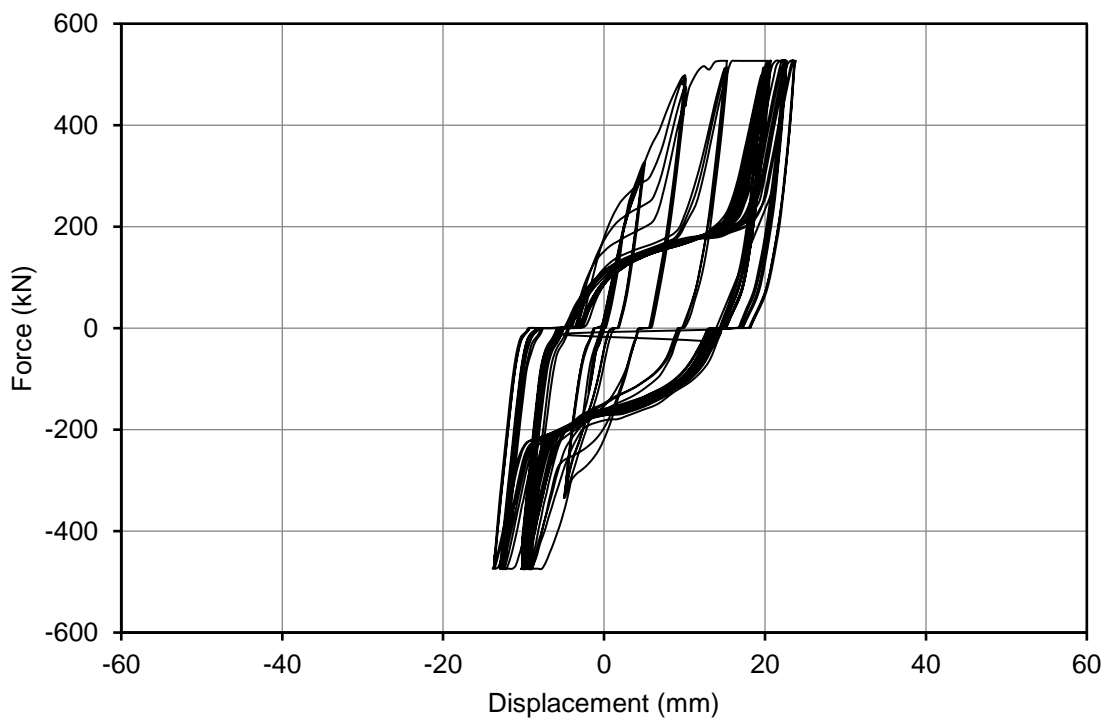


Figure 3-27: Force-displacement curve for experimental test 15C.

### 3.5.3. Experimental Test 02R

The test specimen 02-R\_S235\_S355\_E is composed by a chamfered section pin (Figure 3-28 a) with IST material, and plate elements with SOFMAN material. Contains guiding plates GP1.

The loading history applied consists of a hysteretic cycle following the ECSS protocol (Figure 3-28 b).

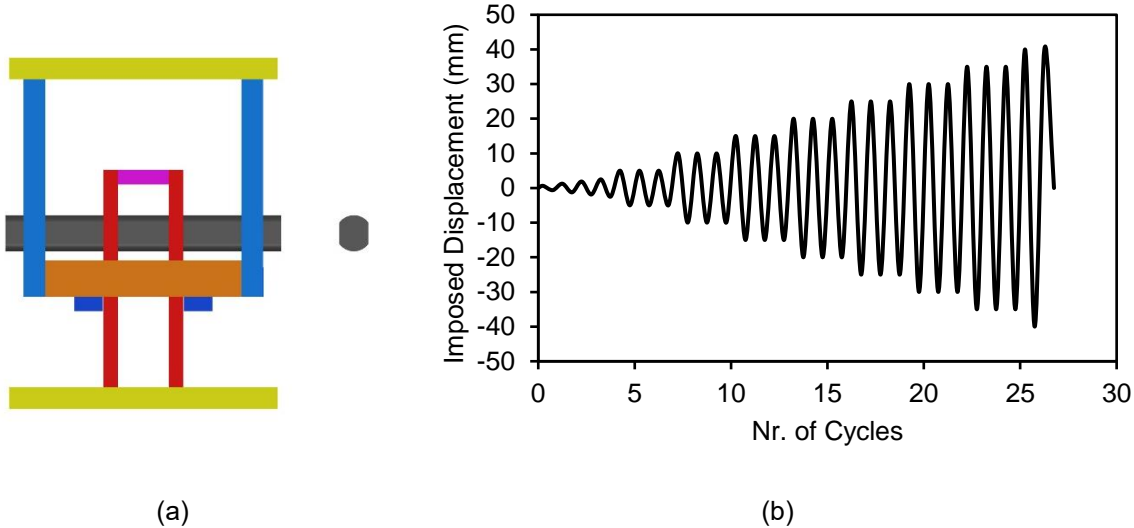


Figure 3-28: Experimental test 02R: (a) specimen model, (b) load history applied.

Pin failure occurred at the mid-span of the pin due to bending and tensile forces. Large plastic deformation and elongation of the pin. Quasi symmetric deformation of the pin. Ovalization of the holes of the eye-bar plates occurred. The positive and negative peak load and imposed displacement, total dissipated energy and number of cycles obtained in the experimental test 02R are presented in Table 3-13.

Table 3-13: Results for experimental test 02R.

	Positive	Negative
$F_{max}$ (kN)	488	-505
$\delta_{max}$ (mm)	40.31	-40.61
Dissipated Energy (kNm)	200	
Nr. of cycles	29	

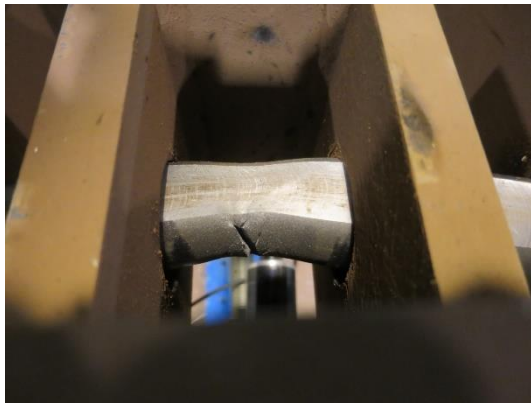
Note: Reached pin failure.



(a)



(b)



(c)



(d)

Figure 3-29: Experimental test 02R: (a) pin deformation, (b) pin elongation, (c) & (d) pin failure.

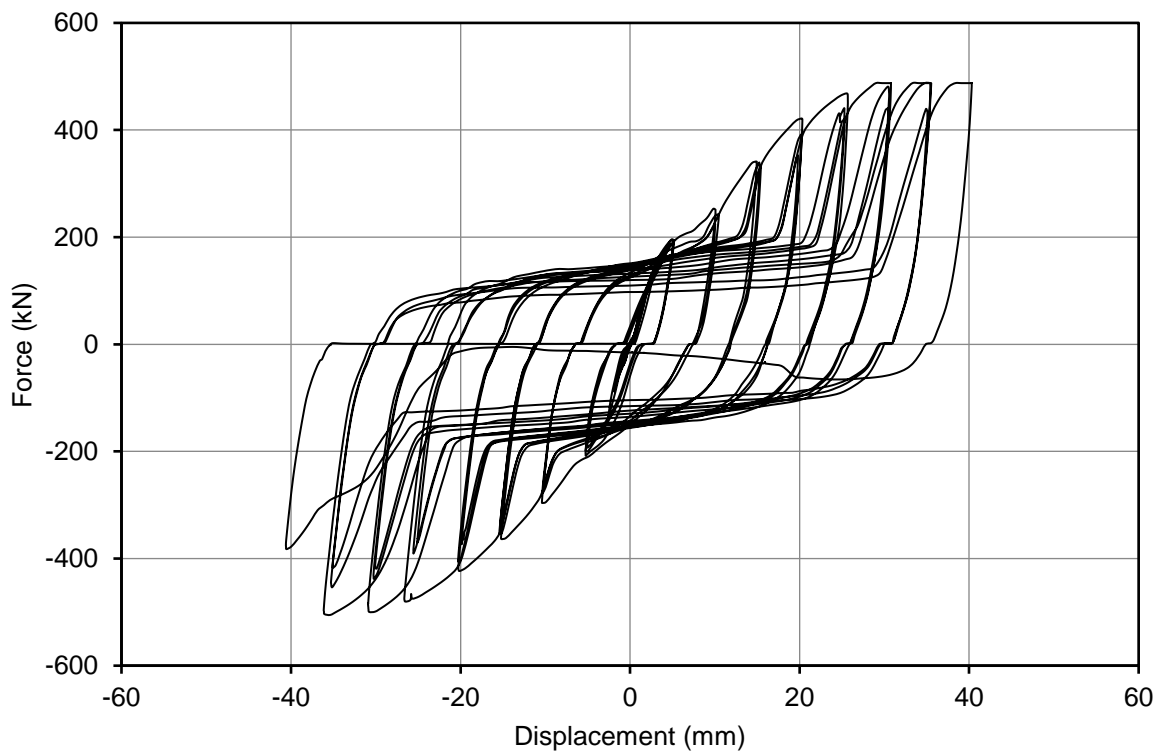


Figure 3-30: Force-displacement curve for experimental test 02R.

**3.5.4. Experimental Test 03R**

The test specimen 03-R\_S235\_S355\_C1 is composed by a chamfered section pin (Figure 3-31 a) with IST material and plate elements with SOFMAN material. Contains guiding plates GP1.

The loading history applied consists of a hysteretic cycle following an adapted constant pattern (Figure 3-31 b).

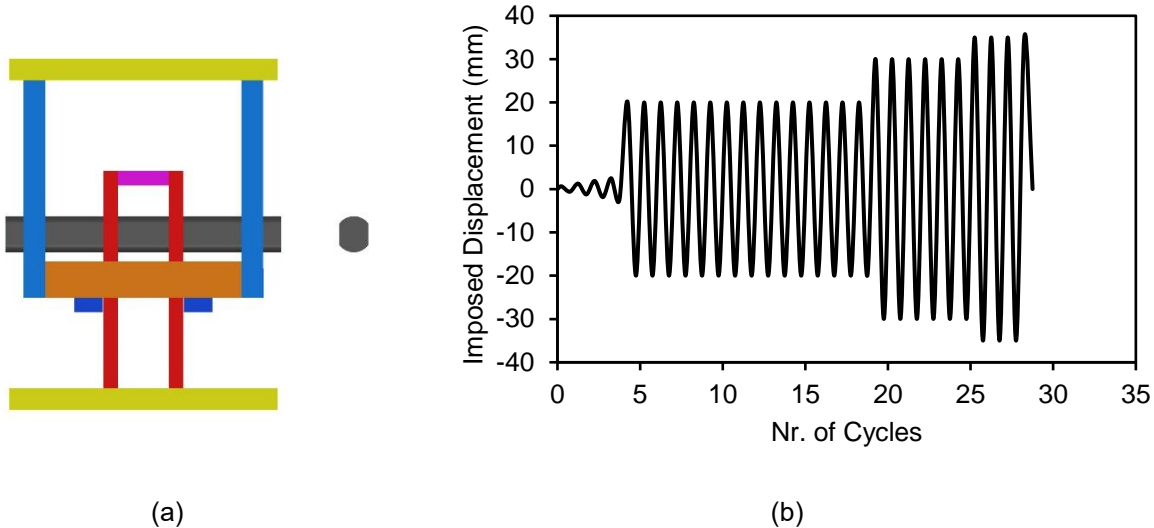


Figure 3-31: Experimental test 03R: (a) specimen model, (b) load history applied.

Like the previous test, the pin failure occurred at mid-span of the pin due to bending and tensile forces. Large plastic deformation and elongation of the pin. Quasi symmetric deformation of the pin. Ovalization of the holes of the eye-bar plates occurred. The positive and negative peak load and imposed displacement, total dissipated energy and number of cycles obtained in the experimental test 03R are presented in Table 3-14.

Table 3-14: Results for experimental test 03R.

	Positive	Negative
$F_{max}$ (kN)	488	-513
$\delta_{max}$ (mm)	36.46	-35.20
Dissipated Energy (kNm)	208	
Nr. of cycles	23	

Note: Reached pin failure.





(a)



(b)



(c)



(d)

Figure 3-32: Experimental test 03R: (a) asymmetric loading, (b) pin elongation, (c) & (d) pin failure.

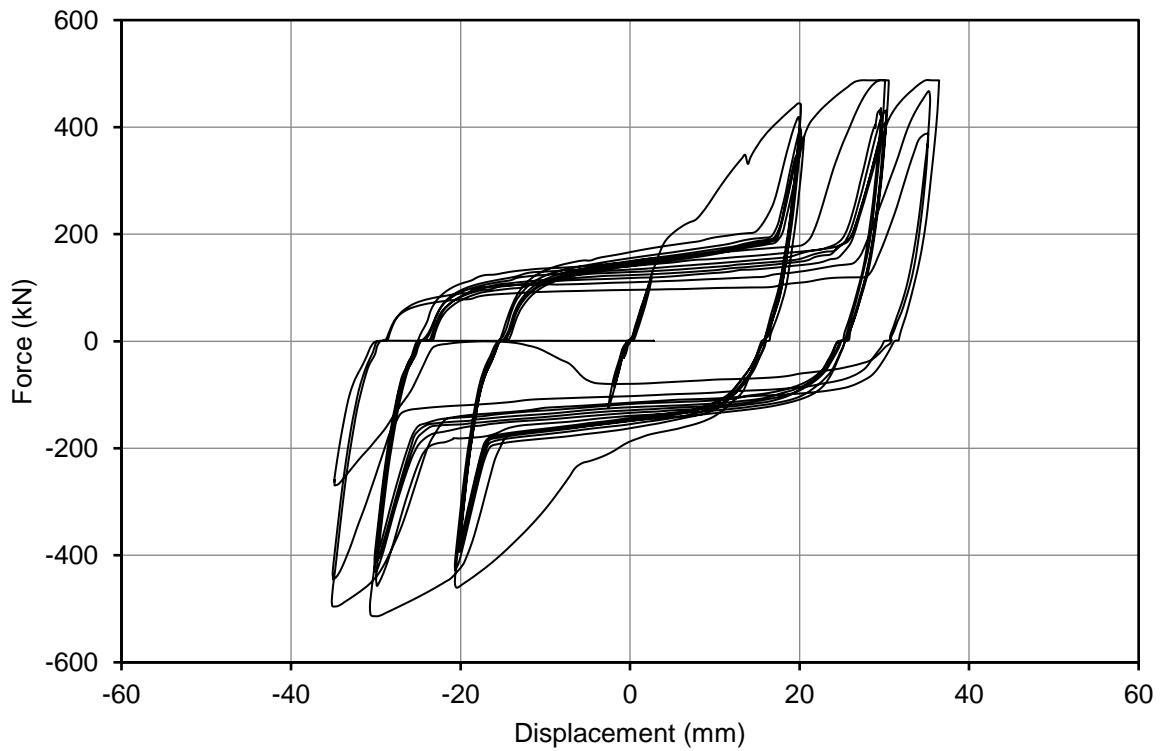


Figure 3-33: Force-displacement curve for experimental test 03R.

### 3.5.5. Experimental Test 04R

The test specimen 04-R\_S235\_S355\_C2 is composed by a chamfered section pin (Figure 3-34 a) with IST material and plate elements with SOFMAN material. Contains guiding plates GP1 and it is the first test to have the inclusion of the second group of guiding plates GP2.

The loading history applied consists of a hysteretic cycle following a constant pattern (Figure 3-34 b).

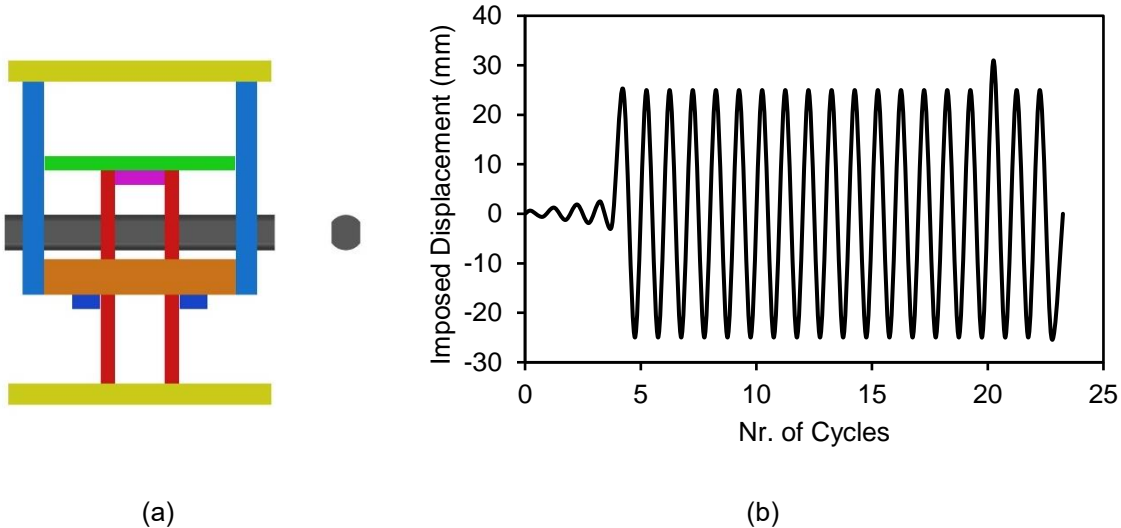


Figure 3-34: Experimental test 04R: (a) specimen model, (b) load history applied.

The pin failure occurred at mid-span of the pin due to bending and tensile forces. Large plastic deformation and elongation of the pin. Symmetric deformation of the pin and diminished lateral displacements due to the employment of both guiding plates groups. Ovalization of the holes of the eye-bar plates occurred. The positive and negative peak load and imposed displacement, total dissipated energy and number of cycles obtained in the experimental test 04R are presented in Table 3-15.

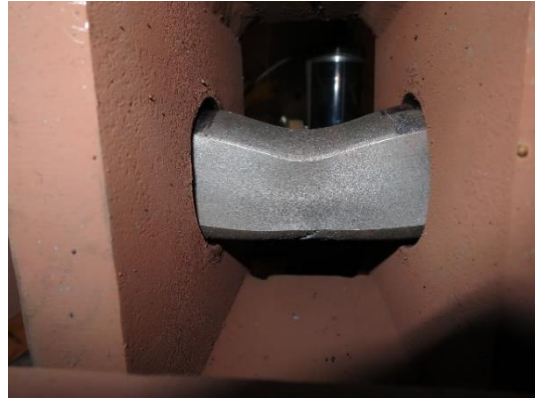
Table 3-15: Results for experimental test 04R.

	Positive	Negative
$F_{max}$ (kN)	486	-487
$\delta_{max}$ (mm)	32.62	-25.51
Dissipated Energy (kNm)	190	
Nr. of cycles	35	

Note: Reached pin failure.



(a)



(b)



(c)



(d)

Figure 3-35: Experimental test 04R: (a) pin elongation, (b) pin deformation, (c) & (d) pin failure.

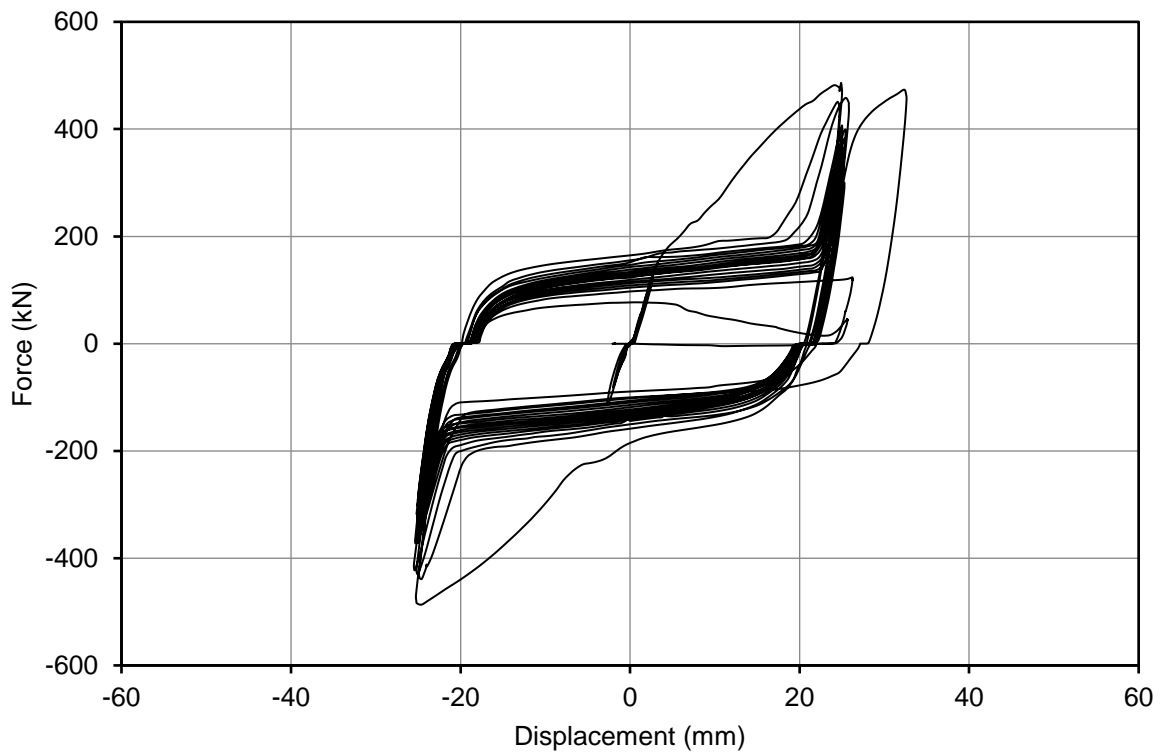


Figure 3-36: Force-displacement curve for experimental test 04R.

**3.5.6. Experimental Test 16C**

The test specimen 16-R\_S235\_S355\_E is composed by a circular section pin (Figure 3-37 a) with IST material and plate elements with SOFMAN material. Contains guiding plates GP1 and GP2 guiding plates and W2 weld configuration.

The loading history applied consists of a hysteretic cycle following an adapted ECCS protocol (Figure 3-37 b).

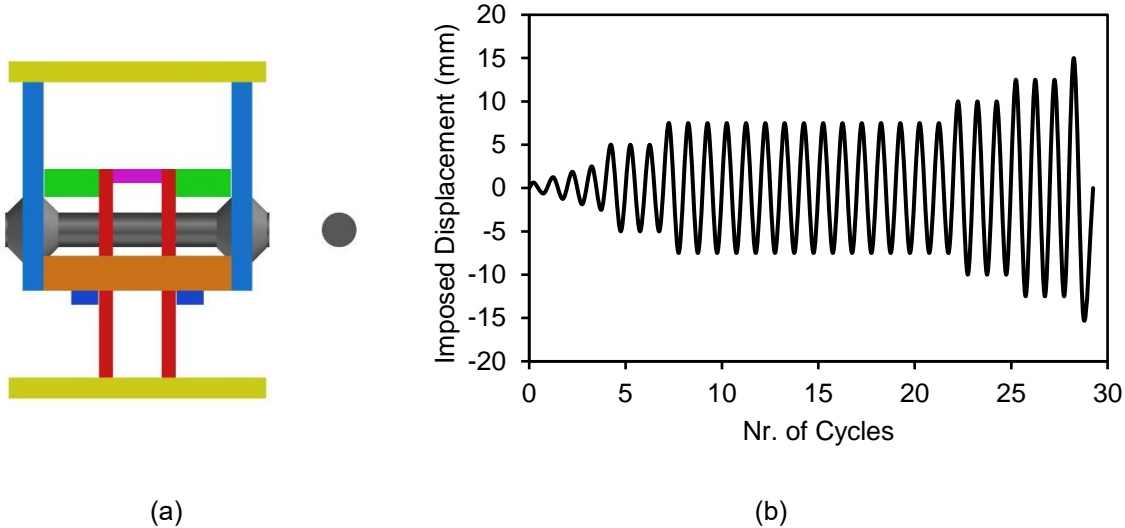


Figure 3-37: Experimental test 16C: (a) specimen model, (b) load history applied.

This four-section welded specimen revealed diminished pin elongation and deformation. The pin reached failure near the welded sections, due to high shear forces mobilized. The welds did not reach failure. The positive and negative peak load and imposed displacement, total dissipated energy and number of cycles obtained in the experimental test 16C are presented in Table 3-16.

Table 3-16: Results for experimental test 16C.

	Positive	Negative
$F_{max}$ (kN)	488	-513
$\delta_{max}$ (mm)	15.01	-15.72
Dissipated Energy (kNm)	97	
Nr. of cycles	29	

Note: Reached pin failure, did not reach welds failure.



(a)



(b)



(c)



(d)

Figure 3-38: Experimental test 16C: (a) onset of failure of the pin, (b) failure mode (c) & (d) pin failure.

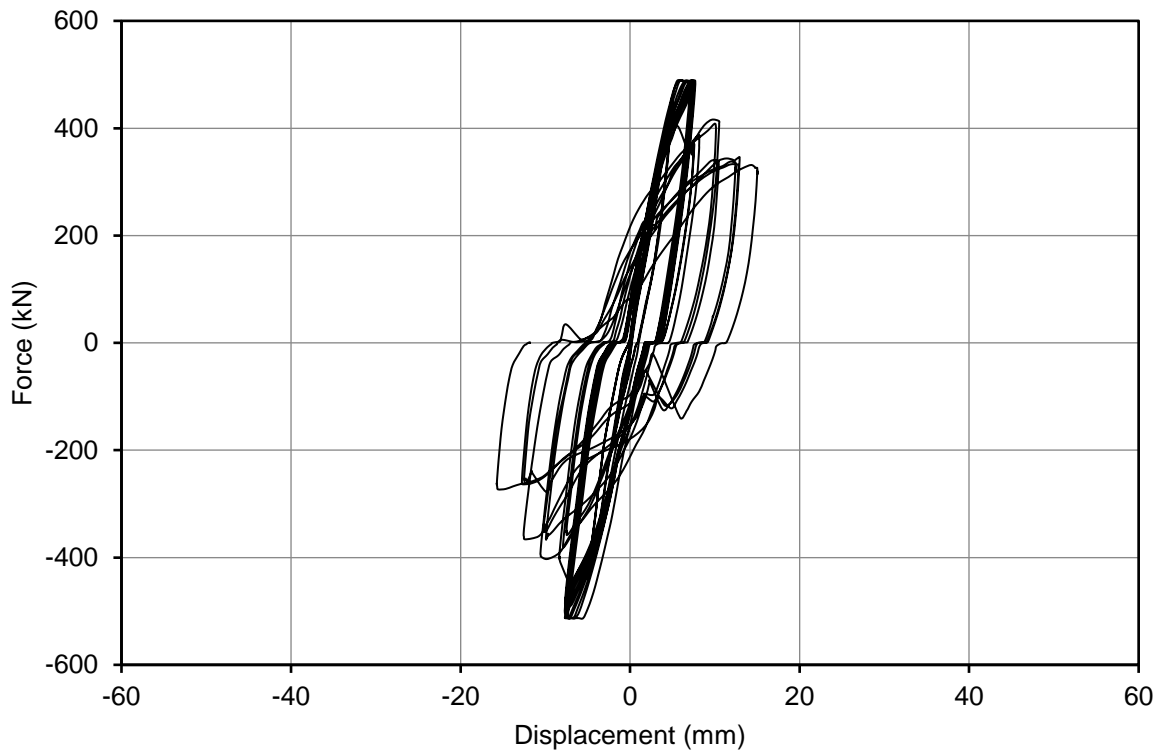


Figure 3-39: Force-displacement curve for experimental test 16C.

### 3.5.7. Experimental Test 17C

The test specimen 17-C\_S235\_S355\_E is composed by a circular section pin (Figure 3-40 a) with IST material and plate elements with SOFMAN material. Contains guiding plates GP1 and GP2 guiding plates and W1 weld configuration.

The loading history applied consists of a hysteretic cycle following an adapted ECCS protocol (Figure 3-40 b).

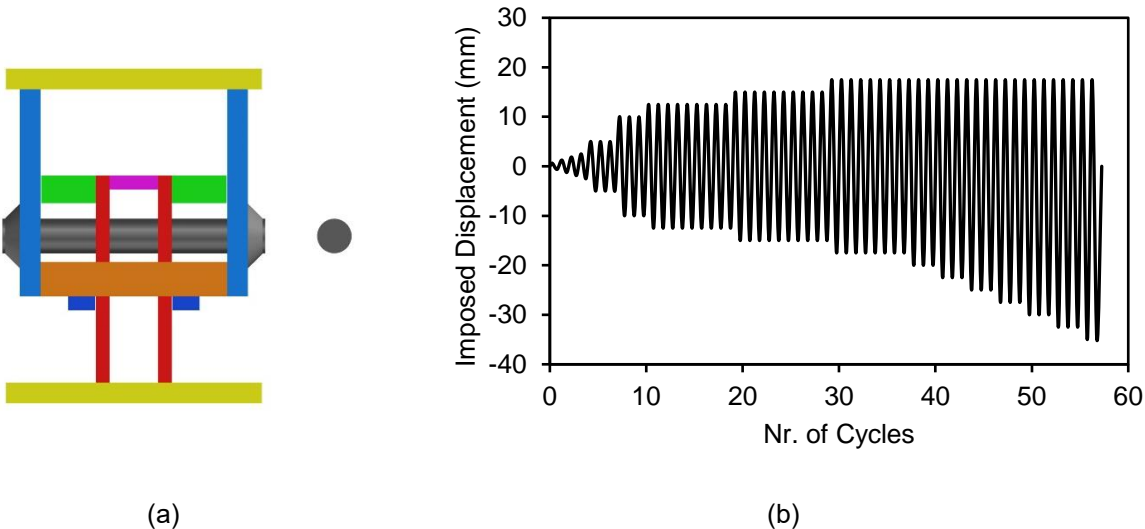


Figure 3-40: Experimental test 17C: (a) specimen model, (b) load history applied.

The two welded sections prevented pin elongation and deformation, as it is observed in the experimental test 16C. It resulted in early failure of the welds. The pin was in an advanced damaged state near the welded sections but did not reach full failure because the test had to be terminated for technical reasons related to the operation of the actuator. The positive and negative peak load and imposed displacement, total dissipated energy and number of cycles obtained in the experimental test 17C are presented in Table 3-17.

Table 3-17: Results for experimental test 17C.

	Positive	Negative
$F_{max}$ (kN)	487	-514
$\delta_{max}$ (mm)	18.08	-35.13
Dissipated Energy (kNm)	452	
Nr. of cycles	57	

Note: Pin did fracture but did not reach full failure, it reached welds failure.

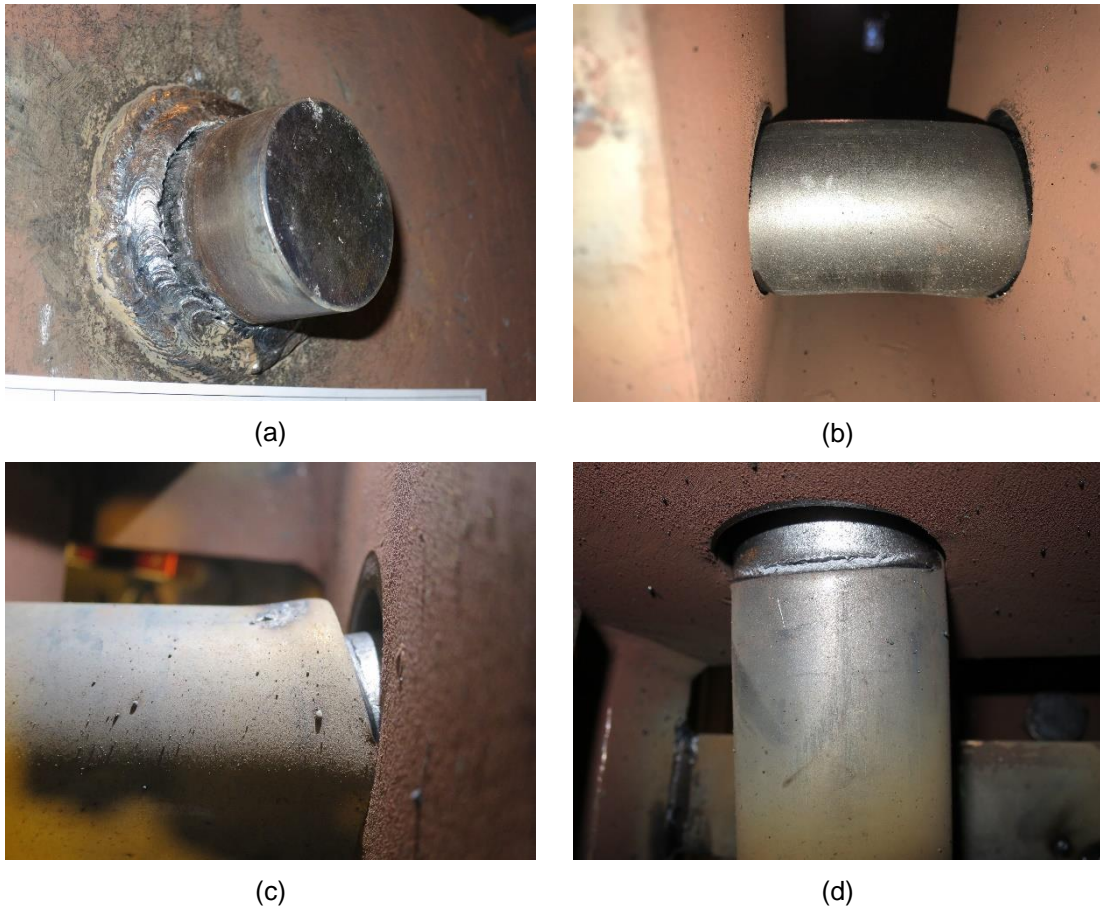


Figure 3-41: Experimental test 17C: (a) weld failure, (b) mid-span undeformed section, (c) & (d) pin failure.

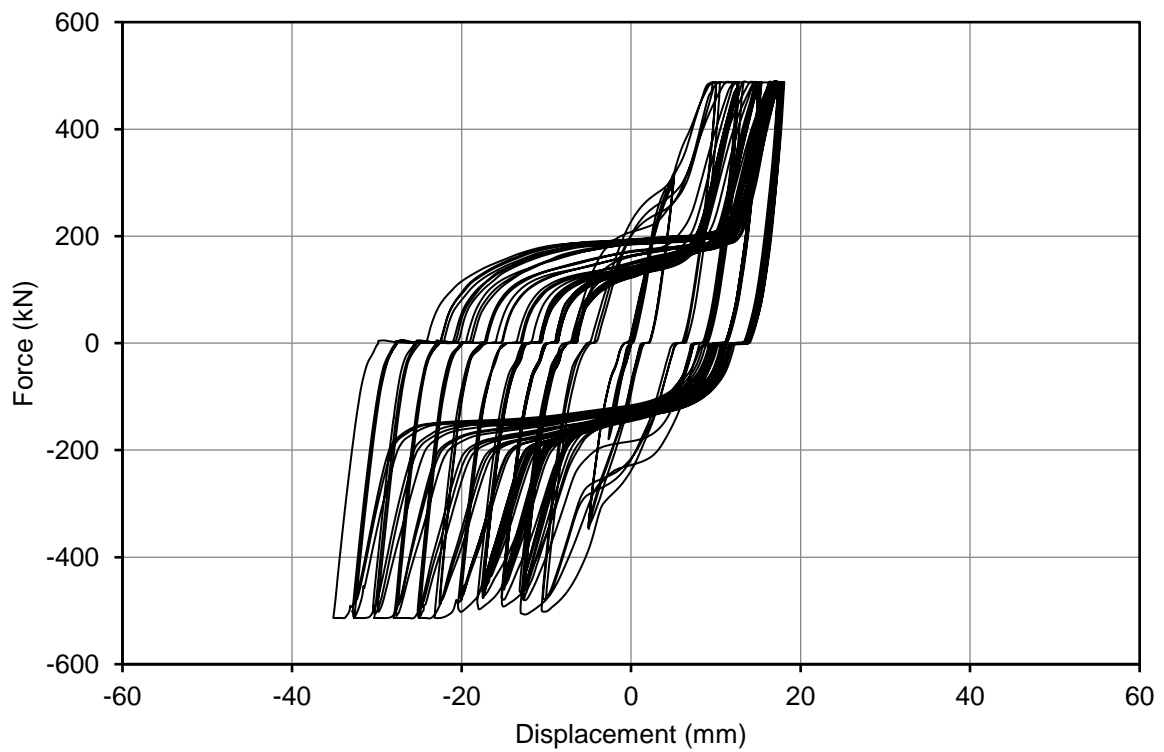


Figure 3-42: Force-displacement curve for experimental test 17C.

### 3.5.8. Experimental Test 18C

The test specimen 18-C\_S235\_S355\_E is composed by a circular section pin (Figure 3-43 a)) with IST material for the pin and plate elements with SOFMAN material. Contains guiding plates GP1 and GP2 guiding plates and W3 weld configuration.

The loading history applied consists of a hysteretic cycle following an adapted ECCS protocol (Figure 3-43 b)).

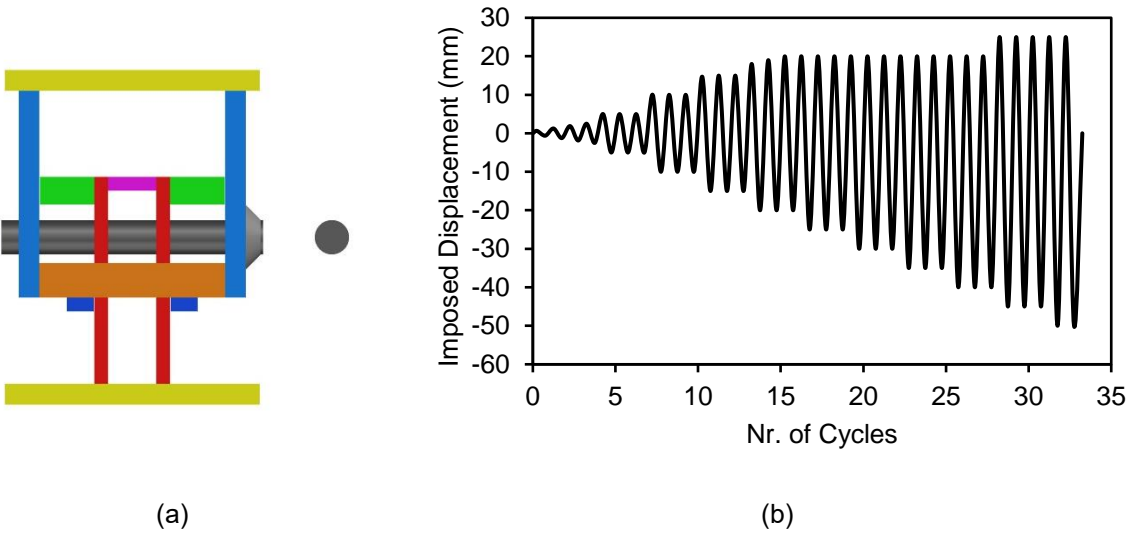


Figure 3-43: Experimental test 18C: (a) specimen model, (b) load history applied.

With only one welded section, large pin elongation and deformation took place. It resulted in an early weld failure. The failure of the pin occurred near the welded section due to high shear forces mobilized. The positive and negative peak load and imposed displacement, total dissipated energy and number of cycles obtained in the experimental test 18C are presented in Table 3-18.

Table 3-18: Results for experimental test 18C.

	Positive	Negative
$F_{max}$ (kN)	487	-514
$\delta_{max}$ (mm)	27.86	-52.45
Dissipated Energy (kNm)	340	
Nr. of cycles	33	

Note: Reached pin and welds failure.



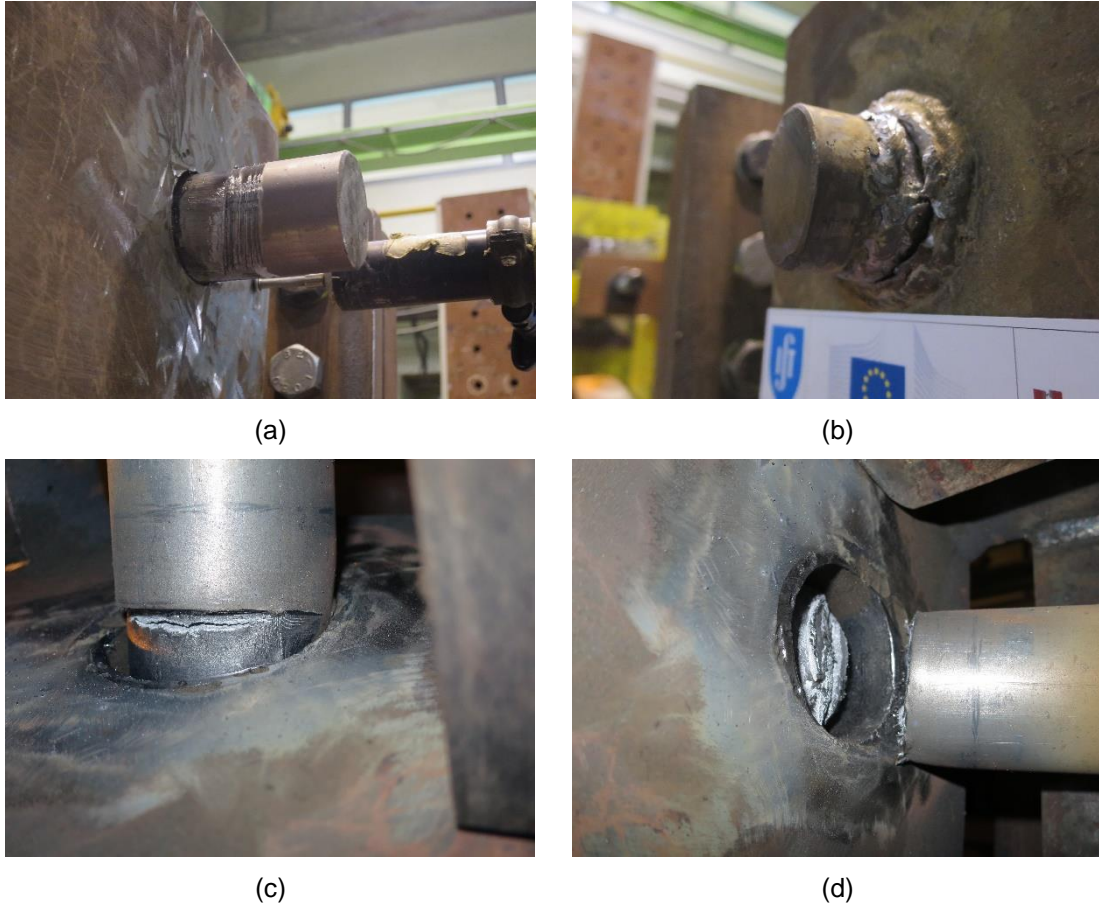


Figure 3-44: Experimental test 18C: (a) pin elongation, (b) weld failure, (c) & (d) pin failure.

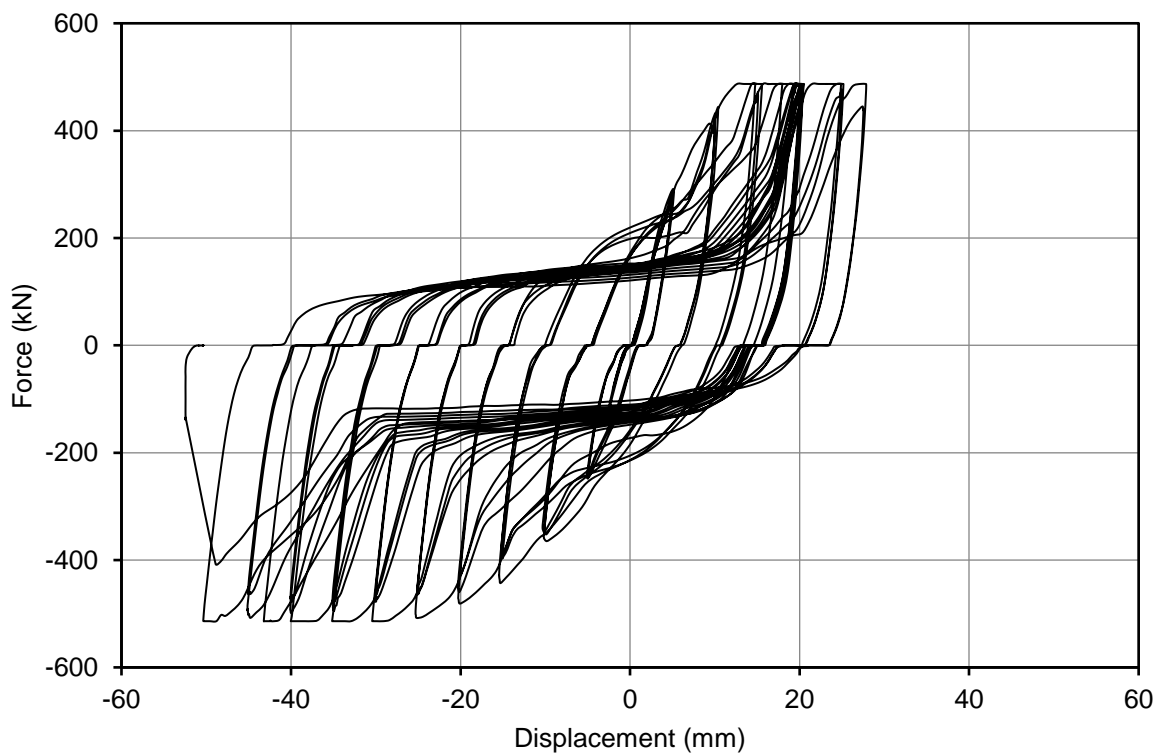


Figure 3-45: Force-displacement curve for experimental test 18C.

### 3.6. Conclusions

A general evaluation of the influence that each variable revealed in the performance of the tested configurations is discussed in this section. As referred in the literature review, INERD studies presented a pinching phenomenon (Vayas et al., 2017), due to the ovalization of the eye-bar plate holes. This issue was also verified in the experimental results obtained for the DRBrC connection. On a positive note, the transverse bending of the steel plates observed in INERD, was negligible in the DRBrC connection due to the inclusion of the spacers.

In the first instance, regarding the pin section geometry, all chamfered sections presented a failure mode due to bending, in the mid-section of the pin, as it is ideal. On the other hand, the circular section configurations with weld configurations presented a failure mode due to shear, in the contact of the exterior eye-bar plates, which is more abrupt at its occurrence. This probably happens because since the chamfered pin can elongate freely out-of-plane, the section reduction is focused on the mid-span of the pin, where the bending is higher. Leading to the development of the local plastic hinge at this point, and consequently to the failure through accumulation of plasticity. On the other hand, since the circular sections configurations have welds preventing the pin from elongating, the section is barely reduced when compared to the chamfered configurations and happens to be more fragile in the areas of contact of the eye-bar plates. One experimental test worth of attention to support this argument is the 18C where, since only one extremity is welded, the pin elongates on the other side. Exhibiting a much more ductile behaviour, identical to the chamfered section configurations. It is possible to conclude that using welds is not favorable to the pin device performance, not only because the welds present a premature brittle failure but also because they prevent the pin elongation, compromising the ductile behaviour of the pin as well as the failure mode. By analyzing the failure modes, it is possible to conclude that the elongation of the pin plays a fundamental role on the failure mode and cyclic behaviour of the specimens. The first test for each pin section geometry, namely, the 01R and 15C were performed with the original pin material, produced by SOFMAN. This material revealed high resistance. Ultimately, the pins with SOFMAN material did not reach failure, simply because the material was too resistant for the purposes of the experimental studies. On the contrary, all the pins with IST material reached failure.

Constant amplitude was only applied once in experimental test 04R. All load histories are slightly different for each test, introducing comparison limitations. However, it is also a favorable thing, to evaluate and analyze the behaviour of the pin under a varied range of imposed displacements.

Regarding the circular pin configurations with welded sections, the most favorable weld position was when there was only one section weld. The pin had a more ductile behaviour because it could elongate. All the other weld configurations made the pin stiffer, resulting in shear failure modes.

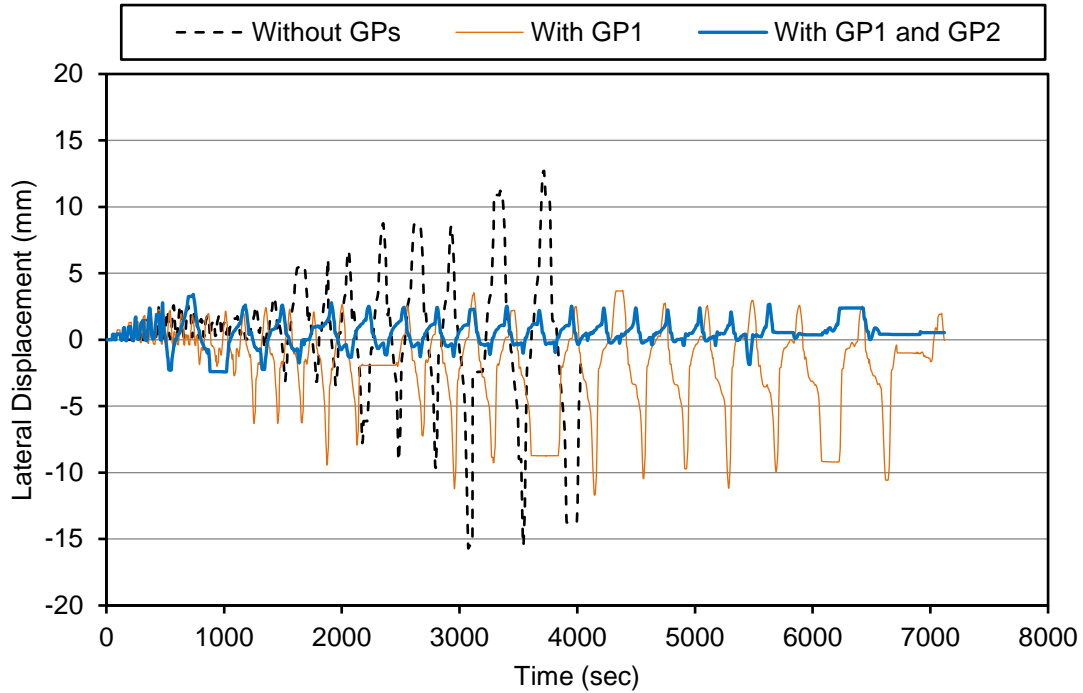


Figure 3-46: Guiding plates influence on lateral displacement.

Figure 3-46 shows the influence of the guiding plates on the lateral displacement of the external plates. It can be observed that when the GP1 is applied, positive displacements, that correspond to lateral displacements to the inside of the pin device box, are greatly reduced, but the negative displacements remained prevalent. It can be concluded that GP1 benefits the behaviour of the pin device because it prevents the movement of the exterior plates on this direction. But it is only when both guiding plates are applied that the improvements are clear, showing pronounced and symmetrical reduction on the lateral displacement of the exterior eye-bar plates. The best results were obtained when both groups of guiding plates, GP1 and GP2 were applied considering that the maximum lateral displacements were reduced from 15 mm to 3 mm, a reduction of more than 500%. The inclusion of both guiding plates brings very significant advantages to the pin performance because they permit for efficient centralization of the movement of the device. Avoiding buckling and non-axial loads or displacements formation. With these results guiding plates revealed to be an indispensable upgrade to apply on future designs. Although the application of these elements dictates an increased cost of the dissipative device, its benefits on the performance remarkably surpass that drawback. Additionally, although increasing the total weight of the system, it has shown not to influence the easiness of installation and reparability.

Table 3-19: Dissipated energy and nr. of cycles obtained in each experimental test.

Test Nr.	01R	02R	03R	04R	15C	16C	17C	18C
Dissipated Energy (kNm)	110	200	<b>208</b>	190	224	97	<b>452</b>	340
Nr of Cycles	19	29	23	<b>35</b>	27	29	<b>57</b>	33

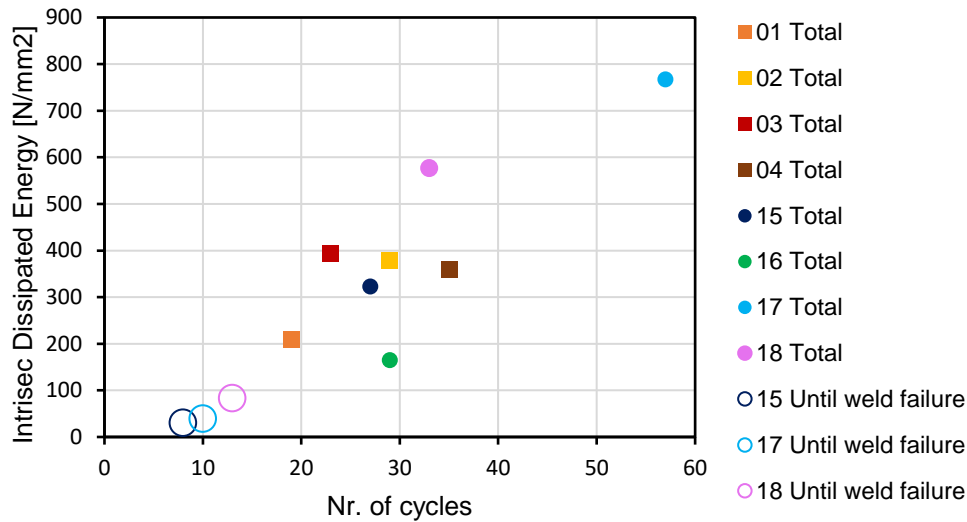


Figure 3-47: Guiding plates influence on lateral displacement.

The values of total energy dissipated are presented in Table 3-19. Additionally, Figure 3-47 shows the total intrinsic dissipated energy at the end of the tests. In the case of the circular pin test configurations, it is also presented the dissipated energy at the cycle where failure of the welds took place, except for test 16C where the pin did reach failure, but the welds did not. Total intrinsic dissipated energy is used in order to have uniform values and it is determined by the ratio between total dissipated area and dissipative volume. The dissipative volume is the volume of the pin regarding the length between the middle axis of the exterior plates.

This way, it is possible to verify that the circular pin tests with welds present a greater dispersion of values, indicating a very unpredictable behaviour, despite having obtained the test with the highest number of cycles and dissipation energy. Whereas the tests with chamfered pin present energy dissipation values under a close range

As noted earlier, the failure modes of the circular pin specimens presented a brittle behaviour early in the tests, which EC8 does not allow for dissipative zones. Additionally, regarding the circular pin configurations, the dissipated energy obtained until the failure of the welds is much lower than the obtained for the chamfered pin tests.

A more in-depth analysis on the performance of the tested pin devices is presented in the next chapter.

## 4. Analysis of Experimental Results

### 4.1. Experimental test limitations

A particular limitation that affected the experimental studies and the following analysis was the equipment used. Specifically, the load cell whose maximum capacity was easily reached on some experimental tests due to the high resistance of the pin, when following the formerly defined ECCS protocol. This issue occurred mainly in the case of the circular pin section tests. This led to occasional measurement failures and loss of information. As a result, some experimental force-displacement curves present a slight trimmed shape which represents missing dissipated energy, as it is illustrated in Figure 4-1. This issue was soon verified during the experimental test procedure. To avoid this, some load histories were adapted, during the experimental tests, as it was referred previously in section 3.1.7, so that the maximum load cell capacity would not be surpassed.

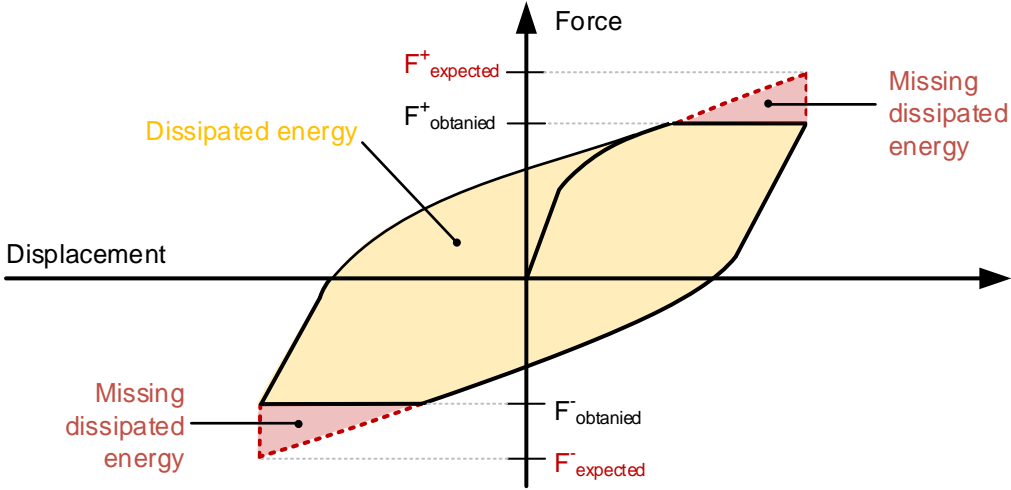


Figure 4-1: Equipment limitation: trimmed force-displacement curve.

The pin materials received had to be replaced due to their high resistance, as it is explained in section 3.3. Because of this, the two first experimental tests have SOFMAN pin material, and the remaining experimental tests have IST pin material. This led to comparison difficulties between the performance of the different tests. Additionally, the tests with SOFMAN pin material, 01R and 15C, did not reach failure. Even so, the manufacture of the new pins with IST material as well as their assembly resulted in a delay of the experimental tests process.

Despite the diversity of loading stories that, circumstantially, were forced to adopt, it was decided to proceed with the treatment of the results in the dimensionless way proposed by the ECCS (ECCS, 1986).

### 4.2. Parameters of interpretation

To compare the results between the different configurations, it was necessary to adopt a method that is able to homogenize the results. In this work, the method recommended by ECCS was applied, which is exactly intended for experimental cyclic tests on steel elements (ECCS, 1986).

Foremost, the elastic parameters for each configuration of the dissipative device tested experimentally were determined. In the case of cyclic tests, there will always be, for each parameter, two components, the positive that corresponds, in this work, to tensile actions in the bracing and the negative, corresponding to compressive actions in the brace. Therefore, each experimental test has a positive yield load,  $F_y^+$ , and a negative yield load  $F_y^-$ , with correspondent positive yield displacement,  $e_y^+$ , and negative yield displacement,  $e_y^-$ . According to the ECCS, the determination of these parameters is based on monotonic tests. However, in this work, since monotonic tests were not performed on the device specimens, these parameters were determined based on the envelope curve of each experimental cyclic test, as depicted in Figure 4-2. Thus, the limit of the elastic phase was determined through the intersection between the tangent of the envelope at the origin, whose slope defines the elastic stiffness  $K_e = tg\alpha_y^+$ , and the tangent of envelope with the slope of  $0.1 \cdot K_e$ . Thus, the elastic parameters obtained for each tested configuration is presented in Table 4-1.

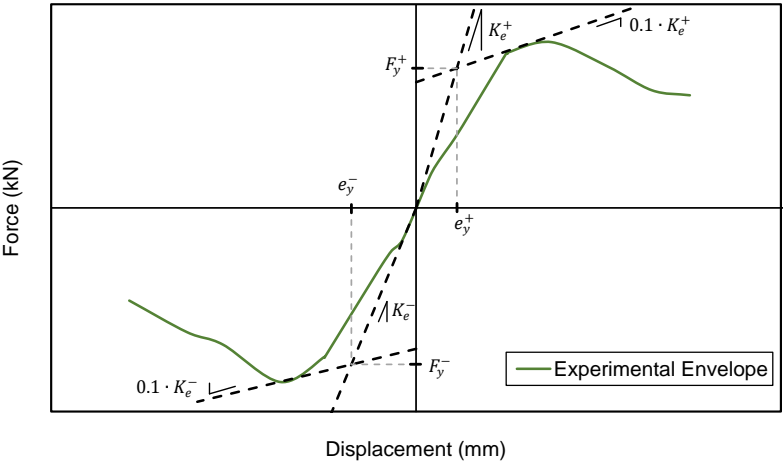


Figure 4-2: Determination of the elastic parameters.

Table 4-1: Elastic parameters of the tested devices.

	01R	02R	03R	04R	15C	16C	17C	18C
$F_y^+ (kN)$	433	344	378	400	464	411	456	444
$F_y^- (kN)$	-389	-378	-400	-411	-456	-461	-476	-422
$e_y^+ (mm)$	9.09	5.61	7.56	7.79	5.66	2.23	5.69	7.41
$e_y^- (mm)$	-6.48	-7.26	-8.00	-9.14	-6.90	-3.55	-6.79	-8.44

Subsequently, the characterizing parameters can be determined from the force-displacement curve, for each cycle, in the plastic range,  $e > e_y$ , as depicted in Figure 4-3. The absolute value of these parameters will be taken into account to determine said characterization parameters that relate the real behaviour obtained in the experimental tests with the perfect elastic-plastic behaviour (EPP) of the dissipative device. The expressions of the characterization parameters are presented in the following sections, along with the results and discussion.

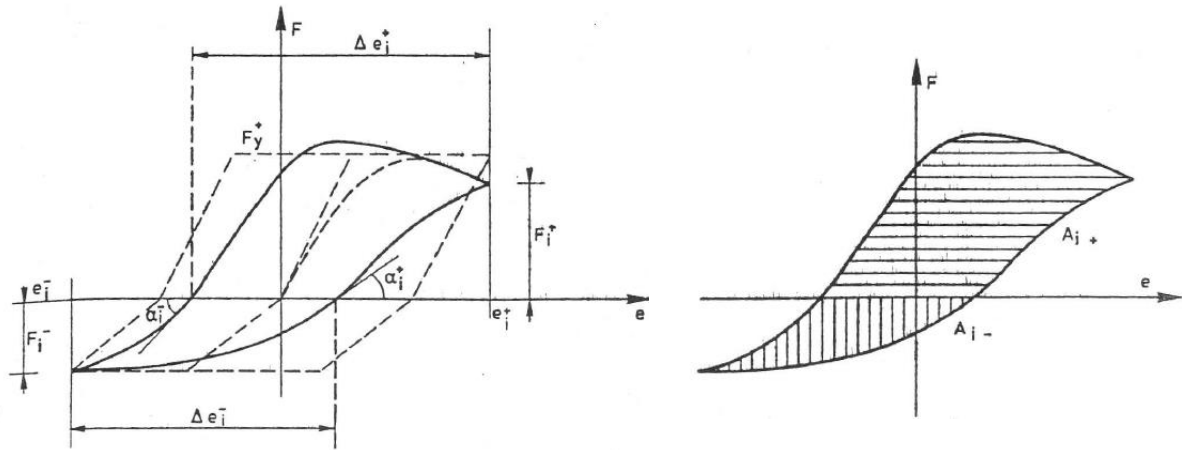


Figure 4-3: Parameters of interpretation for one cycle (ECCS, 1986).

### 4.3. Behaviour assessment of the experimental test configurations

As a tool to access the behaviour of the different experimental test configurations, the figures that represent each determined characterization parameter are presented separately for the chamfered pin section and circular pin section configurations. Additionally, although the characterizing parameters have an absolute value, the negative components, correspondent to the compressive actions in the brace are presented in the range of negative coordinates of the figures. Thus, enabling the assessment of the symmetrical behaviour of the pin device. Thereby, a generic comparison of the performance of each device configuration regarding the influence of the different variables considered was performed.

#### 4.3.1. Ductility

Ductility is defined as the ability of a material to deform plastically before failure. To evaluate ductility ECCS introduces various characterization parameters. In this study, ductility evaluation is performed using the full ductility parameter that represents the ratio between the excursion and the yield displacement and can be determined with the following expressions applied at the end of each cycle:

$$\mu_i^+ = \frac{\Delta e_i^+}{e_y^+} \quad (4.1)$$

$$\mu_i^- = \frac{\Delta e_i^-}{e_y^-} \quad (4.2)$$

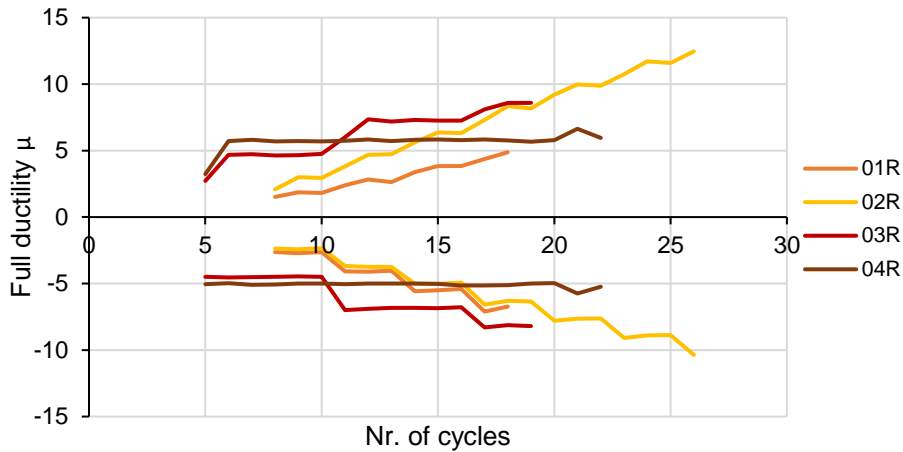


Figure 4-4: Full ductility of chamfered pin tests.

Examining Figure 4-4, where the full ductility for each half cycle of the chamfered pin tests, the test 04R progression remains approximately horizontal because it consists of a constant cyclic load history. It is visible for test 01R a discrepancy in the different directions of the load, so that test 01R shows greater ductility in the compressive directions. The test that presented general less ductility is the test 01R that contains SOFMAN pin material. The test with less ductility range is the test 04R. The test with highest ductility range is the 02R and the one with general higher ductility values are the 03R and 04R tests.

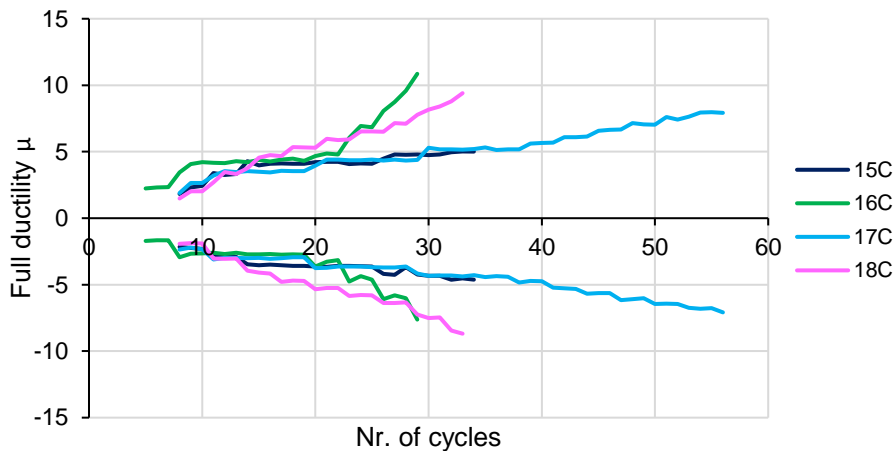


Figure 4-5: Full ductility of circular pin tests.

On the other hand, Figure 4-5 presents the full ductility for each half cycle of the circular pin tests. One can conclude that the ductile ability is practically symmetrical for all circular pin tests. The tests 16C and 18C present a higher ductility range, while 15C and 17C do not, even for a great number of cycles in the case of test 17C. It is interesting to note that both 15C and 18C have the same welded configurations and present similar low ductility ranges, although having different pin materials. This can mean that the welded configurations are more determining of the ductile ability of the pin device than the resistance of the pin material. Moreover, almost all configurations present symmetrical values.



It can be seen that in circular section configurations full ductility is generally lower. This is justified by the fact that circular tests require greater displacements imposed to adequately explore the inelastic properties. As an exception, test 18C showed higher values, justified by only having a welded section that enabled the pin to develop a more pronounced deformation.

**4.3.2. Stiffness**

Stiffness is the ability to distribute a load and resist deformation or deflection. It is related with the plastic hardening and stiffness degradation of the material. To evaluate stiffness, the rigidity ratio,  $\xi$ , proposed by ECCS is used. This characterizing parameter is defined by the ratio between the slope at the change of sign in the force and the elastic stiffness of the structural element:

$$\xi_i^+ = \frac{tg\alpha_i^+}{K_e^+} \tag{4.3}$$

$$\xi_i^- = \frac{tg\alpha_i^-}{K_e^-} \tag{4.4}$$

The Figure 4-6 shows the rigidity ratio at the end of each half cycle for the chamfered pin tests. All tests with the exception of test 01R, with SOFMAN pin material, present a decreasing rigidity ratio.

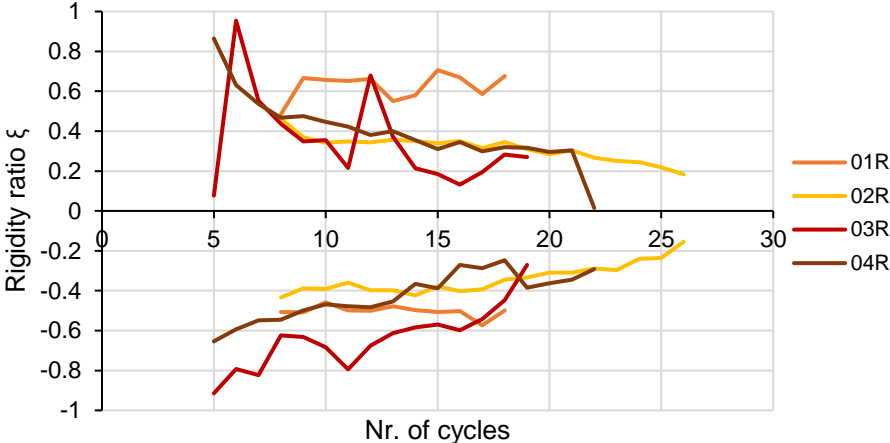


Figure 4-6: Rigidity ratio for chamfered pin tests.

The Figure 4-7 shows the rigidity ratio at the end of each half cycle for the circular pin test. The test with general higher rigidity ratios is the test 18C, again the one performing better from the group of circular pin tests, this can be justified because, although suffering a higher deformation, the deformation enabled the pin device to better distribute the loads and so presenting a higher rigidity ratio.

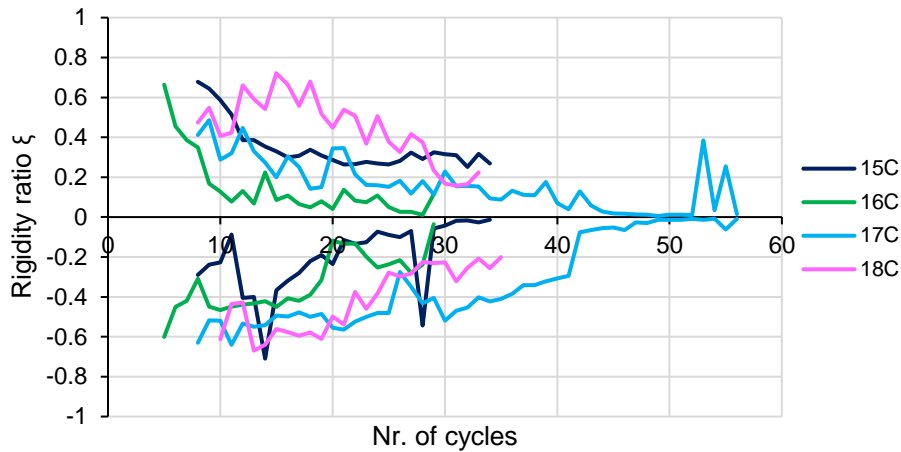


Figure 4-7: Rigidity ratio for circular pin tests.

The chamfered pin tests present a smoother variation while the circular pin sections have a sharper variation. This can be justified by the fixing mechanism opted for each configuration, since the chamfered sections are fixed geometrically the smooth rigidity decreasing happens at the rate of the ovalization of the plates and deformation of the pin. While the circular sections rigidity is affected by the welded sections that presented sudden failures, affecting all the system, and resulting in an irregular rigidity loss.

### 4.3.3. Resistance

Resistance is the general ability of a material to withstand an applied force. The parameter used to evaluate the resistance is the resistance ratio,  $\varepsilon$ , that can be determined with the following expressions:

$$\varepsilon_i^+ = \frac{F_i^+}{F_y^+} \quad (4.5)$$

$$\varepsilon_i^- = \frac{F_i^-}{F_y^-} \quad (4.6)$$

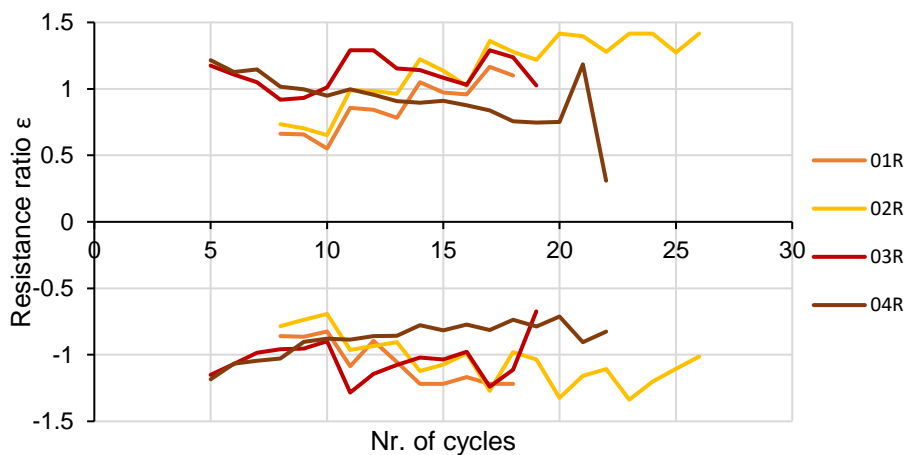


Figure 4-8: Resistance ratio for chamfered pin tests.

The Figure 4-8 shows the resistance ratio at the end of each cycle for chamfered pin tests. As referred earlier, the load history for the experimental test 04R is based on a constant amplitude of imposed displacements, thus it can be observed that the range of the resistance ratio obtained for this test is very limited. Test 01R and 02R show a clear crescent resistance ratio progress, where the last resistance ratio is superior to the first plastic range cycle. Otherwise, for test 03R and test 04R the resistance ratio decreased from the first to the last cycle.

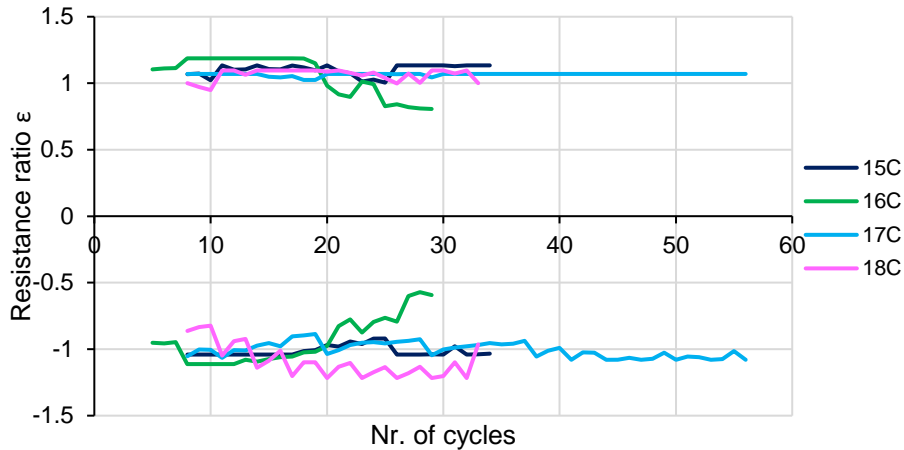


Figure 4-9: Resistance ratio for circular pin tests.

In the case of circular welded sections, the resistance ratio for each half cycle is shown in Figure 4-9, which have a generally low range of values. The test 17C presents a practically horizontal line in the positive direction due to the equipment limitation referred in section 4.1. Generally, all circular pin tests presented very horizontal and limited range of resistance ratios. This is because they have a generally higher resistance comparing to the chamfered sections, which was really close to the measuring capacity of the load cell. The few things that can be noticed is the degrading of resistance of test 16C, before completing 10 cycles, due to the welds failure, and the crescent resistance ratio on test 18C that stands out at the tensile direction, meaning that the test has a broader plasticity range. The positive and negative yield loads determined for the different specimens are generally close to the maximum load cell capacity, which explain the low range of the resistance ratios determined.

#### 4.3.4. Energy Dissipation

Energy dissipation is a measure of toughness, defined as the ability of a material to absorb energy and plastically deform without fracturing. This is an essential characteristic on dissipative devices. In order to evaluate the energy dissipation capacity, ECCS proposes the absorbed energy ratio that can be determined by the expressions:

$$\eta_i^+ = \frac{W_i^+}{F_y^+ \cdot (e_i^+ - e_y^+ + e_i^- - e_y^-)} \quad (4.7)$$

$$\eta_i^- = \frac{W_i^-}{F_y^- \cdot (e_i^+ - e_y^+ + e_i^- - e_y^-)} \quad (4.8)$$

Where the numerator represents the absorbed energy for every half cycle, determined by the integral of each half cycle of the force-displacement curve:

$$W_i^+ = A_i^+ = \int_{\text{cycle } i} F \cdot de, \quad F > 0 \tag{4.9}$$

$$W_i^- = A_i^- = \int_{\text{cycle } i} F \cdot de, \quad F < 0 \tag{4.10}$$

Accordingly, the total dissipated energy for each experimental test, value previously presented in the experimental results section 3.5, can be determined applying the expression:

$$W_t = \sum_{i=1}^{n \text{ cycles}} W_i \tag{4.11}$$

The cumulative dissipated energy for each experimental test is presented in Figure 4-10. The final value of each line represents the total energy dissipated energy. The test 17C had the highest dissipated energy with the highest number of cycles also performed, while the test 16C is the one with less dissipated energy. In the case of the chamfered sections test 02R showed the highest energy dissipated value, while test 03R is the one with less dissipated energy, also performing the lesser number of cycles. It can be observed that the weld configurations have an influence in the progress of the dissipated energy because the tests with two welded sections, 15C and 17C, show a very close progression. While test 17C with only one welded section presents a higher slope, that means that the dissipated energy per cycle is higher. The test 16C, with four welded section, has the lowest slope with the lowest dissipated energy per cycle. It is not possible to take conclusions on the different pin material tested because the SOFMAN pin configurations did not reach failure, but it can be seen that the influence in the progression is insignificant because test 15C and test 17C, and test 01R and 02R, with the same configurations and similar conditions only differing in the pin material, show a very close progression. It can also be noted that the chamfered sections show very similar progressions and limits, while the circular sections show pronounced diversions in the progression and maximum values.

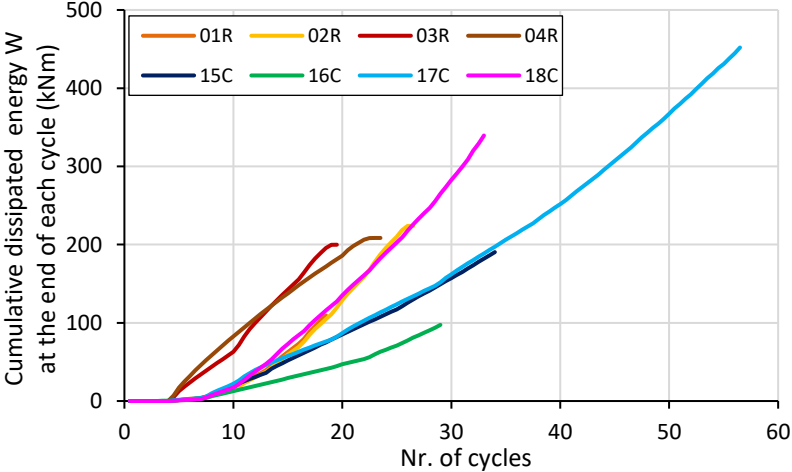


Figure 4-10: Cumulative dissipated energy  $W_T$  at the end of each cycle.

The absorbed energy ratio for each half cycle of the chamfered tests is presented in Figure 4-11. It can be seen that the energy dissipation capacity is progressively degraded with the running of the test. Every test shows a clear symmetrical behaviour. For the chamfered pin configurations, the test 01R shows the highest range of absorbed energy ratios, while test 03R and 04R presents a very limited range.

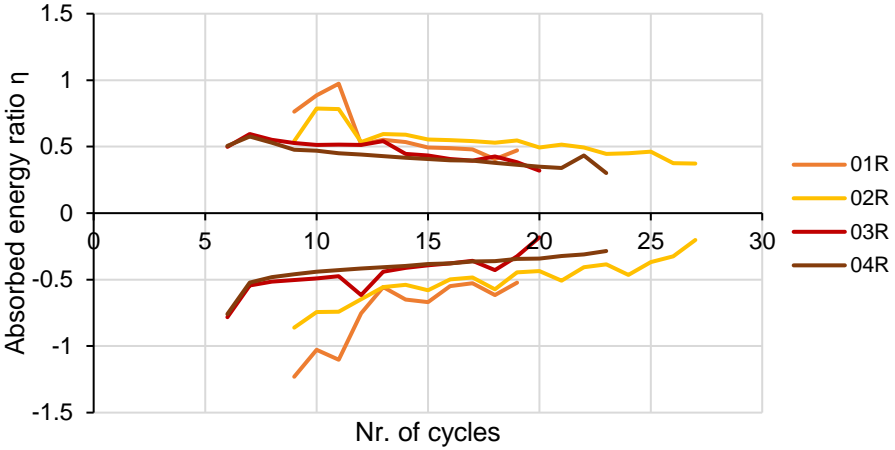


Figure 4-11: Absorbed energy ratio for chamfered tests.

The Figure 4-12 shows the absorbed energy ratio progression for circular tests. All tests present a decreasing absorbed energy ratio, with the exception of test 16C that practically stays in the same range of values. The test 18C shows a very step degradation on the energy dissipation capacity, probably due to the combined effect of the ovalization of the plates and the deformation of the pin.

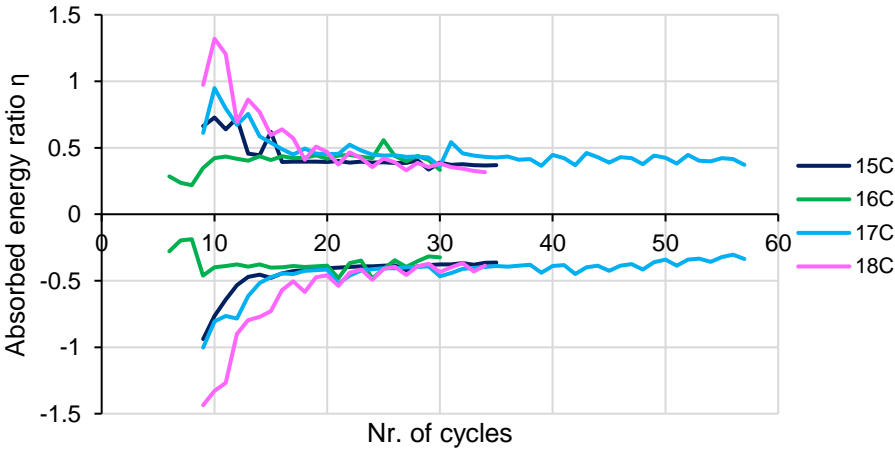


Figure 4-12: Absorbed energy ratio for circular tests.

From a cross over comparison of the last two figures, all the tests, regardless of the pin section and the material show a pronounced degradation, and in the case of the circular tests the absorbed energy ratio is stabilized after 20 cycles.



## **5. Numerical Models**

### **5.1. Introduction**

The development of the numerical models is explained in this chapter. Wherein, the applied concepts and calibration methods are presented. Furthermore, a general description of the relevant characteristics that define the numerical models is made, including the geometric properties, the material properties, and the type of analysis. The information obtained from the experimental tensile tests enabled the definition of the material properties. The results obtained from the numerical models are presented for both a chamfered pin test and a circular pin test.

### **5.2. Finite Element Model**

All the experimental tests, eight in total, were simulated using the general-purpose software ABAQUS/Standard. This software has Python embedded, which allowed the development of scripts to automate procedures of the modelling and the postprocessing. In this regard, three of the scripts developed and applied in this study are presented in Annex C. The different characteristics between the tested configurations such as pin material, pin section geometry, load histories and weld positions, in the case of circular sections, were all taken into consideration in the finite element models. The chamfered pin section tests have a completely symmetrical design in two planes, whereas the weld configurations applied in the circular pin are not always symmetrical. Therefore, the chamfered pin section tests were modelled taking advantage of the symmetry, while the circular pin section tests and the simulations present a complete model.

#### **5.2.1. Geometric properties**

Some geometric simplifications were assumed in the models so that all the dimensions for homonym elements in the different models are equal, that is, the diameter of the pin and the thickness of the plates, as well as the dimension of the hole tolerances are identical for all simulations.

#### **5.2.2. Material properties**

It is possible through the obtained stress-strain curves to define their corresponding constitutive relations and apply them on the numerical models. In terms of the defining properties of the materials discussed in this work we can divide it into two parts, the elastic behaviour and the plastic behaviour.

The elastic behaviour is considered to be isotropic and it is defined by the Young's modulus and Poisson's ratio. The conventional carbon steel elastic properties were assumed, namely the Young's modulus of 210GPa and Poisson's ratio of 0.3, following the Eurocode provisions (EN1993-1-1, 2005). In this study the steel materials involved can be classified as ductile materials given that they present large inelastic strains at orders of magnitude less than the Young's modulus. For this type of material, the input stress-strain values introduced in finite-element models must be the true stress and true strain (ABAQUS, 2012).

These values are slightly higher than the engineering stress-strain values obtained at the tensile tests described in the point 3.2.1, since they take into consideration the reduction of the section along the test

(Hradil et al., 2017). In this regard and according to Eurocode provisions (EN1993-1-5, 2006, p.45-49) the true stress,  $\sigma_{true}$ , and true strain,  $\varepsilon_{true}$ , values, presented in the Annex A, were determined using the following expressions:

$$\sigma_{true} = \sigma_{eng}(1 + \varepsilon_{eng}) \quad (5.1)$$

$$\varepsilon_{true} = \ln(1 + \varepsilon_{eng}) \quad (5.2)$$

These expressions are only valid in the plastic range until the ultimate tensile strength point, since, after this point, the stress and strain are not equally distributed in the cross-section anymore due to the effects of the necking phenomenon (Soboyejo, 2002).

The plastic hardening modelling for cyclic steel components is made considering the combined hardening theory present in ABAQUS, based on the formulations developed by Armstrong-Frederick and Chaboche (Myers et al., 2009 - Appendix D). As the term implies, it is defined by the combination of isotropic hardening with non-linear kinematic hardening (Figure 5-1). In the preliminary models the combined hardening parameters used were based on the literature (Krolo et al., 2016). Later, a calibration method was applied (Myers et al., - Appendix D).

The isotropic hardening component,  $\sigma^0$ , is defined by the instantaneous size of the yield surface derived from the following expression:

$$\sigma^0 = \sigma|_0 + Q_\infty(1 - e^{-b \cdot \bar{\varepsilon}^p}) \quad (5.3)$$

where,

$\sigma|_0$ : initial yield surface size (=  $f_y$ ).

$\bar{\varepsilon}^p$  : equivalent plastic strain.

$Q_\infty$  and  $b$ : isotropic hardening parameters.

Whereas the evolution of the non-linear kinematic hardening component is derived from the expression:

$$\bar{\alpha}_i = C \bar{\varepsilon}^p \frac{1}{\sigma^0} (\bar{\sigma} - \bar{\alpha}) - \gamma \bar{\alpha} \bar{\varepsilon}^p + \bar{\alpha}_{i-1} \quad (5.4)$$

where,

$\sigma^0$ : yield stress at zero plastic strain (=  $f_y$ ).

$C$  and  $\gamma$ : kinematic hardening parameters.

$\bar{\alpha}$ : equivalent back stress.

$\bar{\sigma}$ : equivalent stress or Von Mises stress.

Finally, the nonlinear combined isotropic and kinematic stress tensor, in the case of a tensile load test, is given by:

$$\bar{\sigma} = \sigma^0 + \bar{\alpha} \quad (5.6)$$



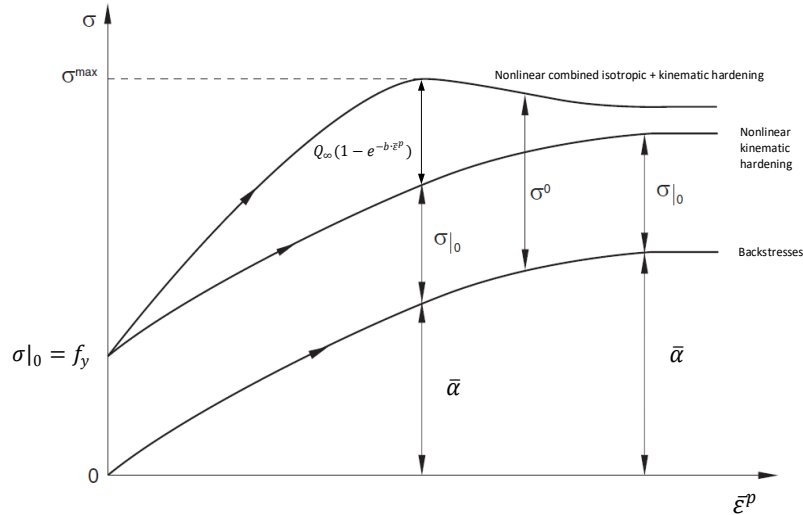


Figure 5-1: Evolution of isotropic and kinematic hardening for combined hardening model under uniaxial stress state (adapted from ABAQUS, 2012).

These parameters were derived preliminary in a curve fitting process, where the expressions, were applied analytically and faced with the true stress-strain curve obtained experimentally. Then, a simulation of the tensile tests was modelled, with the geometry, boundary conditions and mesh presented in Figure 5-2.

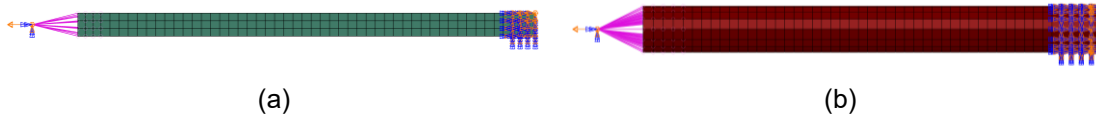
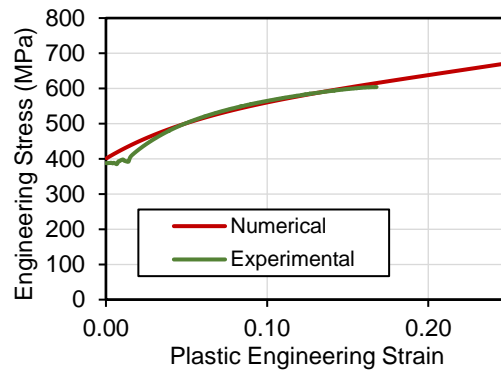


Figure 5-2: Boundary conditions and rupture: (a) plate element, (b) pin element.

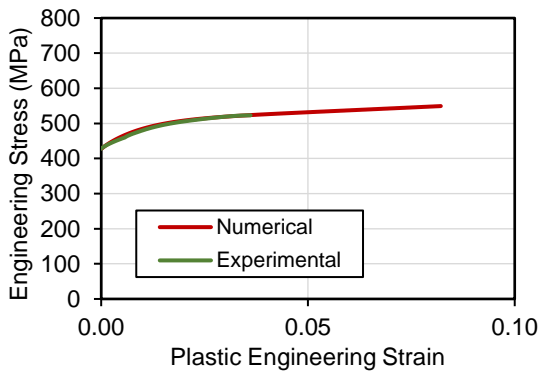
The results of the tensile tests models were compared to the ones obtained experimentally and through a process of a trial and error and curve fitting the combined hardening parameters were finally adjusted, resulting in the curves depicted in Figure 5-3. Ultimately, it was necessary to disregard the isotropic component because in order to calibrate both isotropic and kinematic aspects, cyclic tensile tests should have been performed, together with monotonic tensile tests. Since only monotonic tensile tests were performed experimentally it was only possible to consider one of these components. Thus, isotropic hardening was not taken into consideration because it does not capture the Bauschinger effect, where a hardening in tension will lead to a softening in a subsequent compression, whereas kinematic hardening does (Kelly, 2013). This way, the calibrated combined hardening parameters for each component of the pin device that were used in the numerical models are presented in Table 5-1.

Table 5-1: Combined hardening parameters.

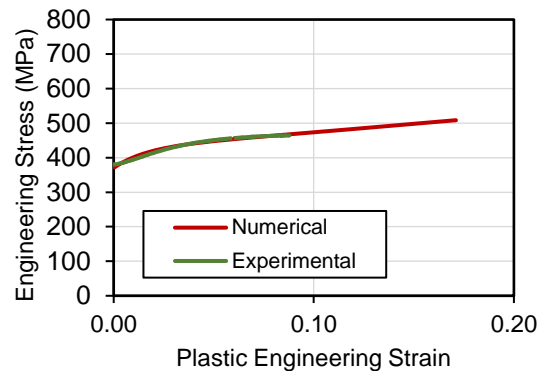
Element	$\sigma^0, \sigma _0$ (MPa)	$C$	$\gamma$	$Q_\infty$	$b$
Plates	400	2200	18	0	0
SOFMAN Pin	420	8000	100	0	0
IST Pin	380	3400	58	0	0



(a)



(b)



(c)

Figure 5-3: Combined hardening calibration: (a) plate material, (b) SOFMAN pin material and (c) IST pin material.

### 5.2.3. Mesh, contact, interactions, boundary conditions and loads

Standard elements C3D8R, composed of an 8-node linear brick, reduced integration and standard hourglass control were used. The pin mesh dimensions have an approximate global size of 4 mm. The eye-bar plates mesh is refined in the proximity of the pin with an approximate global size of 5 mm. In the case of the circular pin section models the weld elements have an approximate global size of 4 mm, similarly to the pin. The remaining components mesh sizes were considered so that every adjacent component has a mesh size ratio inferior to three.

Surface-to surface contact interactions with finite sliding and low friction coefficient were considered. Tie constraints were also defined to simulate the welded connections between the different elements of the device model.

In the case of the symmetry model used for the chamfered pin sections the model has plane cuts. For these plane cuts normal displacements and corresponding rotation are nulled. Besides this, all elements are free but the end plates, one is completely fixed, simulating the bolted connection to the column and the other is fixed with the exception of the axial displacements imposed.

The imposed displacements were applied in the exterior surface of the end plate and defined with the exact same amplitude of the displacements imposed experimentally for each test.

The Figure 5-4 shows the geometry, the mesh size and the boundary conditions considered for the symmetry model and the full model developed. The colours of the figures represent the different materials defined: red for the pin material, grey for the welds material and green for the plate elements material.

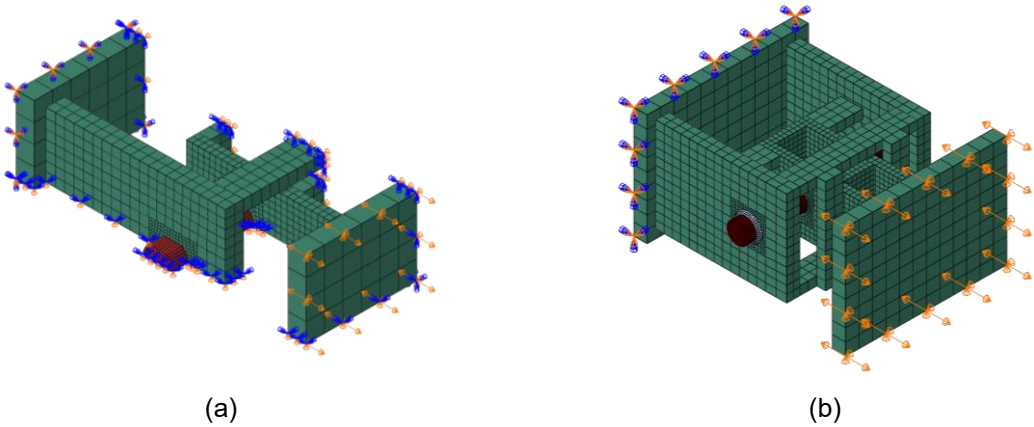


Figure 5-4: Numerical model representation: (a) symmetry model for chamfered section configurations, (b) full model for circular section configurations.

**5.2.4. Type of analysis**

The development of the finite element model of the DRBrC connection was performed through a nonlinear static type of analysis. According to ABAQUS documentation (ABAQUS, 2012) a static analysis is used when inertia effects and time-dependent material effects, such as creep or viscoelasticity, can be neglected. This type of analysis takes rate-dependent and hysteretic behaviour into account. Moreover, in order to access the elastic-plastic resistance for ultimate limit states the choice of the finite element method must be nonlinear for both material and geometric behaviours (EN1993-1-5, 2006, p.45-49).

**5.2.5. Output variables**

The total reaction force of the system is given by the sum of the requested axial reaction force for each node at the exterior surface of the completely fixed end plate. Whereas the displacement is requested by the axial displacement at the node of the moving end plate.

Furthermore, the force-displacement curves are determined by combining the imposed displacement with the total reaction force in the postprocessing of the output database files. An example of a script developed to do this automatically and meant to be applied in the case of the symmetry model is presented in Annex C.

Beyond this, Von Mises stress, equivalent plastic strain *PEEQ*, as well as the normal stress  $\sigma_{33}$  were requested. Von Mises stress is used to predict yielding of materials under complex loading from the results of uniaxial tensile tests. It is mostly used for ductile materials, such as steel. The von Mises yield criterion states that if the von Mises stress of a material under load is equal or greater than the yield limit of the same material under simple tension then the material will yield. Similarly, to evaluate if the material has reached inelastic deformation, the equivalent plastic strain, *PEEQ*, is used.

This value may contain errors from the extrapolation process, therefore, in this work, this value is taken as a qualitative evidence of the inelastic deformation. If this variable is greater than zero, the material has yielded. Finally, normal stresses  $\sigma_{33}$  were requested to access the symmetrical behaviour of the DRBrC device. As well as to compare the dimensions of the normal stresses between the chamfered section and the circular section.

### 5.3. Numerical Results

The resulting force-displacement curves for each numerical model test are presented in Annex B along with the experimental force-displacement curves. Following sections present the values obtained experimentally of the Von Mises stresses, normal stress  $\sigma_{33}$  and  $PEEQ$  for a chamfered pin configuration and a circular pin configuration simulations, namely the 02R and 16C.

#### 5.3.1. Chamfered section tests

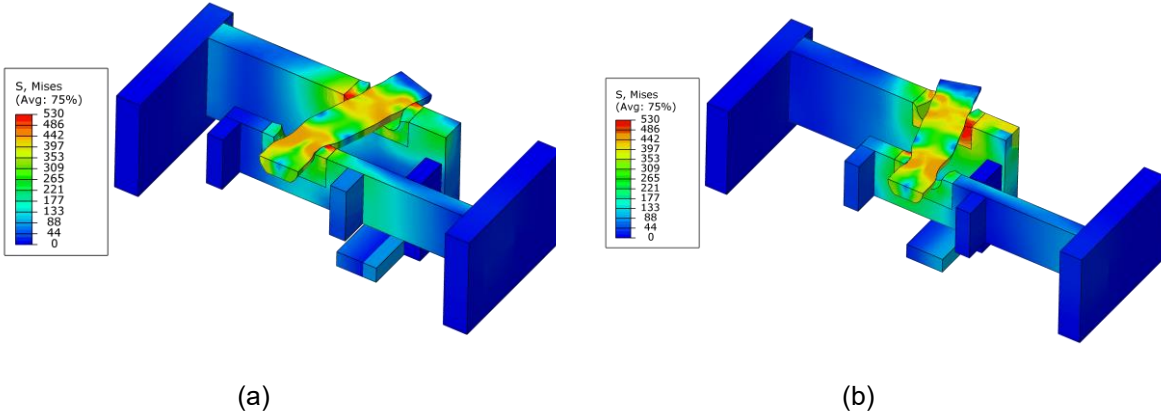


Figure 5-5: Von Mises stresses for the numerical model of test 02R: (a) bracing under tension, (b) bracing under compression.

The Figure 5-5 shows the Von Mises stresses for an advanced cycle of test 02R. It is possible to verify the clear symmetry of the stresses whether the bracing is under tension or under compression.

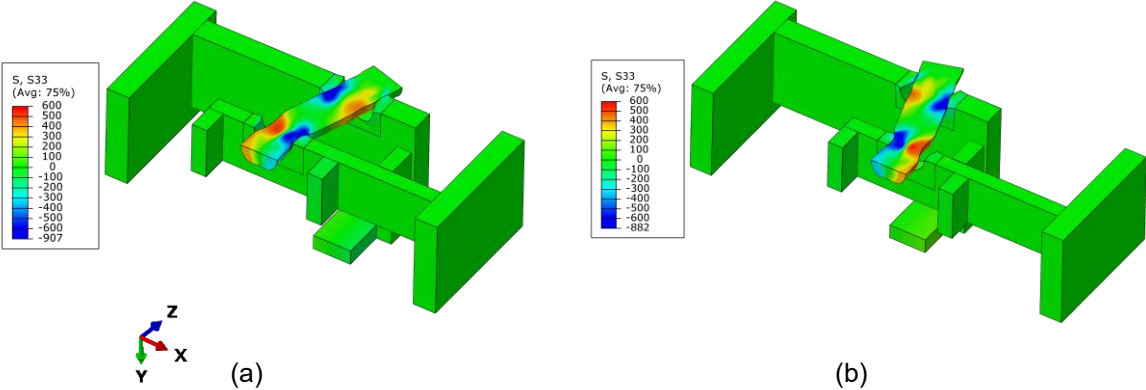


Figure 5-6: Normal stresses  $\sigma_{33}$  for the numerical model of test 02R: (a) bracing under tension, (b) bracing under compression.

The Figure 5-6 shows the normal stresses  $\sigma_{33}$  at an advanced cycle of test 02R. Again, it is possible to verify the symmetry whether the bracing is under tension or compression.

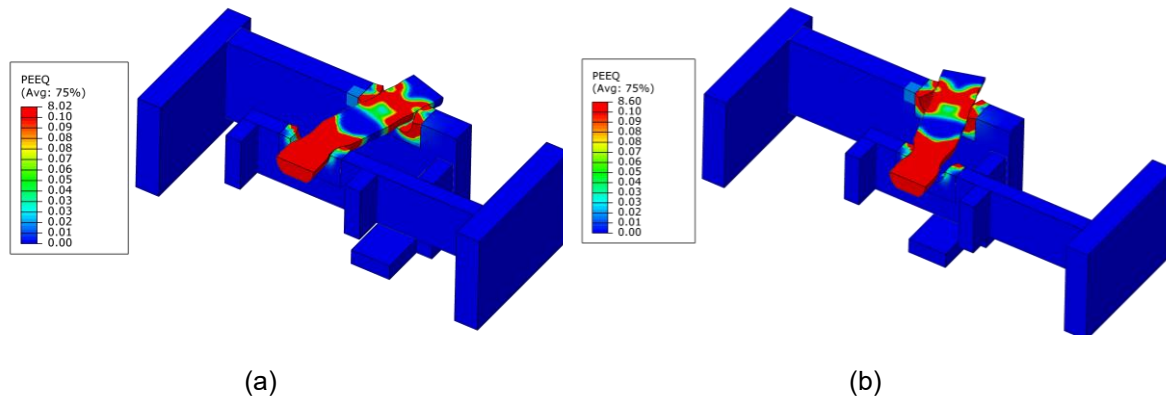


Figure 5-7: Equivalent plastic strains  $PEEQ$  for the numerical model of test 02R: (a) bracing under tension, (b) bracing under compression.

In order to evaluate which elements reached the yielding point,  $PEEQ$  values are represented in Figure 5-7. The elements in dark blue did not leave the elastic range. The pin element has reached yielding stresses for almost all its geometry. The eye-bar plates reached the plastic range in the proximity of the pin contact, this is verified in the ovalization of the plates. All the other device elements remained in the elastic state.

### 5.3.2. Circular section tests

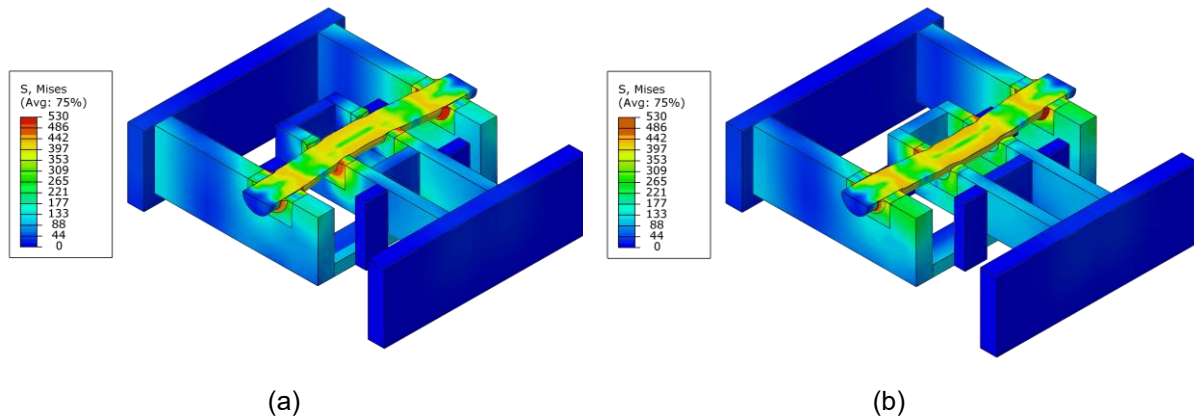


Figure 5-8: Von Mises stresses for the numerical model of test 16C: (a) bracing under tension, (b) bracing under compression.

The Figure 5-8 shows the Von Mises stresses at an advanced cycle for the test 16C. There is a clear symmetry of the stresses. In this case the welds and the contact areas present the higher stresses.

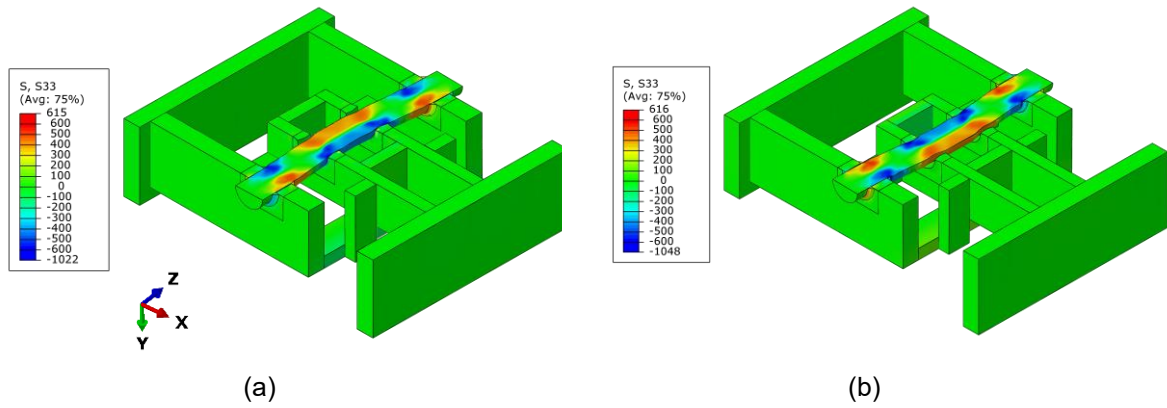


Figure 5-9: Normal stresses  $\sigma_{33}$  for the numerical model of test 16C: (a) bracing under tension, (b) bracing under compression.

The Figure 5-9 shows the normal stresses  $\sigma_{33}$  at an advanced cycle of test 16C. The symmetry is clear. Comparing the Figure 5-9 with the Figure 5-6, it is possible to observe that the circular pin configuration develops higher values of normal stresses than the chamfered pin configuration. Additionally, the area affected with these stresses is broader in the circular pin configuration.

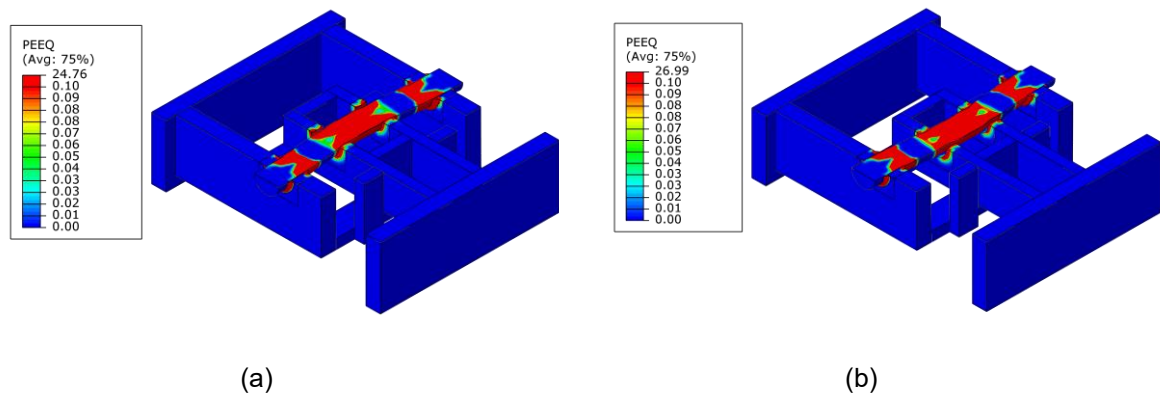


Figure 5-10: Equivalent plastic strains  $PEEQ$  for the numerical model of test 16C: (a) bracing under tension, (b) bracing under compression.

The Figure 5-10 shows the  $PEEQ$  values for an advanced cycle of the test 16C. Almost all the pin element is in the plastic range. The welds and the proximity interface pin-plate are in the plastic range. All the remaining elements remain in the elastic range.

## 6. Numerical-Experimental Comparison

Based on two experimental tests, one with chamfered pin section and one with circular pin section, a comparison between obtained experimental results and numerical results is presented. The damage criteria was investigated in the circular pin section numerical model.

The validation of the numerical models consists of verifying that the numerical models faithfully simulate the observed experimental behaviour of the device. In order to do this the numerical and experimental force-displacement curves, envelope curves, excursion diagrams, peak force diagrams, and dissipated energy diagrams were analysed.

### 6.1. Chamfered pin tests

The test selected to represent the chamfered pin tests is the test 02R. The force-displacement curve obtained numerically was plotted along with the experimental force-displacement curve and envelope curve in Figure 6-1. The numerical force-displacement curve did not show the gradual stiffness degradation in the unloading phases and showed a more pronounced yielding softening at the advanced cycles. Nevertheless, the maximum force as well as the plateaus, where the force variation is small, seen in the numerical force-displacement curve show an excellent correspondence to the experimental force-displacement curve. Therefore, it is possible to say that the numerical model is validated.

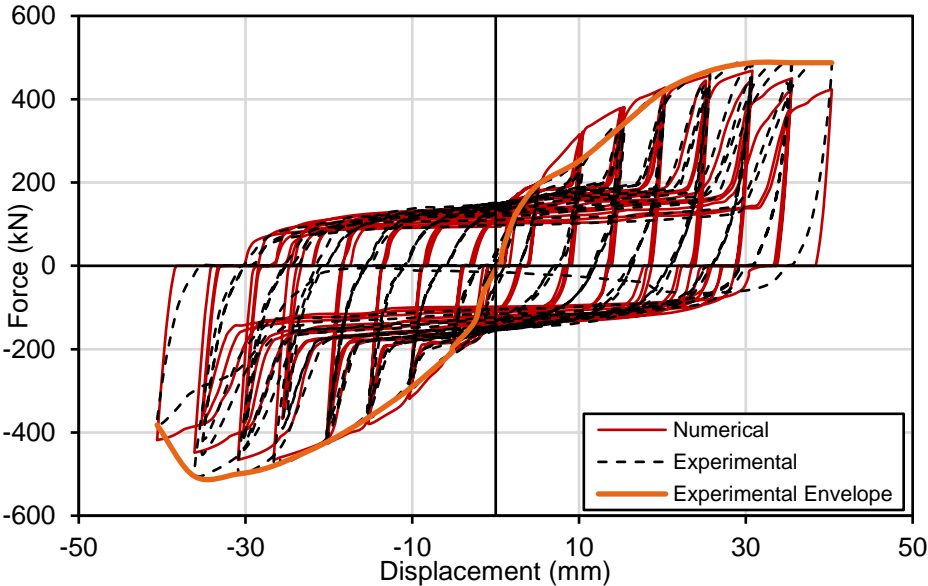


Figure 6-1: Force-displacement curves comparison for test 02R.

The Figure 6-2 shows the envelope curves obtained both experimentally and through the numerical models for test 02R along with the force-displacement curve obtained for the monotonic tests performed numerically. It is possible to see that the stiffness of the numerical model is higher in the beginning of the plastic range, but at the end the yielding degradation of the numerical model is greater than the obtained experimentally. Nevertheless, the envelope curves show an excellent correspondence.

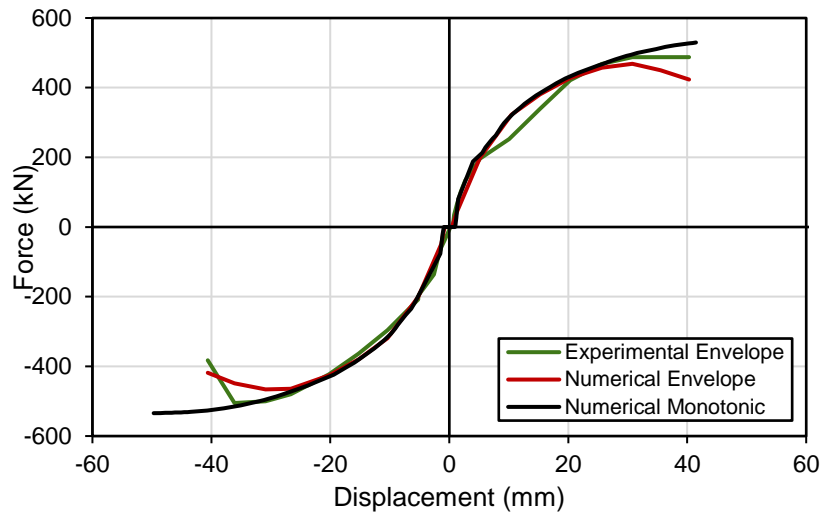


Figure 6-2: Envelope curves comparison for test 02R.

The Figure 6-3 shows the comparison between the peak forces for each half cycle for both experimental and numerical tests. In the range of the 7<sup>th</sup> to 12<sup>th</sup> positive half cycles, when the bracing is under tension, the numerical peak forces are considerably lower. On the other hand, after the 18<sup>th</sup> cycle the numerical peak forces are generally lower than the obtained experimentally.

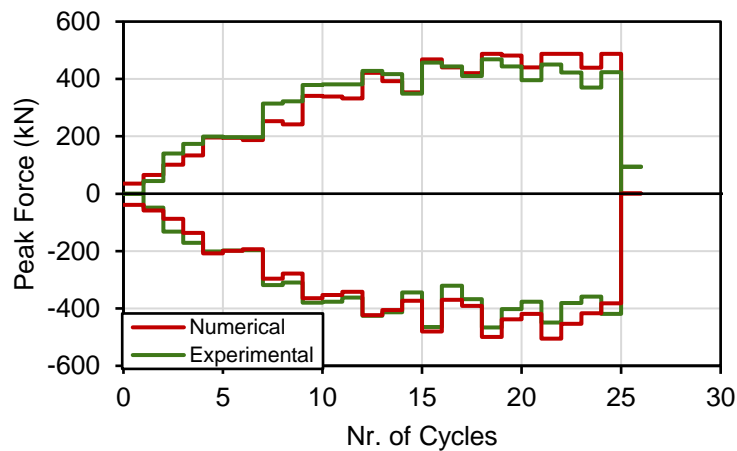


Figure 6-3: Peak force for each half cycle comparison for test 02R.

Furthermore, a comparison between the excursions for each half cycle is presented in Figure 6-4. Although it was expected for the numerical and experimental excursions to be identical, the numerical excursions showed generally higher values. The reason for this has already been stated which is due to the numerical models not capturing the stiffness degradation in the unloading phases.



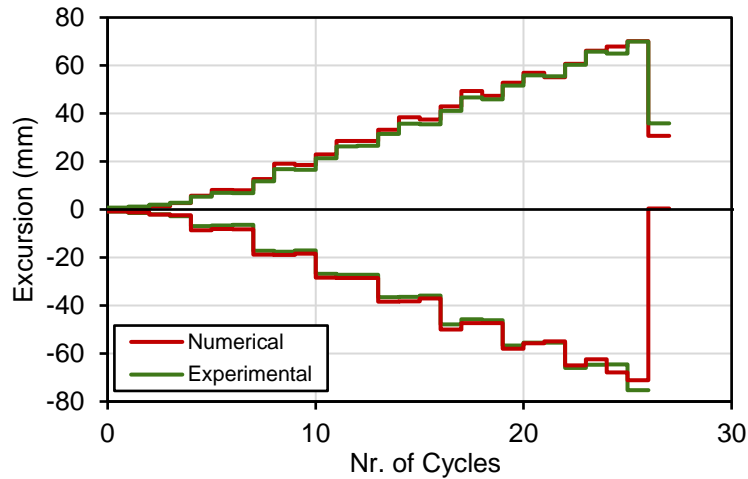


Figure 6-4: Excursion for each half cycle comparison for test 02R.

Finally, a visual comparison regarding the deformation of the pin is depicted in Figure 6-5. The numerical visualization was obtained by mirroring the planes of symmetry. The slight unsymmetrical loading observed in the experimental test is not captured in the numerical model. Anyhow, the section reduction and elongation of the pin as well as the ovalization of the plates were simulated in the numerical models in a similar way of how it was observed in the experimental tests.

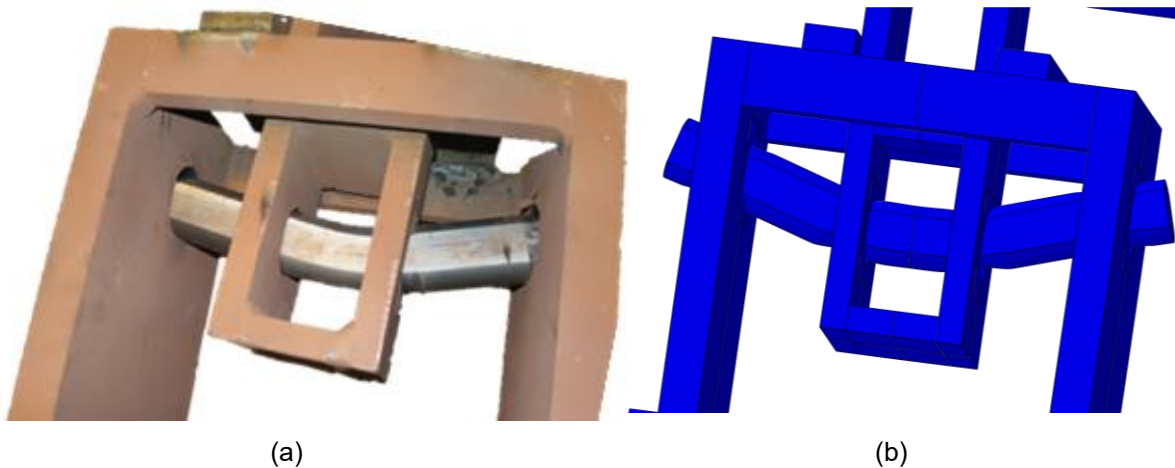


Figure 6-5: Deformation of the pin in test 02R: (a) experimental test, (b) numerical model.

## 6.2. Circular pin test with welded sections

The test selected to analyse the circular pin tests is the 16C. This test showed the highest deviation from the experimental tests results, mainly because it has four welded sections, which the interactions are intricate to simulate and thus make for this test more complex.

The Figure 6-6 shows the force-displacement curve obtained in the numerical models in red, the force-displacement curve obtained in the experimental test in the black dash lines and the experimental envelope in orange. The numerical model failed to simulate the pronounced pinching effect, the yielding softening, and the stiffness degradation on both loading and unloading phases of the hysteresis loop.

This is because the welds were damaged progressively and reached failure soon in the experimental test, an occurrence that the numerical models do not consider. For that reason, damage criteria was investigated in order attain failure in the numerical models and thus validate the model according to the experimental results.

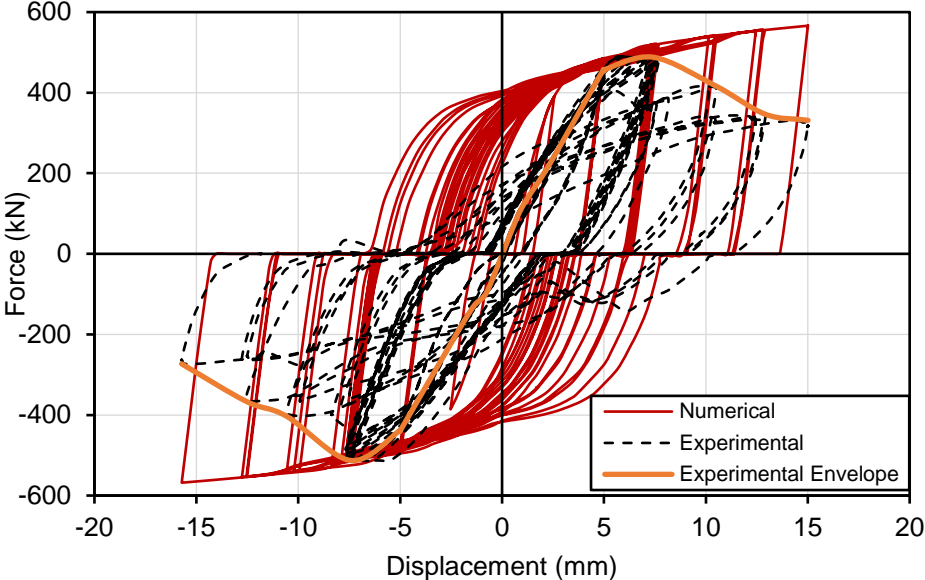


Figure 6-6: Force-displacement curves comparison for test 16C.

**6.2.1. Damage criteria**

The theory applied for modelling progressive damage and failure was the ductile damage, applicable to isotropic ductile metals, together with element deletion. This failure mechanism manifests itself in the softening of the yield stress and degradation of the elastic stiffness (Figure 6-7), and it is defined through a damage initiation criterion and a damage evolution law (ABAQUS, 2012).

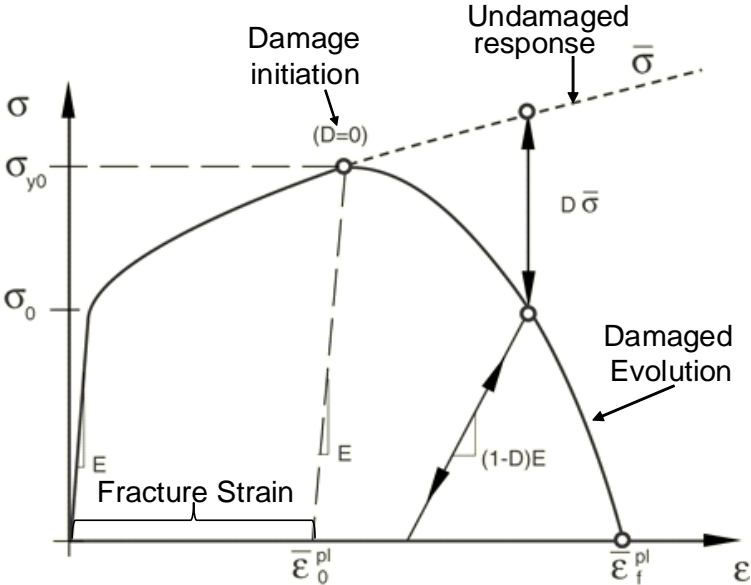


Figure 6-7: Stress-strain curve with progressive damage degradation (adapted from ABAQUS, 2012).

The damage initiation criterion is defined by the fracture strain value, that corresponds to the equivalent true plastic strain at the onset of damage,  $\bar{\epsilon}_0^{pl}$ . The fracture strain is related to the stress at the onset of damage, that corresponds to the ultimate stress,  $\sigma_{y0} = \sigma_u$ .

Once the damage initiation criteria has been reached ( $D=0$ ), the stress tensor in the material follows the law of evolution of the damage, resulting in an increasing loss of the stiffness of the element and may be set to remove the element from the mesh when the failure point is reached ( $D=1$ ).

$$\sigma = (1 - D)\bar{\sigma} \tag{6.1}$$

where,

D is the damage parameter.

$\bar{\sigma}$  is the undamaged stress tensor.

The damage evolution can be defined in various forms, in the present study it is specified in terms of fracture energy  $G_f$  (Hillerborg, 1978). The fracture energy is obtained through the expression (6.2).

$$G_f = \int_{\bar{\epsilon}_0^{pl}}^{\bar{\epsilon}_f^{pl}} L \sigma d\bar{\epsilon}^{pl} = \int_0^{\bar{u}_f^{pl}} \sigma d\bar{u}^{pl} \tag{6.2}$$

where L is the characteristic element length determined by, in the case of linear elements, the cubic root of volume of initial geometry of the element. This variable is introduced into the formulation in order to alleviate the mesh dependency. Because when damage occurs, the stress-strain relationship no longer accurately represents the material's behaviour, therefore instead of defining the deformation after damage initiation as plastic strain, it is defined as an equivalent plastic displacement. (Levanger, 2012) In this case, the energy dissipated during the damage process is specified per unit area, not per unit volume.

The damage criteria is only applied in the pin element and in the welds, since these are the only elements that are subjected to failure conditions. To determine the damage parameters, a process identical to the calibration of the plastic hardening, the simulation of the tensile tests (Figure 6-8), was performed. Through trial and error, the analytically determined parameters were refined through curve fitting of the engineering stress-strain curves obtained experimentally (Figure 6-9), resulting in the parameters shown in Table 6-1. To do this, two Python scripts, presented in Annex C, were developed and applied. The first creates and runs jobs from the tensile test model database file (.cae) with varying fracture strain, fracture energy and mesh size values. The second prints an image file of the stress-strain curve from tensile test output database file (.odb).

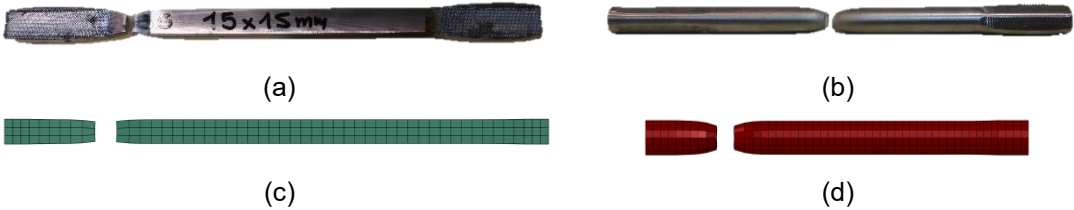


Figure 6-8: Tensile test rupture: (a) & (c) plate element, (b) & (d) pin element.

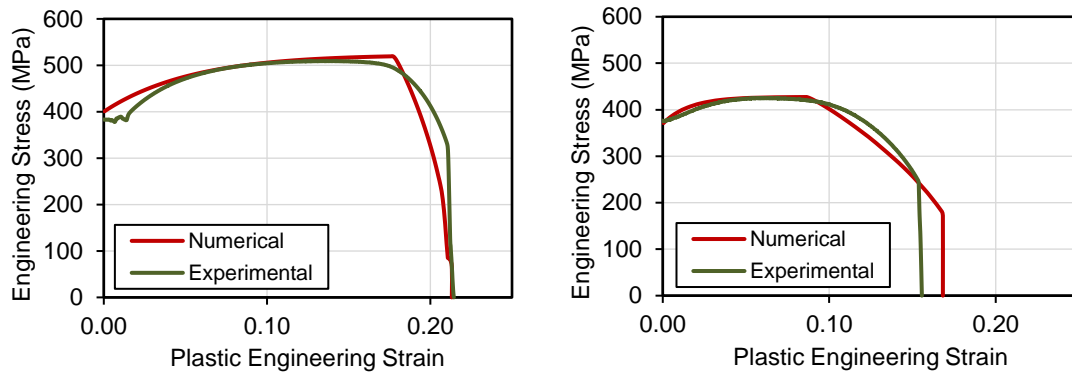


Figure 6-9: Damage criteria calibration: (a) plate elements, (b) pin element.

Table 6-1: Damage parameters for the tensile tests.

Element	Fracture Strain	Fracture Energy ( $N/mm$ )
Pin	0.11	700
Plate/Weld	0.22	700

Afterwards the concept was applied to the numerical model of test 16C. In the case of the numerical models for the DRBrC devices the fracture energy was determined through the force-displacement curve obtained experimentally divided by what can be referred as the equivalent area of the numerical model elements.

$$G_f = \int_0^{\bar{u}_f^{pl}} \frac{F}{L^2} d\bar{u}^{pl} \quad (6.3)$$

Wherefore the fracture strain and fracture energy values that define the damage for this test are presented in Table 6-2.

Table 6-2: Damage parameters for the numerical test 16C.

Element	Fracture Strain	Fracture Energy ( $N/mm$ )
Pin	0.11	6800
Plate/Weld	0.22	6800

The force-displacement curve obtained from the numerical test with implemented damage criteria for test 16C is shown in Figure 6-10. It is possible to verify the clear softening of the yield stress with the increasing of the imposed displacements. Additionally, although the stiffness degradation cannot be clearly observed in the numerical force-displacement curve, it was verified analytically. It was confirmed that the rate of the softening of the yield stress was equivalent to the rate of stiffness degradation, and thus related to the damage parameter. For that reason, the ductile damage evolution did manifest itself as expected.

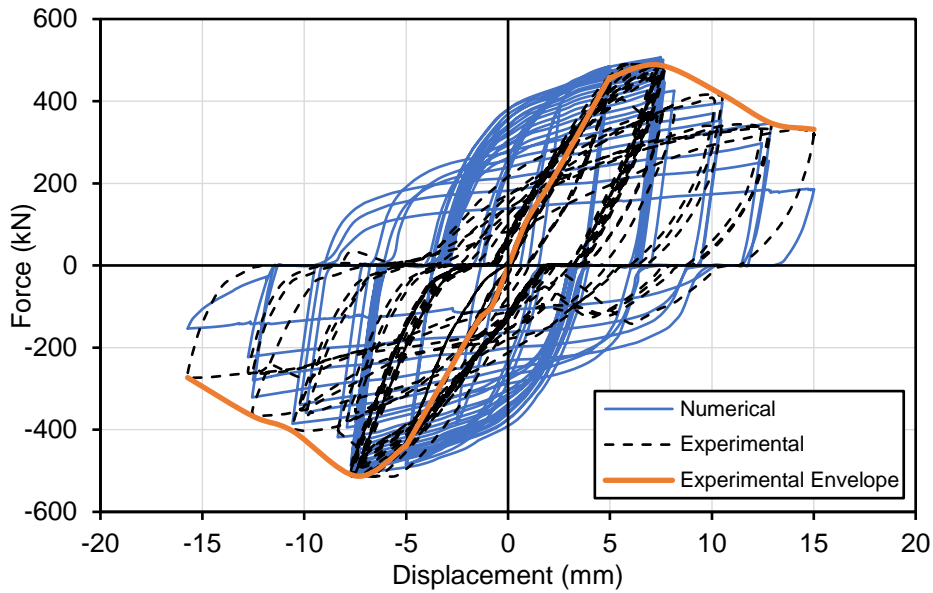


Figure 6-10: Force-displacement curves comparison for test 16C with implemented damage criteria.

The Figure 6-11 shows the envelope curves obtained. The softening of the yield stress obtained in the numerical model is close to the softening obtained experimentally. On the other hand, the initial stiffness is superior for the numerical models.

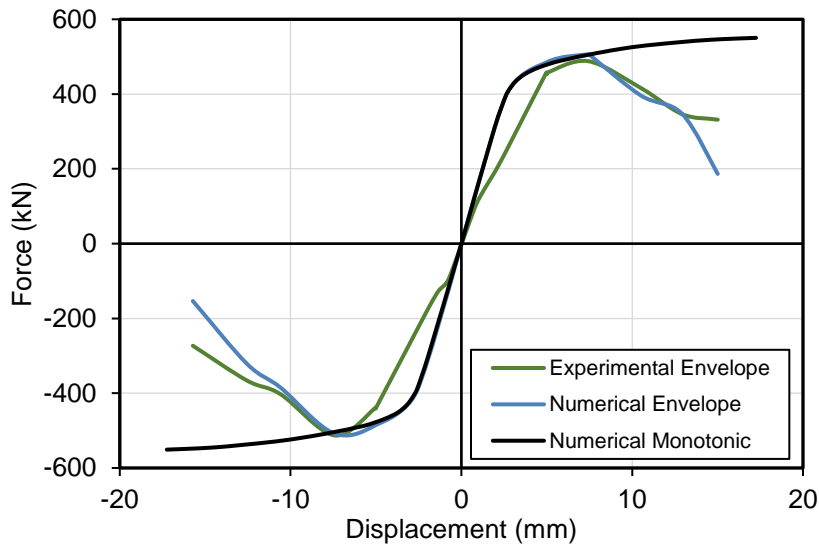


Figure 6-11: Envelope curves comparison for test 16C with implemented damage criteria.

The Figure 6-12 shows the excursion for each half cycle. Unexpectedly, the excursion values for the negative excursions, the compressive direction on the bracing, are generally higher in the numerical model with damage. One reason for that is that the numerical models with damage develop less ovalization in the interior plates, due to the progressive pin damage, and thus the slip for null force is reduced for these models.

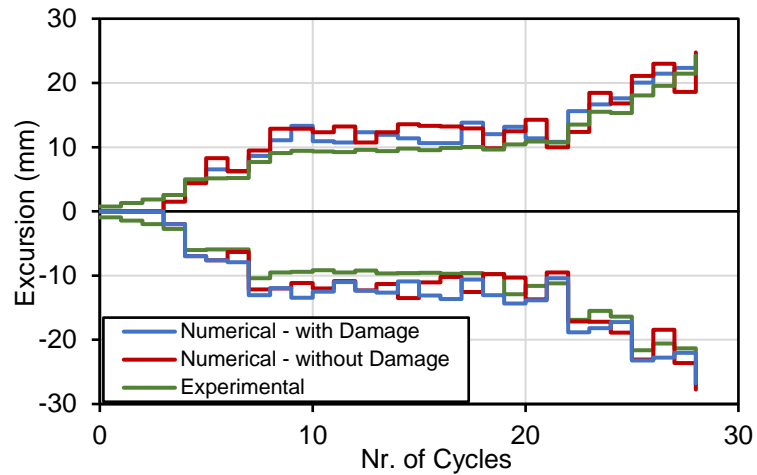


Figure 6-12: Excursion for each half cycle comparison for test 16C.

The Figure 6-13 shows the peak force for each half cycle. The increased quality of the model with implemented damage is clear.

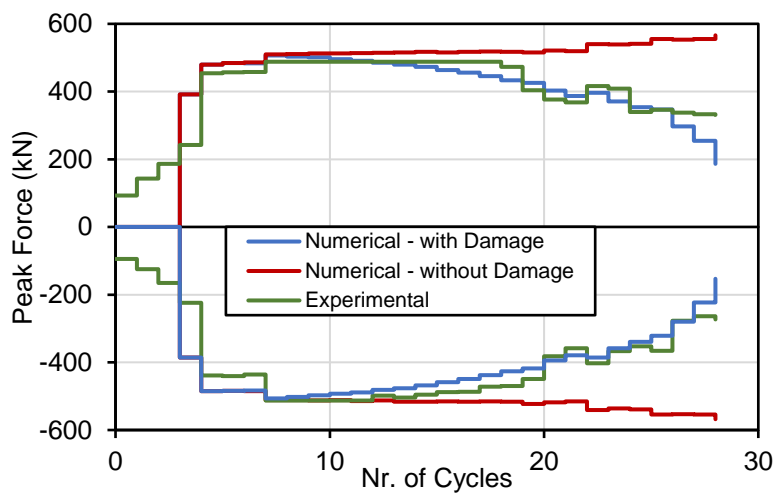


Figure 6-13: Peak force for each half cycle comparison for test 16C.

Finally, the failure mode at the end of the simulation is presented in Figure 6-14. The shear failure mode of the pin near the interior welded sections obtained in the numerical models was very similar to what was observed at the end of the experimental test.

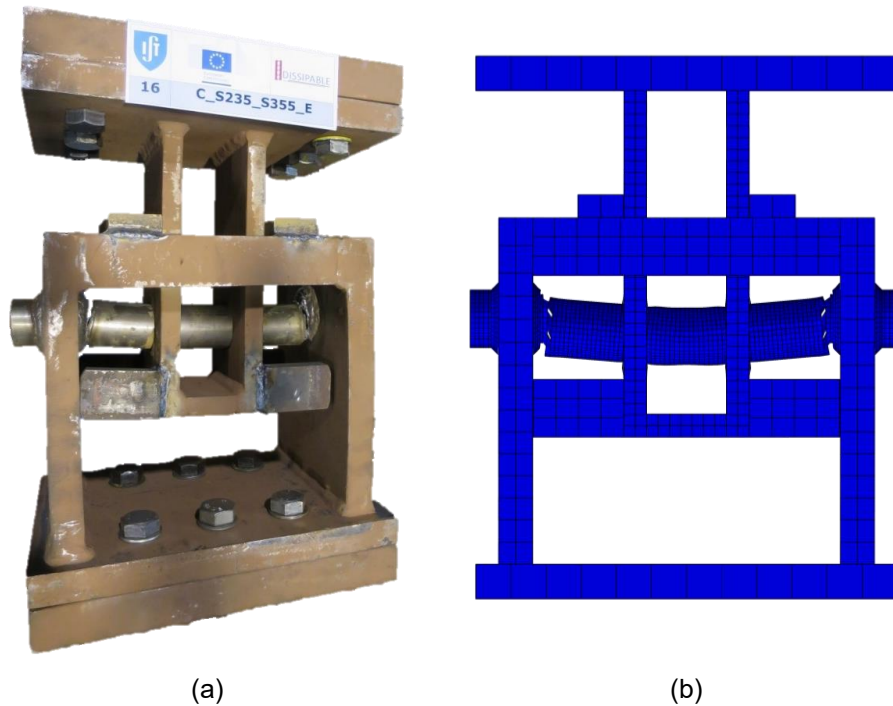


Figure 6-14: Failure mode of test 16C: (a) experimental test, (b) numerical model.

Lastly, Table 6-3 shows the peak forces, both in tensile and compressive directions, and total dissipated energy obtained in the experimental and numerical results. Along with the ratio between these numerical and experimental results in the rightmost column. The ratios reveal in a summarized way a general evaluation of the different numerical model configurations performance regarding the experimental results. Generally, the peak forces obtained are in the safety side because they are smaller in the numerical models, thus in this way the numerical models are conservative.

In the other hand the total dissipated energy is for all cases overestimated, and thus against safety. This is due to the issues presented earlier in the numerical model results comparison, mainly the trimmed force-displacement curves obtained in the experimental tests and the missing stiffness degradation at the unloading phases of the numerical force-displacement curves.

The numerical tests that showed a higher discrepancy from the experimental results are the 15C and 16C, and thus presented in red. The test 15C discrepancy is due mainly to the trimmed force-displacement curve obtained experimentally, where this test data collection was heavily affected. The test 16C discrepancy is caused by the reasons stated before. Additionally, because it is the configuration with a higher number of welded sections, the behaviour of test 16C is the most complex to simulate and the issues, like the pinching effect are intensified. Nevertheless, with the implemented damage criteria better results were obtained.

Table 6-3: Numerical-experimental peak forces and dissipated energy comparison.

Test acronym	Experimental			Numerical			Numerical/Experimental		
	$F_{max}^+$ (kN)	$F_{max}^-$ (kN)	$W_t$ (kNm)	$F_{max}^+$ (kN)	$F_{max}^-$ (kN)	$W_t$ (kNm)	$F_{max}^+$ (kN)	$F_{max}^-$ (kN)	$W_t$ (kNm)
01R	505	-474	109	458	-466	123	0.91	0.98	1.12
02R	488	-505	224	469	-466	244	0.96	0.92	1.09
03R	488	-513	200	481	-486	225	0.99	0.95	1.13
04R	486	-487	209	464	-467	240	0.95	0.96	1.15
15C	527	-474	190	597	-537	310	1.13	1.13	1.63
16C	488	-513	97	566	-568	219	1.16	1.11	2.25
				507*	-507*	176*	1.04*	0.99*	1.80*
17C	487	-514	452	484	-501	554	0.99	0.97	1.23
18C	487	-514	339	461	-490	394	0.95	0.95	1.16

Note (\*): Numerical model with implemented damage criteria.



## 7. Conclusion and Further Developments

### 7.1. General conclusions

The main goal of this work was to access the local behaviour of different configurations of the DRBrC dissipative device through experimental and numerical studies.

Despite the limitations referred in section 4.1, the experimental tests were carried successfully and gather much information from the performance of the pin device. A major improvement on the pin device configuration was implemented during the experimental tests phase, the guiding plates. The guiding plates showed many benefits and should be considered as an integral component of the DRBrC pin device (Figure 7-1). Additionally, the DRBrC device proved to be fully replaceable.

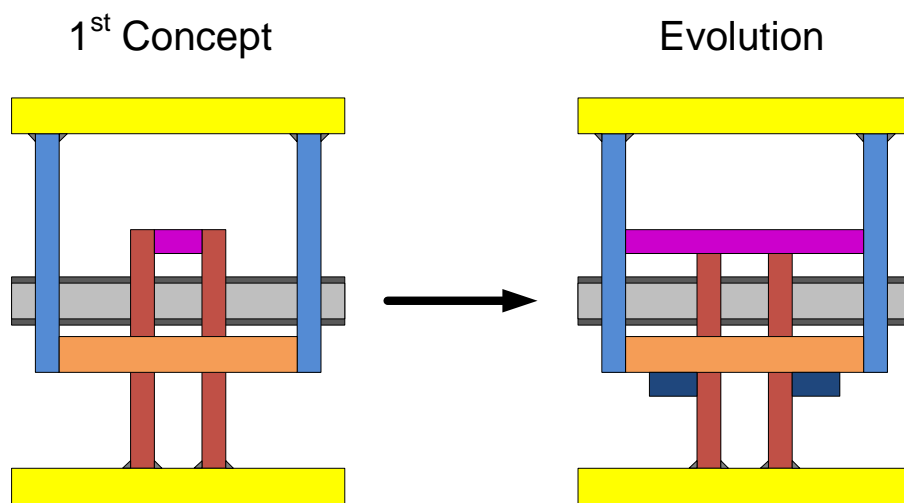


Figure 7-1: The evolution of the DRBrC device: guiding plates.

The numerical models developed adequately simulate the results obtained experimentally, despite presenting a deviation in the results, that arise from the encountered issues:

- The pinching phenomena was not captured by the numerical models.
- Meshing, it is possible to obtain closer results with a more detailed study of the type of elements and characteristic length of the mesh. Mesh convergence study was not the focus, thus the models presented still have room for improvements regarding its efficiency and results refinement.
- Characterization of the material can be further improved considering that the isotropic hardening component was not applied.
- Dimensions of the different components of the device were approximate and not exact.
- The experimental tests show a small eccentricity in the movement and rotations that the numerical models are not able to simulate, this problem is not present in the simulations because the centralization of the system is easily guaranteed.
- The experimental tests present trimmed force-displacement results, as referred before.

It is important to note that this work did not aim to develop advanced numerical models, but rather to develop models in a way that can serve as an auxiliary tool for the evaluation and development of the pin device DRBrC.

The combined hardening characterization could not be performed rigorously because no cyclic tensile tests were performed to characterize the cyclic behaviour of the steel materials. Nevertheless, the numerical models developed allowed for a more in-depth evaluation.

Regarding the pin device performance evaluation, the best configuration is the chamfered pin section, with the application of both guiding plates, GP1 and GP2. The pin device configurations with a circular section and welded sections, although resulting in remarkably higher dissipated energy values, showed an expected early brittle failure of the welds. In real life applications this could cause greater consequences, due to the sudden and more unpredictable response.

## **7.2. Further Developments**

This dissertation refers to the first part of a succession of experimental tests on the local behaviour of DRBrC the pin device. Therefore, more experimental tests will be carried out which will allow to acquire more information to better understand the device behaviour. The finite element models along with the Python scripts developed in this work can be updated to consider not only the geometrical modifications and design changes but also material characteristics. Consequently, the next specified experimental test configurations can already have expected values obtained from the numerical models. In the following experimental studies of the connection it is suggested that cyclic tensile tests are performed as suggested in the combined hardening calibration method (Myers et al., 2009, Appendix D) applied in this work. The ductile damage criteria developed showed to be a promising tool but should be further investigated. Thus, standard damage characterization tests on the material can be investigated and performed.

## References

- ABAQUS, 2012. Analysis User's Manual, Version 6.12. Dassault Systèmes, Providence, RI.
- Alehashem, S.M.S., Keyhani, A., Pourmohammad, H., 2008. Behavior and Performance of Structures Equipped With ADAS & TADAS Dampers (a Comparison with Conventional Structures). In: The 14th World Conference on Earthquake Engineering. Beijing.
- Amiri, H.A., Najafabadi, E.P., Estekanchi, H.E., Ozbakkaloglu, T., 2020. Performance-based seismic design and assessment of low-rise steel special moment resisting frames with block slit dampers using endurance time method. *Engineering Structures* 224.
- ASTM A370-20, 2016. Standard test methods and definitions for mechanical testing of steel products. ASTM International, West Conshohocken, PA.
- Bruneau, M., Chang, S.E., Eguchi, R.T., Lee, G.C., D. O'rourke, T., Reinhorn, A.M., Shinozuka, M., Tierney, K., Wallace, W.A., Von Winterfeldt, D., 2003. A Framework to Quantitatively Assess and Enhance the Seismic Resilience of Communities. *Earthquake Spectra* 19, 733–752.
- Calado, L., Ferreira, J., Feligioni, S., 2004. Characterization of Dissipative Connections for Concentric Bracing Systems in Steel Frames in Seismic Areas: Report 2 - Detailed Report INERD.
- Carvalho, R.P.N., 2017. Estudo de Dissipadores Histeréticos de Aço - Modelação de uma consola de secção variável. Instituto Superior Técnico.
- Castiglioni, C., Calado, L., Plumier, A., Thanopoulos, P., Vayas, I., 2004. Behaviour of seismic resistant braced frames with innovative dissipative (INERD) connections.
- Chang, K.L., Rees, S.J.W., Carroll, C., Clandening, K., 1999. The use of Triangular Added Damping and Stiffness (TADAS) devices in the design of the Core Pacific City Shopping Centre. *Advances in Steel Structures (ICASS '99)* 775–782.
- DISSIPABLE, 2018. Work package 1 - Deliverable 1.1 Report on evolution of INERD™ and FUSEIS devices into the new DRDs. *Journal of Chemical Information and Modeling* 53, 1689–1699.
- DISSIPABLE, 2020a. Work package 2 - Deliverable 2.2 Report on parametric studies of DRD systems.
- DISSIPABLE, 2020b. Work package 4 - Deliverable 4.1 Report on experimental tests on DRD systems.
- ECCS, 1986. Recommended Testing Procedure For Assessing the Behaviour of Structural Steel Elements under Cyclic Loads. Technical Committee 1 - Structural Safety and Loadings Technical Working Group 1.3 - Seismic Design N° 45, 0–11.
- EN10002-1, 2001. Metallic materials - Tensile testing - Part 1 : Method of test at ambient temperature. (CEN), European Committee for Standardisation.
- EN1993-1-1, 2005. Eurocode 3: Design of steel structures - Part 1-1: General rules and rules for buildings. (CEN), European Committee for Standardisation, Brussels.

- EN1993-1-5, 2006. Eurocode 3: Design of steel structures - Part 1-5: Plated structural elements. (CEN), European Committee for Standardisation, Brussels.
- EN1998-1, 2004. Eurocode 8: Design of structures for earthquake resistance - Part 1 : General rules, seismic actions and rules for buildings. (CEN), European Committee for Standardisation, Brussels.
- Espinha, M., 2011. Hysteretic behaviour of dissipative welded devices for earthquake resistant steel frames. Instituto Superior Técnico.
- Feldmann, M., Hoffmeister, B., Schaffrath, S., Bartsch, H., Münstermann, S., Di, Y., Hoppe, B., Vayas, I., Avgerinou, S., Salvatore, W., Caprili, S., Mussini, N., Karamanos, S., Perdikaris, P., Chatzopoulou, G., Papatheocharis, T., Lindström, B., Pasquale, E. De, 2017. Material Choice for Seismic Resistant Structures (MATCH). European Commission, Brussels.
- Gray, M.G., Christopoulos, C., Packer, J.A., 2010. Cast steel yielding fuse for concentrically braced frames. In: , 9th U.S. National and 10th Canadian Conf. on Earthquake Engineering. Toronto, ON.
- Guerreiro, L., 2011. Estratégias para melhoria do comportamento sísmico de edifícios. Ordem dos Engenheiros, Lisboa.
- Hillerborg, A., 1978. A model for fracture analysis. Report TVBM, vol. 3005, vol. 3005, Division of Building Materials, LTH, Lund University.
- Hradil, P., Fülöp, L., Talja, A., Kurkela, J., 2017. Experiences from numerical modelling of details with ductile fracture. VTT-R-01177-17 1–26.
- Kelly, J.M., Skinner, R.I., Heine, A.J., 1972. Mechanisms of energy absorption in special devices for use in earthquake resistant structures. Bulletin of N.Z. Society for Earthquake Engineering 5.
- Kelly, P., 2013. Solid Mechanics Part II: Engineering Solid Mechanics 300–314.
- Kiggins, S., Uang, C.-M., 2006. Reducing residual drift of buckling-restrained braced frames as a dual system. Engineering Structures 28, 1525–1532.
- Krolo, P., Grandić, D., Smolčić, Ž., 2016. Experimental and Numerical Study of Mild Steel Behaviour under Cyclic Loading with Variable Strain Ranges. Advances in Materials Science and Engineering.
- Levanger, H., 2012. Simulating Ductile Fracture in Steel using the Finite Element Method: Comparison of Two Models For Describing Local Instability due to Ductile Fracture. University of Oslo.
- Myers, A.T., Deierlein, G.G., Kanvinde, A., 2009. Testing and probabilistic simulation of ductile fracture initiation in structural steel components and weldments. Report No. 170 333–350.
- Oh, S.-H., Kim, Y.-J., Ryu, H.-S., 2009. Seismic performance of steel structures with slit dampers. Engineering Structures 31, 1997–2008.
- Plumier, A., Doneux, C., Castiglioni, C., Brescianini, J., Crespi, A., Dell’Anna, S., Lazzarotto, L., Calado,

- L., Ferreira, J., Feligioni, S., Bursi, O., Ferrario, F., Somnavilla, M., Vayas, I., Thanopoulos, P., Demarco, T., 2004. Two innovations for earthquake-resistant design: the INERD project. Luxembourg: European Commission, Research Fund for Coal and Steel 75–130.
- RFCS-02-2017, 2017. DISSIPABLE – Fully Dissipative and Easily Repairable Devices for Resilient Buildings with Composite Steel-Concrete Structures. European Commission, Research Fund for Coal and Steel. POLIMI (coordinator), IST, NTUA, SOFMAN, UNITN, RWTH, CSM, UNIPI.
- Shoeibi, S., Kafi, M.A., Gholhaki, M., 2017. New performance-based seismic design method for structures with structural fuse system. *Engineering Structures* 132, 745–760.
- Soboyejo, W., 2002. *Mechanical properties of engineered materials* (1st ed.). Princeton University Princeton, New Jersey: Marcel Dekker 125–128.
- Symans, M.D., Charney, F.A., Whittaker, A.S., Constantinou, M.C., Kircher, C.A., Johnson, M.W., McNamara, R.J., 2008. Energy Dissipation Systems for Seismic Applications: Current Practice and Recent Developments. *Journal of Structural Engineering* 134, 3–21.
- Taucer, F., Sabau, G.-A., Poljansek, M., Pegon, P., Molina, F.-J., Tirelli, D., Viacoz, B., Stratan, A., Ioan-Chesoan, A., Dubina, D., 2014. DUAREM Full-scale experimental validation of dual eccentrically braced frame with removable links. European Commission, Luxembourg.
- Tehranizadeh, M., 2001. Passive energy dissipation device for typical steel frame building in Iran. *Engineering Structures* 23, 643–655.
- Tirca, L., Danila, N., Caprarelli, C., 2014. Numerical modelling of dissipative pin devices for brace-column connections. *Journal of Constructional Steel Research* 84.
- Vasdravellis, G., Karavasilis, T.L., Uy, B., 2014. Design Rules, Experimental Evaluation, and Fracture Models for High-Strength and Stainless-Steel Hourglass Shape Energy Dissipation Devices. *Journal of Structural Engineering* 140, 04014087.
- Vayas, I., Dimakogianni, P.K.D., Dougka, G., Castiglioni, C.A., Kanyilmaz, A., Calado, L., Proença, J.M., Espinha, M., Hoffmeister, B., Rauert, T., Kalteziotis, D., 2013. Dissipative devices for seismic-resistant steel frames (Fuseis) ( No. RFSR-CT-2008-00032), Research Fund for Coal and Steel. Luxembourg.
- Vayas, I., Thanopoulos, P., Tsarpalis, P., Dimakogianni, D., Henriques, J., Degee, H., Hoffmeister, B., Pinkawa, M., Castiglioni, C.A., Alavi, A., Brambilla, G., Calado, L., Proença, J.M., Sio, J., Chesoaan, A., Stratan, A., Dubina, D., Neagu, C., Dinu, F., Georgiev, T., Raycheva, L., Zhelev, D., Rangelov, N., Morelli, F., Natali, A., Salvatore, W., Butz, C., Renzi, V., Butz, C., Medeot, R., 2017. *Innovative Anti-Seismic Devices and Systems (INNOSEIS)*, 1st ed. ECCS - European Convention for Constructional Steelwork.



# Annex A

## Tensile test stress-strain curves

The tensile tests stress-strain curves obtained experimentally, engineering stress-strain curves, together with the derived true stress-strain curves are presented below. These curves are grouped for the same element material, since each element material had a pair of tensile test specimens with the exception of the pin materials, where different tensile test specimens are involved.

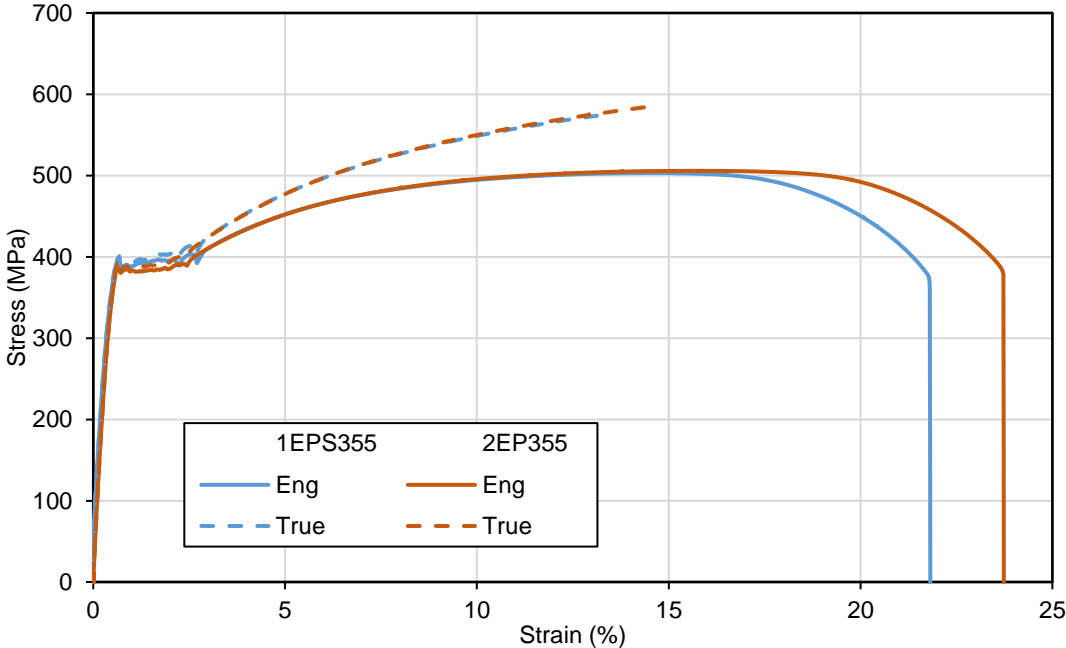


Figure A.-1:Engineering and true stress-strain curves for exterior plates material.

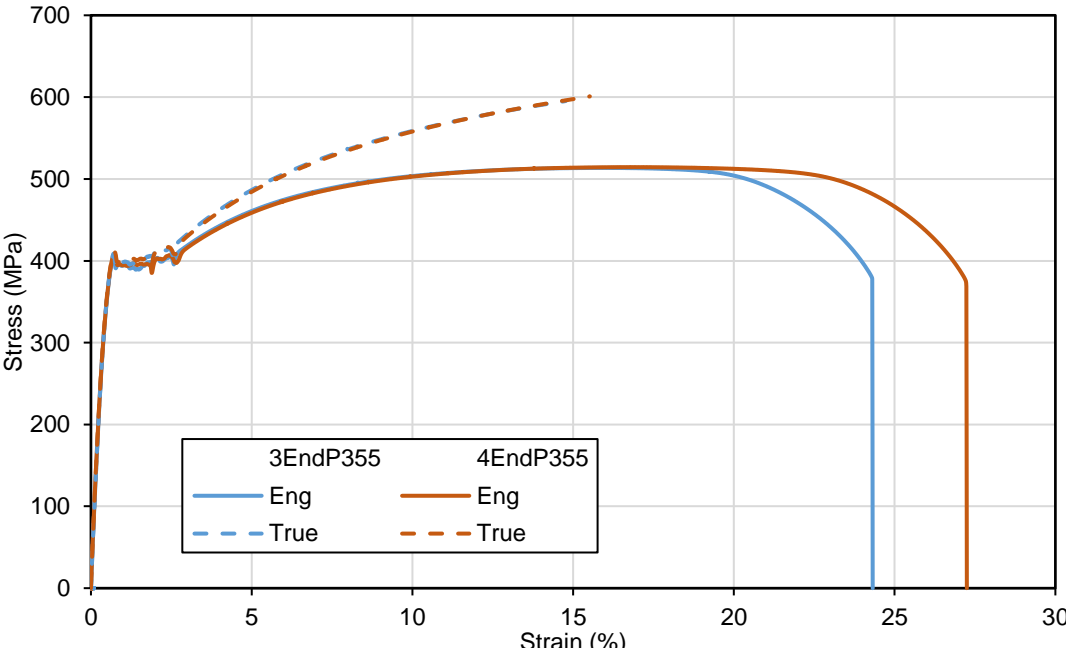


Figure A-2: Engineering and true stress-strain curves for end plates material.

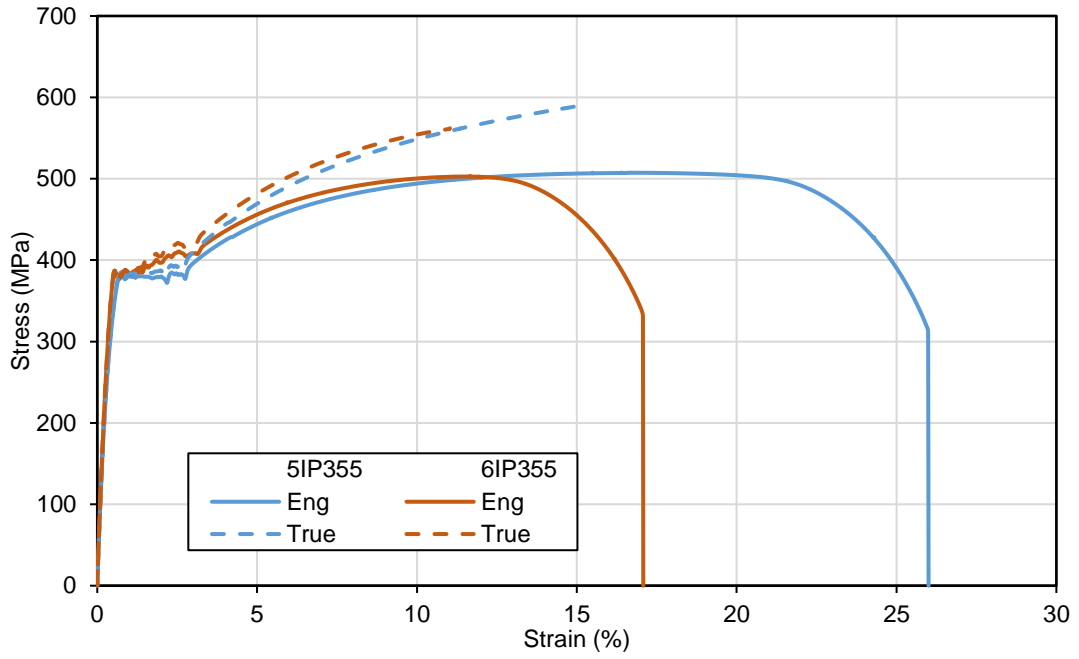


Figure A-3: Engineering and true stress-strain curves for interior plates material.

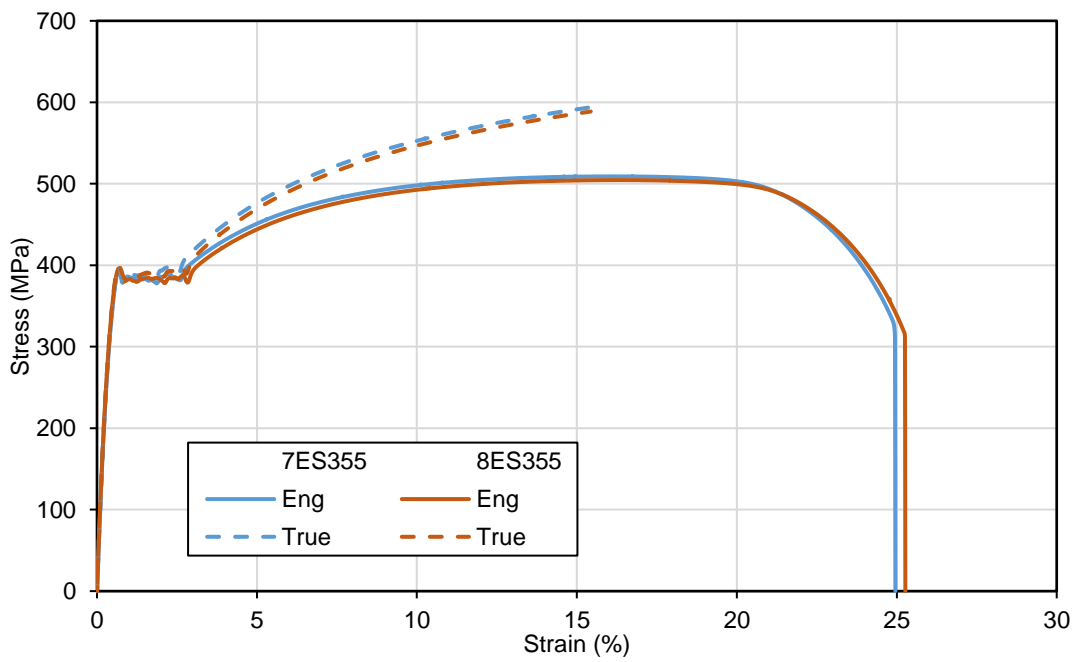


Figure A-4: Engineering and true stress-strain curves for exterior spacers material.



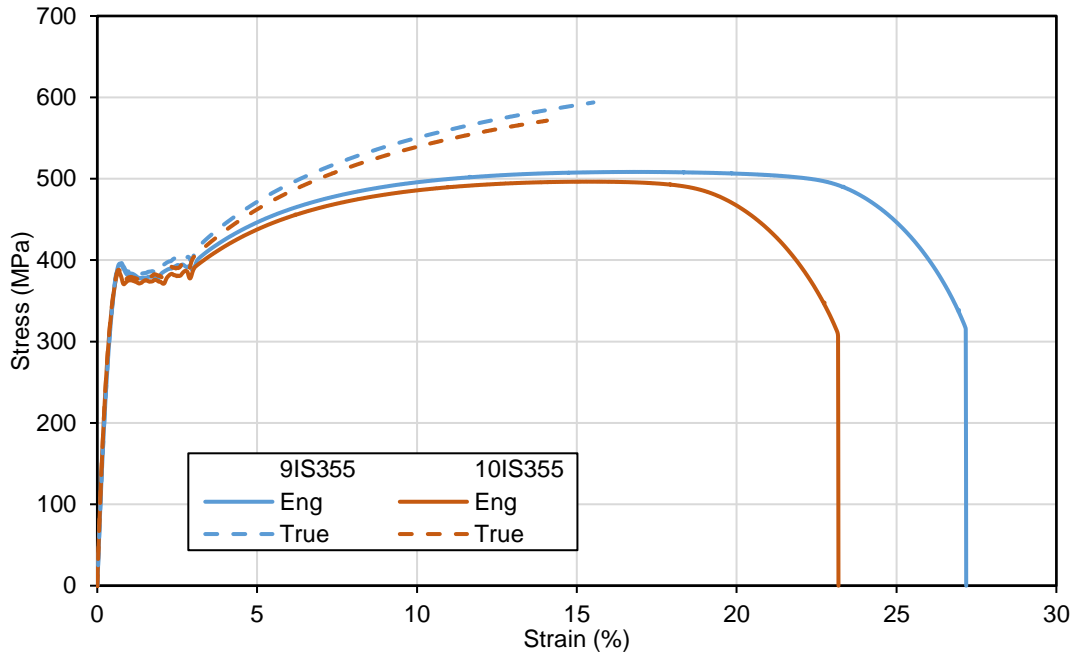


Figure A-5: Engineering and true stress-strain curves for interior spacers material.

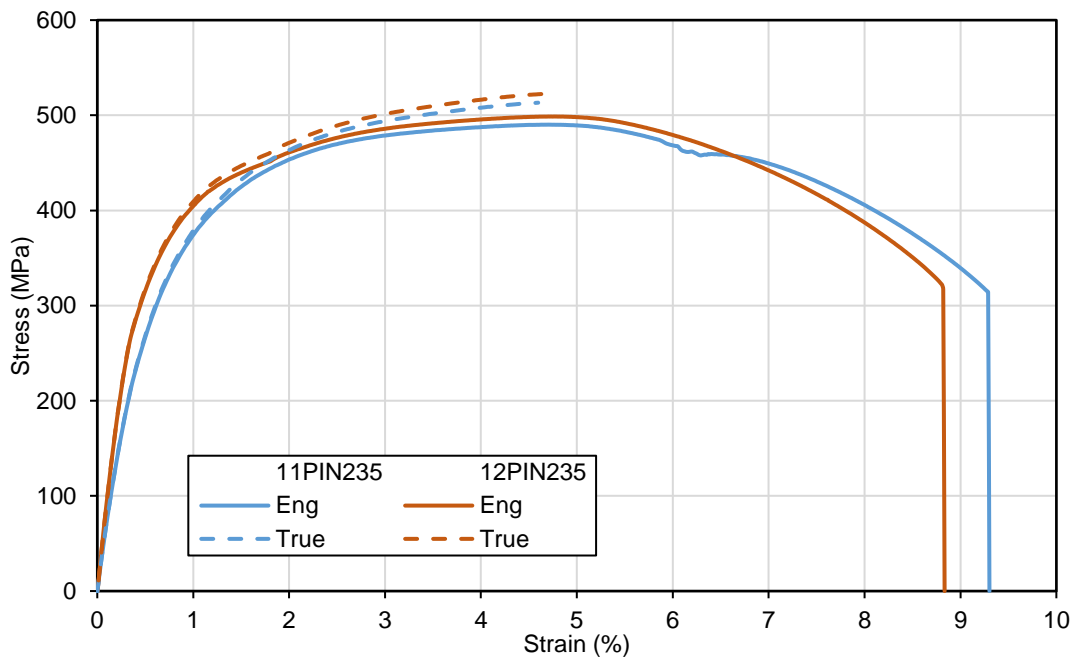


Figure A-6: Engineering and true stress-strain curves for SOFMAN pin material.

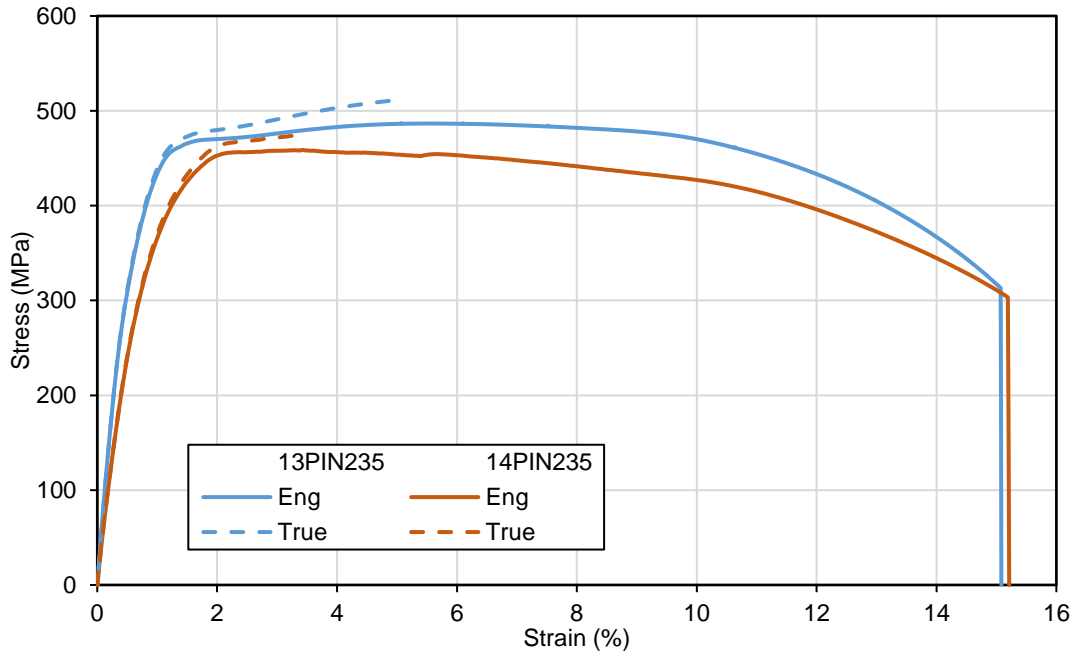


Figure A-7: Engineering and true stress-strain curves for test specimen removed from an untested device corresponding to SOFMAN pin material.

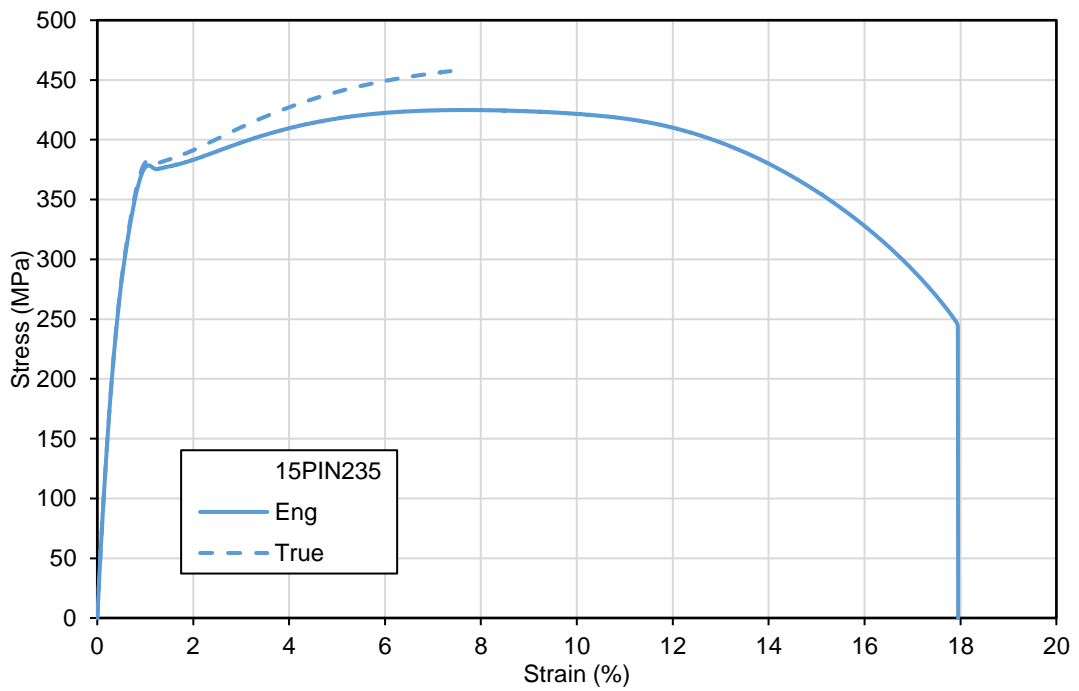


Figure A-8: Engineering and true stress-strain curves for IST pin material.

# Annex B

Numerical and experimental force-displacement curves.

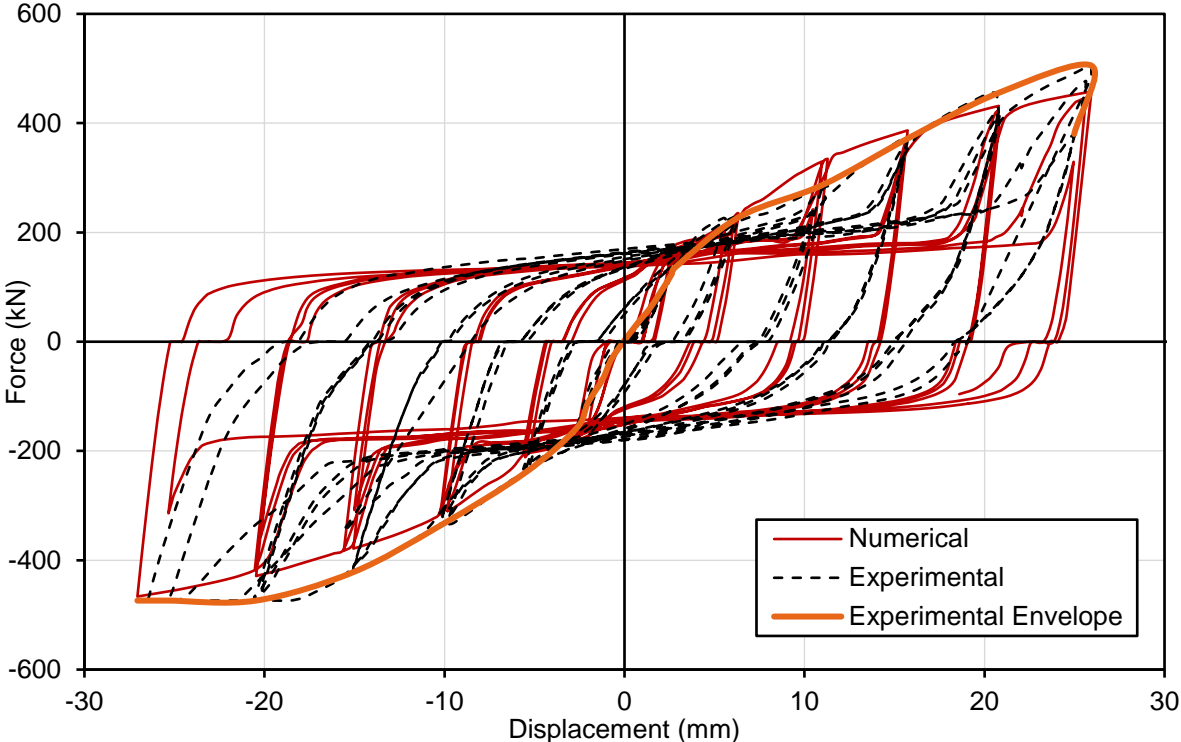


Figure B-1: Force-displacement curves comparison for test 01R.

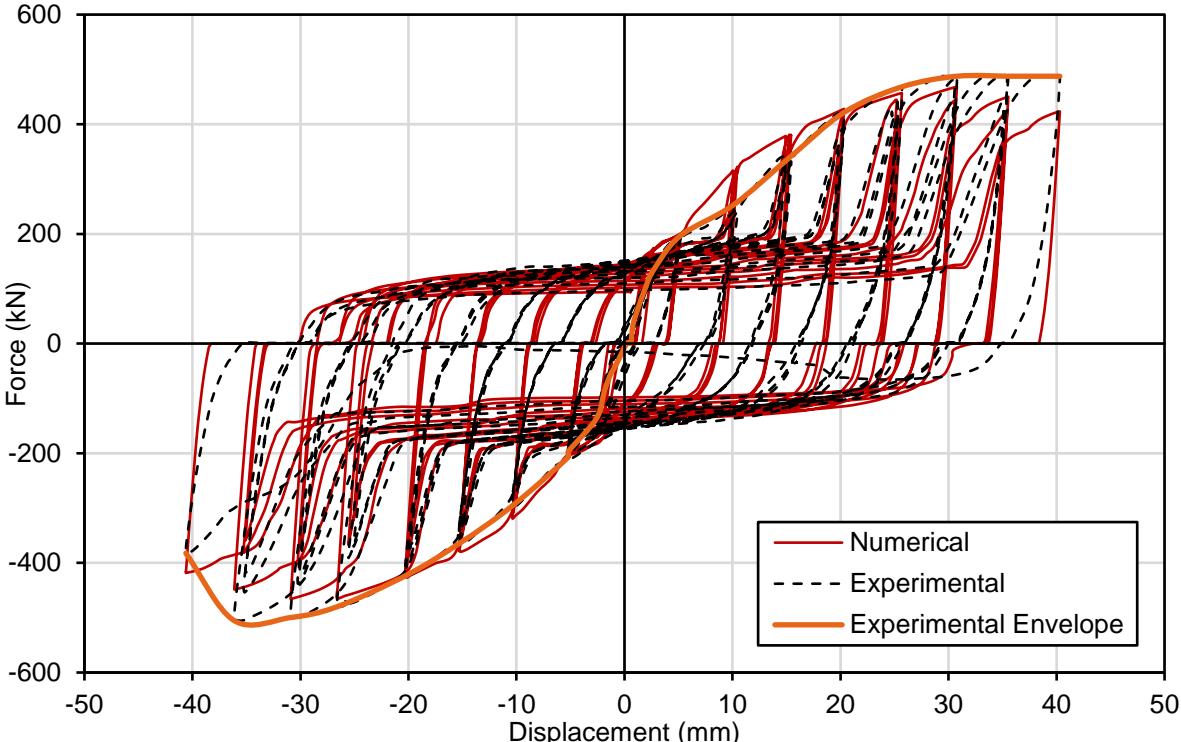


Figure B-2: Force-displacement curves comparison for test 02R.

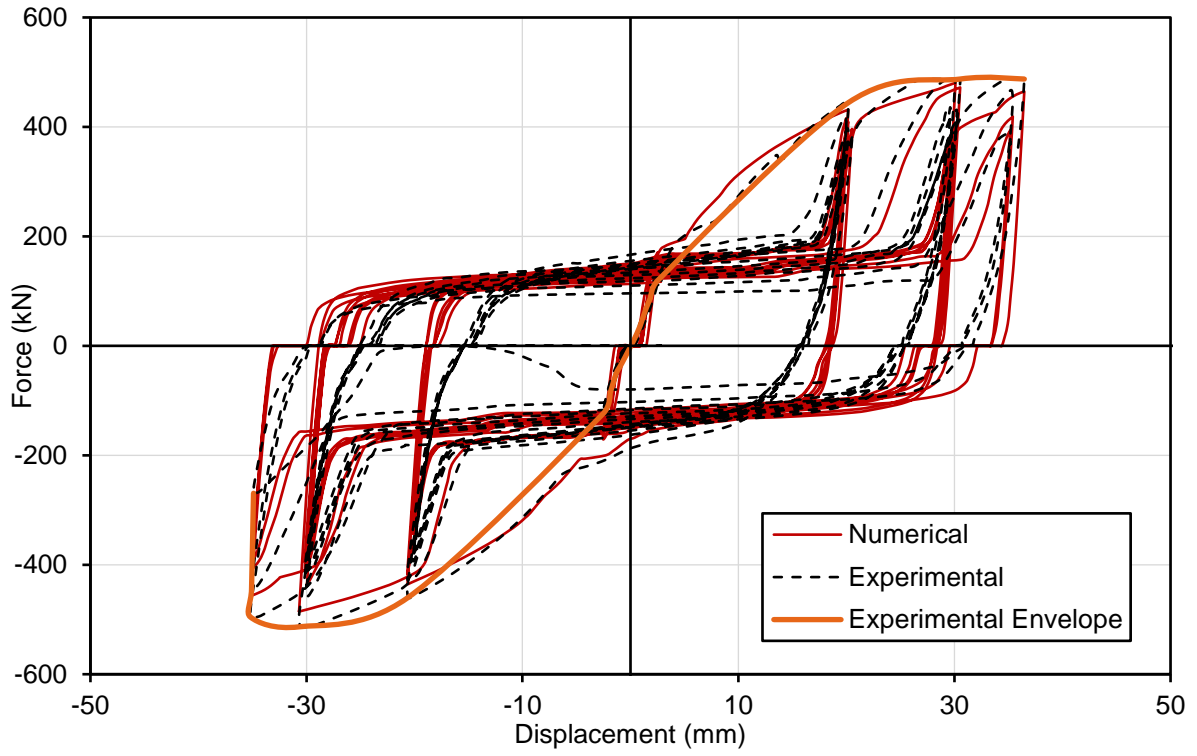


Figure B-3: Force-displacement curves comparison for test 03R.

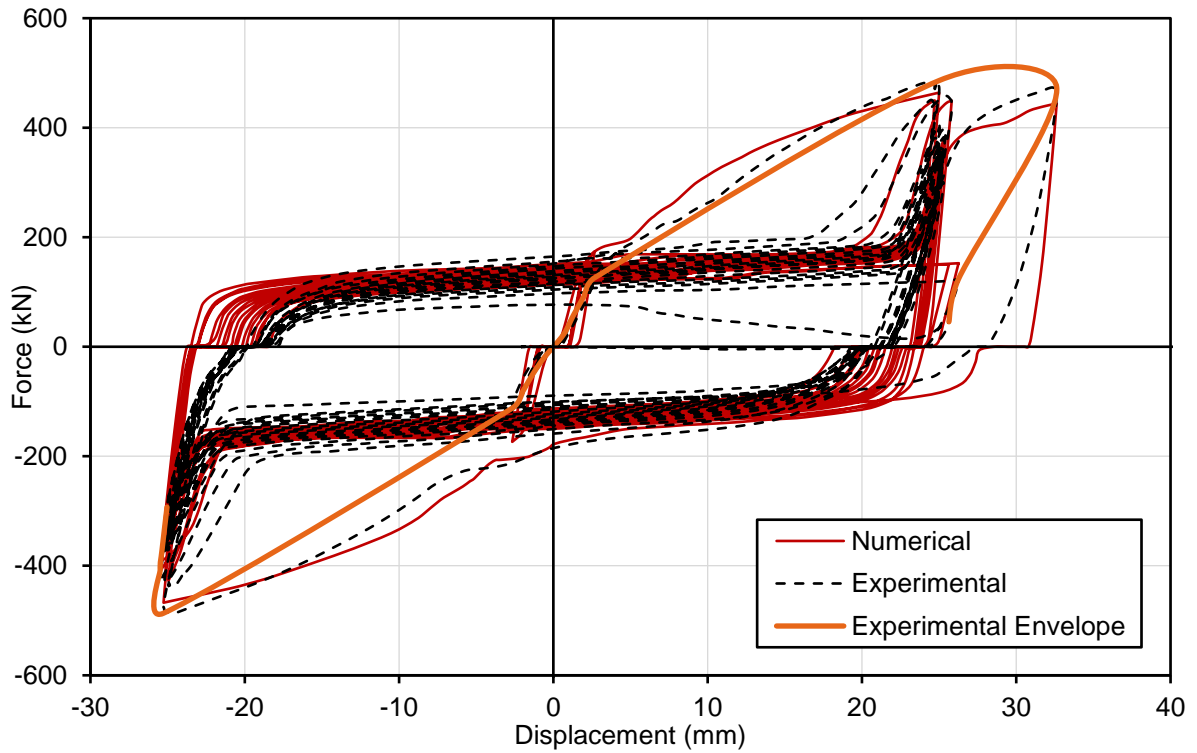


Figure B-4: Force-displacement curves comparison for test 04R.

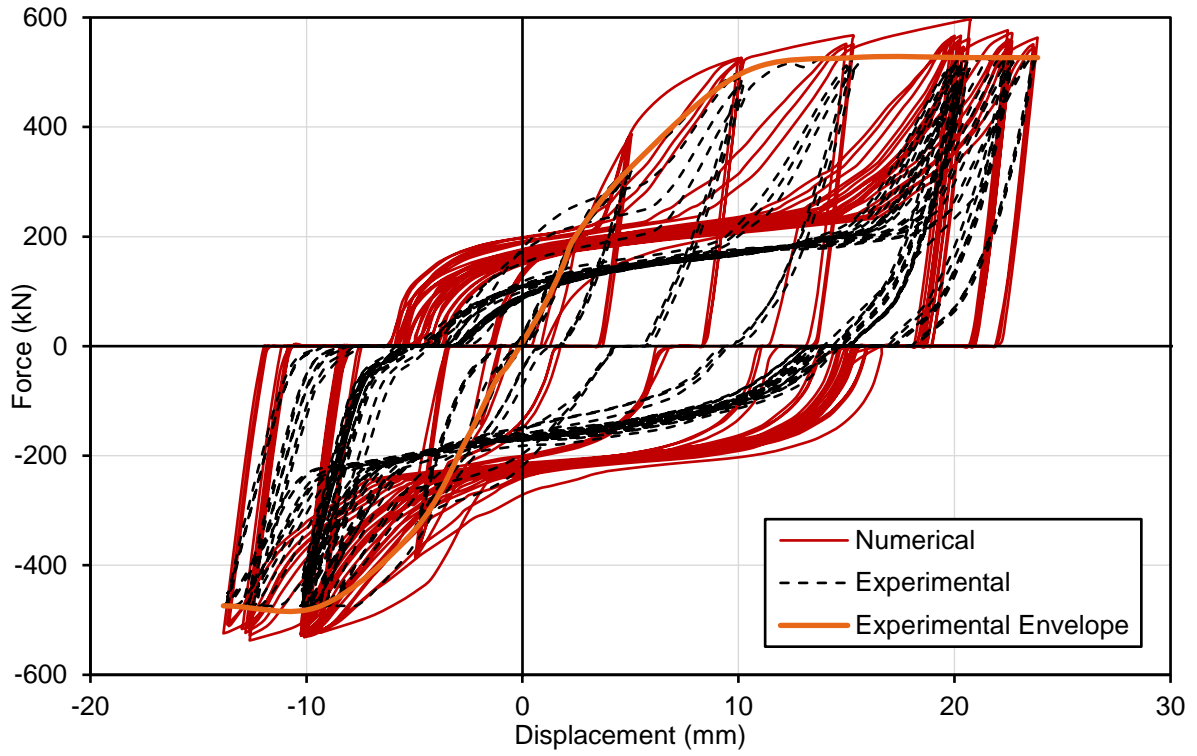


Figure B-5: Force-displacement curves comparison for test 15C.

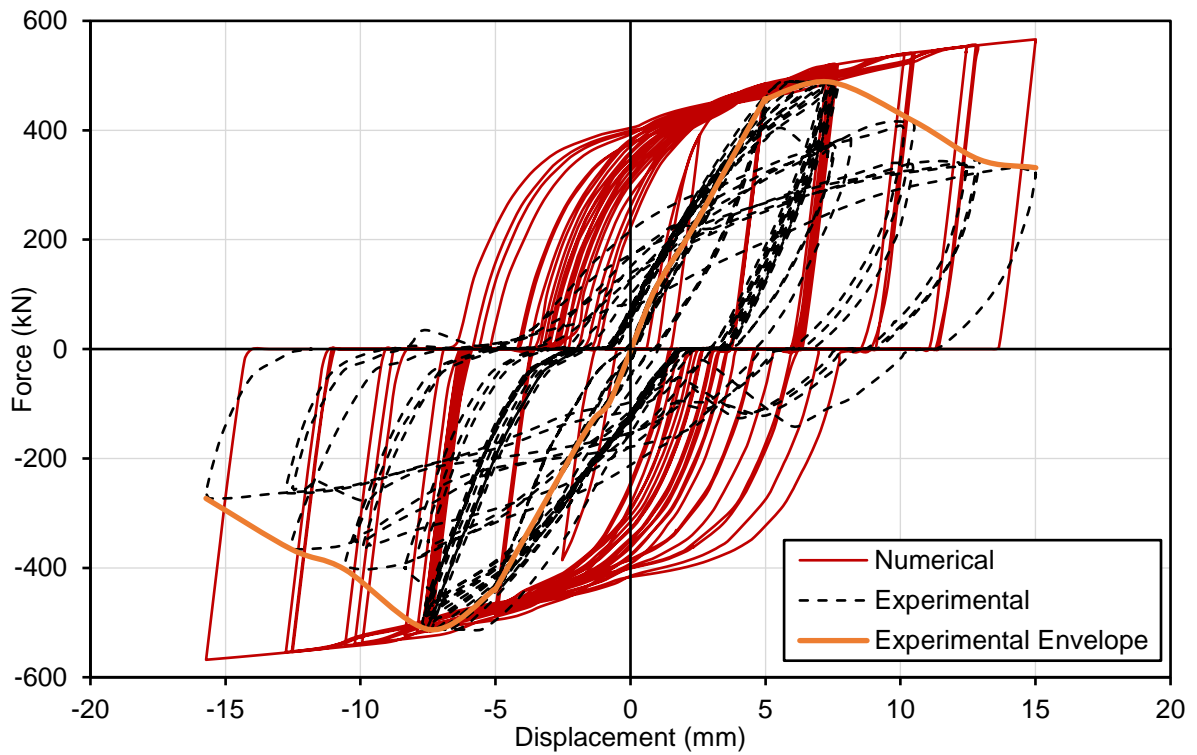


Figure B-6: Force-displacement curves comparison for test 16C.

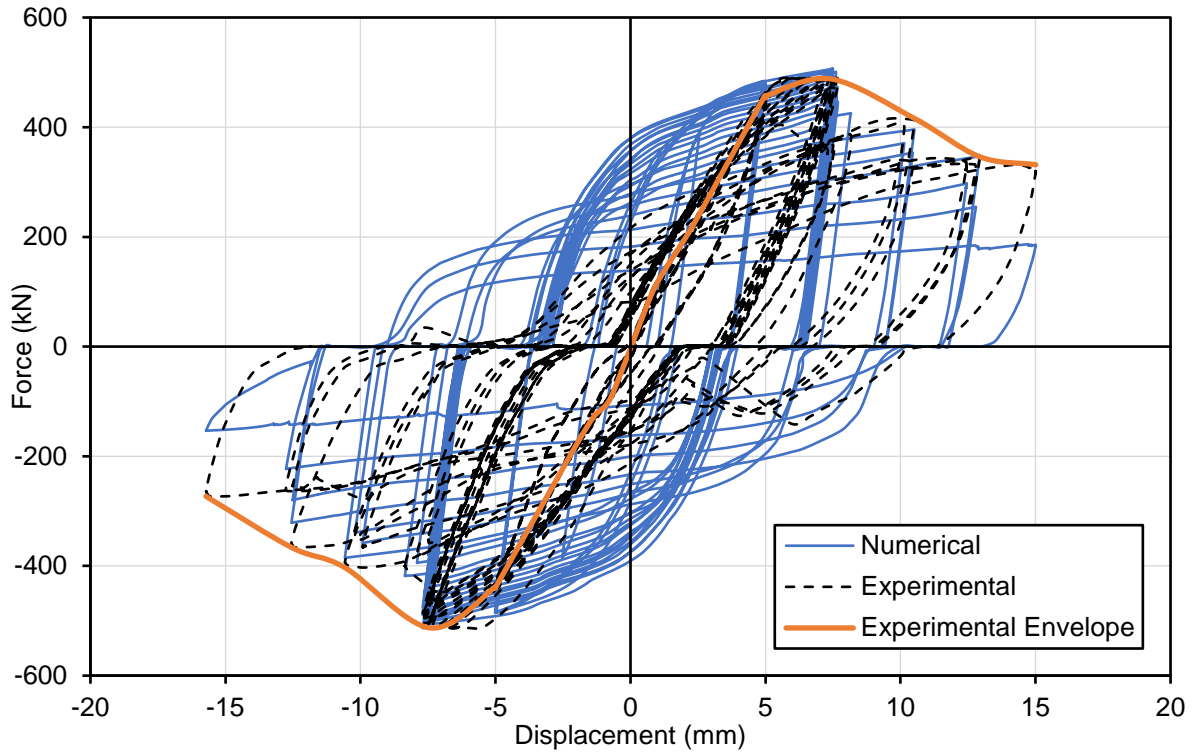


Figure B-7: Force-displacement curves comparison for test 16C with implemented damage criteria.

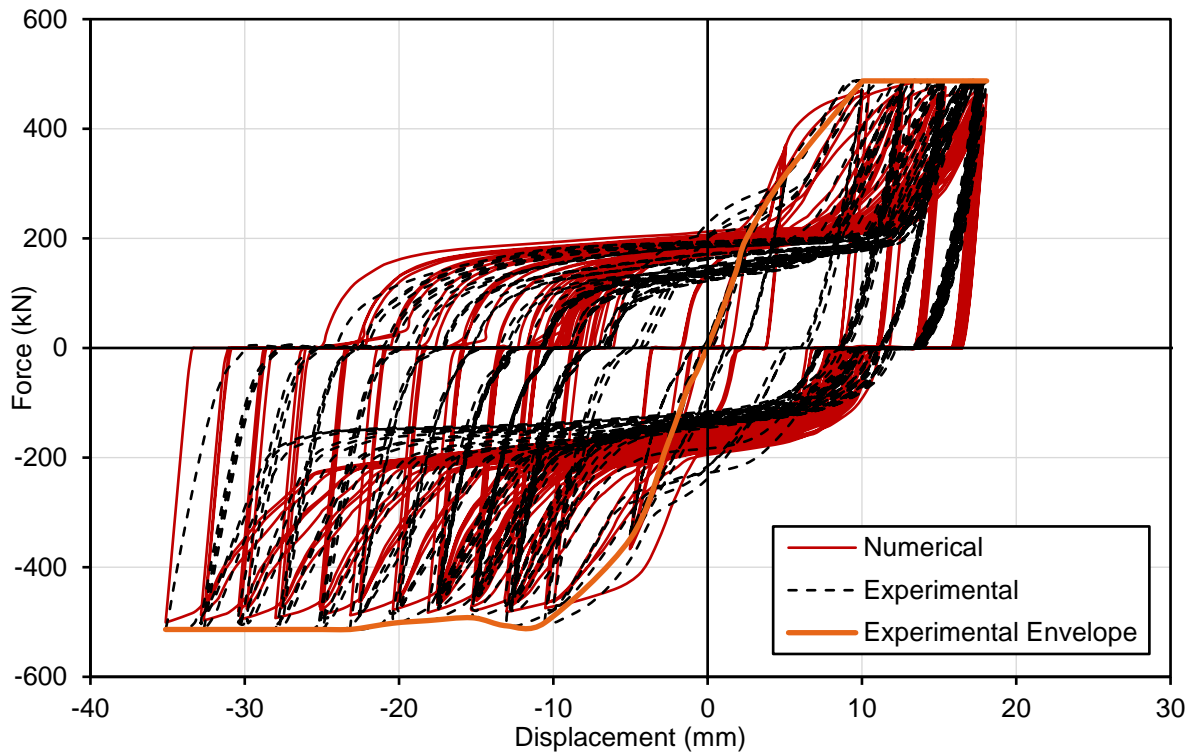


Figure B-8: Force-displacement curves comparison for test 17C.

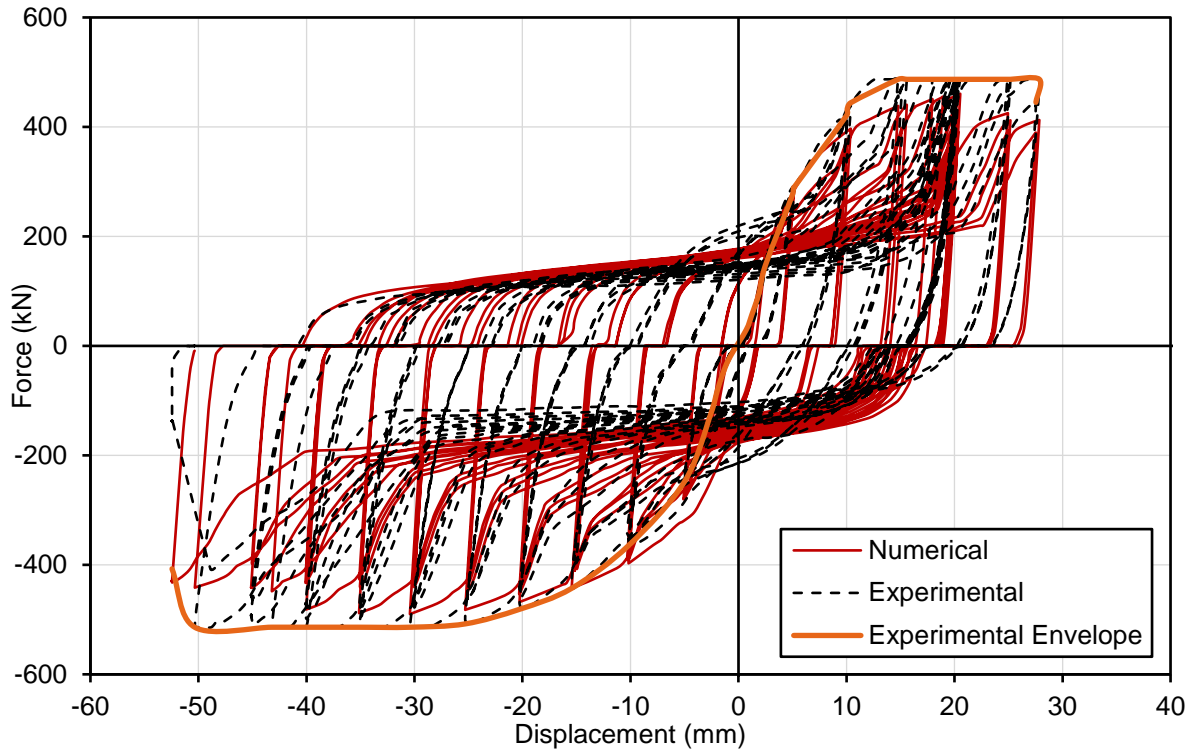


Figure B-9: Force-displacement curves comparison for test 18C.





## Annex C

Python script to extract PNG file with the force-displacement curve from symmetry model output database (.odb) file:

```
#Define the name of the plot#
import xyPlot
from time import time
a=time()
time=str(a).replace('.', '_')
xyp = session.XYPlot('XYPlot-'+time)

#Create XY DATA from ODB history output#
currentViewport = session.viewports[session.currentViewportName]
odb = currentViewport.displayedObject

def addCurve(node):
    xyNode = xyPlot.XYDataFromHistory(odb=odb,
        outputVariableName=('Reaction force: RF1 PI: Plate Top-1 Node
'+str(node)+' in NSET REACTION'),
        steps=('ECCS', ), suppressQuery=True, __linkedVpName__='Viewport: 1')
    cNode = session.Curve(xyData=xyNode)

for nodeNumber in range(36,70):
    addCurve(nodeNumber)

xy37 = xyPlot.XYDataFromHistory(odb=odb,
    outputVariableName='Spatial displacement: U1 PI: Plate Top-2 Node 10
in NSET DISPLACEMENT',
    steps=('ECCS', ), suppressQuery=True, __linkedVpName__='Viewport: 1')
c37 = session.Curve(xyData=xy37)

session.viewports['Viewport: 1'].setValues(displayedObject=xyp)

XY = [session.xyDataObjects['_temp_{}'.format(i)] for i in range(1,36)]

#Create XY Data from Operate on XYData#
xy36 = combine(-XY[-1], 0.004*sum(XY[:-1]))
tmpName = xy36.name
session.xyDataObjects.changeKey(tmpName, 'XYData-1')
xyp = session.XYPlot('XYPlot-1')
chartName = xyp.charts.keys()[0]
chart = xyp.charts[chartName]
xy1 = session.xyDataObjects['XYData-1']
c1 = session.Curve(xyData=xy1)
chart.setValues(axesToPlot=(c1, ), )
#Print PNG file of the Force-Displacement Curve#
session.viewports['Viewport: 1'].setValues(displayedObject=xyp)
session.printToFile(fileName=(os.path.basename(os.path.basename(odb.name))[:
-4]), format=PNG, canvasObjects=(
    session.viewports['Viewport: 1'], ))
```

Python script to create and run jobs from the model database file (.cae) of the tensile test with varying fracture strain, fracture energy and mesh size values.

```
#Import lines#
from abaqus import *
from abaqusConstants import *
import __main__
#Create multiple input files for varying fracture strain and fracture
energy values#
frac = [0.16, 0.18, 0.20]
ener = [200, 250, 300]
for frac_value in frac:
    for ener_value in ener:
        #Define output name#
        frac_name=str(frac_value).replace('.', '_')
        ener_name=str(ener_value)
        inp_name='FS_{}'.format(frac_name)+'FE_{}'.format(ener_name)
        data_folder = 'C:/temp/'
        file_to_open = data_folder + str(inp_name) + '.odb'
        #Define fracture strain#
        mdb.models['Model-1'].materials['Material-
1'].ductileDamageInitiation.setValues(table=((frac_value, 0.0, 0.0), ))
        #Define fracture energy#
        mdb.models['Model-1'].materials['Material-
1'].ductileDamageInitiation.damageEvolution.setValues(type=ENERGY,
table=((ener_value, ), ))
        mdb.models['Model-1'].fieldOutputRequests['F-Output-
1'].setValues(numIntervals=50)
        p = mdb.models['Model-1'].parts['Part-1']
        #Define the mesh#
        a = mdb.models['Model-1'].rootAssembly
        p.deleteMesh()
        p.seedPart(size=10.0, deviationFactor=0.1, minSizeFactor=0.1)
        p.generateMesh()
        a.regenerate()
        mdb.Job(name=inp_name, model='Model-1', description='',
type=ANALYSIS)
        #Submit the job#
        mdb.jobs[inp_name].writeInput(consistencyChecking=OFF)
        mdb.jobs[inp_name].submit(consistencyChecking=OFF)
        mdb.jobs[inp_name].waitForCompletion()
```

Python script to extract PNG file with the stress-strain curve from tensile test output database file (.odb):

```
#Define the name of the plot#
import xyPlot
from time import time
a=time()
time=str(a).replace('.', '_')
xyp = session.XYPlot('XYPlot-'+time)

#Create XY DATA from ODB history output#
currentViewport = session.viewports[session.currentViewportName]
odb = currentViewport.displayedObject

xy1 = xyPlot.XYDataFromHistory(odb=odb,
    outputVariableName='Reaction force: RF3 PI: rootAssembly Node 1 in NSET
DISPL',
    steps=('Step-1', ), suppressQuery=True, __linkedVpName__='Viewport: 1')
c1 = session.Curve(xyData=xy1)

xy2 = xyPlot.XYDataFromHistory(odb=odb, outputVariableName='Spatial
displacement: U3 PI: rootAssembly Node 1 in NSET DISPL',
    steps=('Step-1', ), suppressQuery=True, __linkedVpName__='Viewport: 1')
c2 = session.Curve(xyData=xy2)

session.viewports['Viewport: 1'].setValues(displayedObject=xyp)
xy1 = session.xyDataObjects['_temp_2']
xy2 = session.xyDataObjects['_temp_1']
xy3 = combine(-xy1, -0.001*xy2)
tmpName = xy3.name
session.xyDataObjects.changeKey(tmpName, 'XYData-1')
xyp = session.XYPlot('XYPlot-1')
chartName = xyp.charts.keys()[0]
chart = xyp.charts[chartName]
xy1 = session.xyDataObjects['XYData-1']
c1 = session.Curve(xyData=xy1)
chart.setValues(plotsToPlot=(c1, ), )

#Print PNG file of the Force-Displacement Curve#
session.viewports['Viewport: 1'].setValues(displayedObject=xyp)
session.printToFile(fileName=(os.path.basename(os.path.basename(odb.name))[:
:-4]), format=PNG, canvasObjects=(
    session.viewports['Viewport: 1'], ))
session.printToFile(fileName=(os.path.basename(odb.name))[::-4], format=PNG,
canvasObjects=(
    session.viewports['Viewport: 1'], ))
```